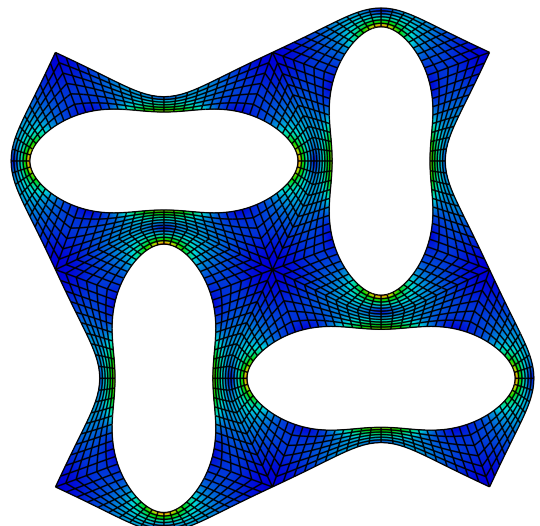
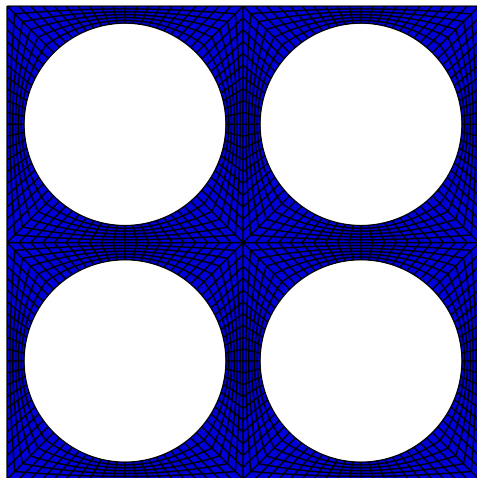




Symmetry-Breaking in Patterned Elastic Sheets



THESIS

submitted in partial fulfillment of the
requirements for the degree of

BACHELOR OF SCIENCE
in
PHYSICS AND MATHEMATICS

Author :

Casper Beentjes

Student ID :

1055275

Supervisors Physics:

Prof. dr. Martin van Hecke

Supervisor Mathematics:

Dr. Corentin Coulais

Dr. Vivi Rottschäfer

Leiden, The Netherlands, July 11, 2014

Symmetry-Breaking in Patterned Elastic Sheets

Casper Beentjes

Huygens-Kamerlingh Onnes Laboratory, Leiden University
P.O. Box 9500, 2300 RA Leiden, The Netherlands
Mathematical Institute Leiden, Leiden University
P.O. Box 9512,2300 RA Leiden,The Netherlands

July 11, 2014

Abstract

In this thesis we investigate the loading of elastic sheets, which are patterned with a square array of circular holes. An elastic buckling instability due to this loading induces a pattern transformation in the material, which breaks symmetries of the material. The pattern transformation is accompanied by a drastic change in the mechanical response, which we investigate through extensive FEM simulations, applying uni-axial as well as bi-axial loading. We find that the pre- and post-buckling response shows similarities to (thick) beam-behaviour, and therefore, we propose to model the material as single effective beams under a load. In the post-buckling phase a negative stiffness is found for certain hole sizes, which results in snap-through buckling behaviour.

Contents

1	Introduction	1
2	Role of symmetries	5
2.1	Computational domain	5
2.2	Short introduction on notation wallpaper group	7
2.3	Symmetry-breaking induced by buckling	7
2.3.1	Symmetry of undeformed geometry	7
2.3.2	Symmetry of buckled geometry	9
2.3.3	Minimal representative unit	10
3	Mechanics of (hyper)elastic materials	13
3.1	General equations	13
3.1.1	Stretch and homogeneous deformation	13
3.1.2	Displacement and strain	15
3.1.3	Forces	15
3.1.4	Newton's laws for a continuum body	16
3.2	Constitutive laws	17
3.2.1	Hookean materials (linear)	18
3.2.2	Neo-Hookean materials (non-linear)	18
3.3	Plane strain	20
4	Non-linear numerical analysis of elastic materials	23
4.1	Finite element method for elasticity problems	23
4.1.1	Weak formulation	24
4.1.2	Test-space	25
4.1.3	Search-space	29
4.1.4	Solving the non-linear FEM system	31
4.1.5	Abaqus	32
4.2	Periodic boundary conditions	32
4.3	Buckling analysis	33
4.3.1	Bifurcations and buckling	33
4.3.2	Linearised buckling analysis	36
4.3.3	Non-linear buckling analysis	38
4.4	Influence of the mesh	39
4.4.1	Mesh density	39
4.4.2	Symmetry considerations	40

5 Results	45
5.1 Force-displacement curves	45
5.2 Mapping the Holey Sheet to a beam	46
5.2.1 Theoretical predictions on non-uniform beams	47
5.3 Pre-buckling phase: small deformations	51
5.3.1 Method I: Pre-buckling stiffness	51
5.3.2 Method II: Critical Euler load	56
5.4 Post-buckling phase: large deformations	61
5.4.1 Method I: Post-buckling stiffness	62
5.4.2 Method II: Force-angle relation	66
6 Conclusion and outlook	71
6.1 Conclusion	71
6.2 Outlook	72

Introduction

A common cause of failure in structures is the buckling process. In this process, slender objects which are under a load, experience a sudden large deformation when the load slightly increases. Since large deformations can lead to a breakdown in structures such as trusses, this process can have disastrous impacts in, for example, construction frameworks. It is for this reason that in engineering much effort has been devoted to the study of buckling. A mathematical framework for buckling was already set up in the late 17th century and the 18th by bright minds such as the Bernoullis and Leonard Euler[1]. Here the focus is on describing the critical buckling conditions. The aftermath of buckling, in contrast, is not of much interest to the engineer, since structures often lose their function after failure. It is for this reason that the post-buckling behaviour has received less attention historically. However, as recent developments (see below) have shown, this post-buckling phase can actually yield some very intriguing effects when placed in a different context.

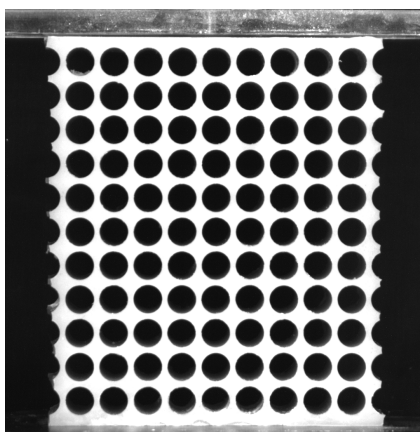
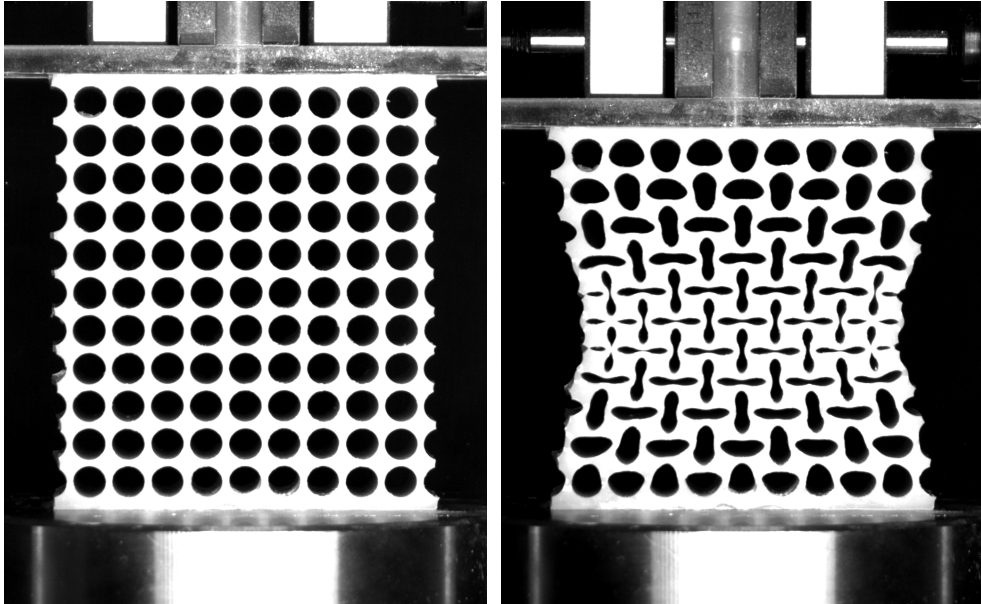


Figure 1.1: Holey Sheet: *Elastic sheet with a periodic pattern of circular holes cut out following [2]. The structure is in equilibrium without external compression. The hole size is 8.5 mm in diameter, the filament thickness 1.5 mm and the depth of the structure is 35 mm.*

In 2007 Mullin et al.[2] proposed a specific design for a so-called *meta-material*. This is a class of materials who gain their characteristic properties not from their intrinsic material properties, but from their specifically designed (microscopic) structures. Mullin et al. took an elastomeric sheet and constructed a specific architecture, consisting of a regular pattern of circular holes, as depicted in figure 1.1. Their meta-material is often dubbed, with a sense of humour, the "*Holey Sheet*". Its specific periodic structure results in interesting mechanical effects when the material

is loaded, such as negative stiffness and a negative Poisson's ratio, which will be explained soon hereafter.

In [2] and other follow-up articles [3, 4], several peculiar properties of the Holey Sheet were discovered. It was observed that under compression a pattern transformation arises at a certain critical point, see the difference between figure 1.2a and 1.2b. This critical point precisely coincides with the point where the filaments in between the circular holes start to buckle. Since the Holey Sheet is made of elastic material, the deformations are reversible, which is not only advantageous for experiments but also for possible applications. The observed pattern transformation alone is an interesting phenomena to observe, but a more striking property can be observed as well.



(a) I: The applied compression is smaller than the critical displacement and only small deformations are present. *(b) II: The applied compression is larger than the critical displacement and the Holey Sheet has buckled, resulting in large displacements.*

Figure 1.2: Photos taken during compression of the Holey Sheet in figure 1.1 in an Instron machine.

When normal materials get compressed along an axis, the material will expand in the two transversal directions. This effect is known as the Poisson effect, named after Siméon Poisson. A measure can be constructed for this effect, known as the Poisson's ratio ν . When we define the strain ε of a material as the relative elongation (positive or negative) of the material, then the Poisson's ratio ν is given by:

$$\nu = -\frac{\varepsilon_{\text{transversal}}}{\varepsilon_{\text{axial}}}. \quad (1.1)$$

From this definition one can see that for normal materials ν will be a positive number. However, for the Holey Sheet we observe something counter-intuitive, see figure 1.2b. When we compress in the vertical direction, the structure shrinks in the horizontal direction as well, resulting in a negative Poisson's ratio. Materials with this non-standard behaviour upon compression are known as auxetic materials and are only known to exist in man-made form since 1987[5]. Although multiple articles have been published related to this meta-material, the precise underlying mechanisms explaining its behaviour are still unknown.

When the force needed to compress the Holey Sheet is plotted against the compression, typical non-linear behaviour can be observed, see figure 1.3. A linear regime seems to describe the behaviour up to the critical point. After this linear part, a peak can be observed. This observation is quite surprising as the buckling predictions by Euler don't have such a peak. It is this distinct and non-linear feature of the Holey Sheet that we try to understand in this thesis. An interesting question one could ask is whether the nature of this peak can be tuned, for example by setting different control parameters in the design of the Holey Sheet. In this way a *programmable meta-material* could be constructed, with a specifically designed geometry to ensure the desired response.

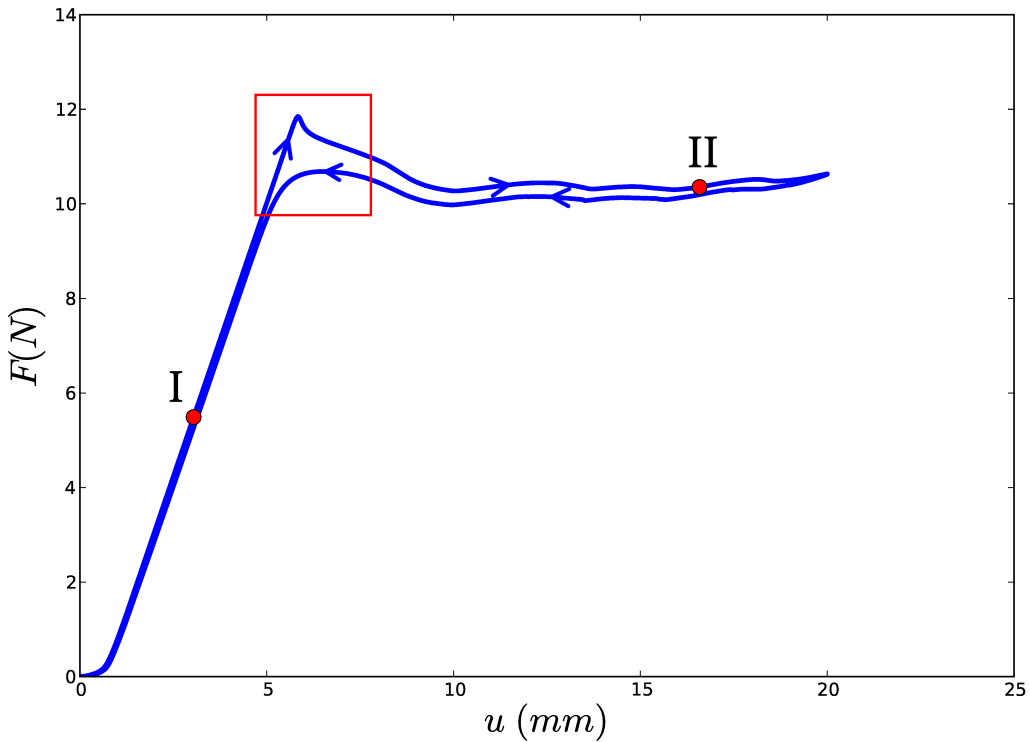


Figure 1.3: Plot of the experimentally observed force F versus the displacement, or compression, u , as measured for the Holey Sheet depicted in figure 1.2. The red dots correspond to the pictures in 1.2; I to 1.2a and II to 1.2b. A clear peak and non-linear behaviour in the $F - u$ curve can be seen in the red box.

The two different curves originate from the fact that the experiment compresses the sample and then returns progressively to the original uncompressed state. The return is observed to be slightly different from the compression.

The design parameters for the Holey Sheet are basically restricted to the amount of holes and the size of the holes. For reasons to be shown shortly hereafter, the effect of the hole-size was of primary interest in this thesis and therefore the specific design parameter was chosen to be the radius of the holes, or equivalently the thickness t of the filaments separating the holes. In order to study the tunability of the response one would then like to perform a parameter study to see whether, and if so how, the response of the Holey Sheet changes under variation of t . Since the process of creating the Holey Sheets is rather involved, it would be very time-consuming to explore the parameter space of t in this way. Therefore we take a different angle for this thesis, we

simulate the Holey Sheet using numerical methods. The numerical exploration of the problem is complementary to the experimental work being a much more flexible approach concerning the exploration of the parameter space. It is also complementary in the sense that it provides us with a way of performing experiments which might help us to understand the Holey Sheet, but which are hard to perform in the laboratory. For instance, a uniform compression at all the sides of a sheet, known as a bi-axial compression test, is rather difficult to attain in experiments. However, it can be easily implemented in numerics. This bi-axial test is not just a pathological example, it can in fact be useful when studying the influence of symmetries on the system as it is one of the few mechanical tests which invoke buckling in the Holey Sheet (see chapter 2).

This thesis will start with a short treatise on the symmetries of the Holey Sheet, which obviously play a major role in the peculiar behaviour it displays. This is followed by a concise and necessary introduction into the field of continuum mechanics. Using this formulation of mechanics the equations governing the elastic behaviour of the Holey Sheet can be derived. In chapter 4 we introduce the numerical method of finite elements (FEM), which will be applied to study the Holey Sheet. Due to the non-linearity of this problem, the study of the response under a load is a challenging numerical problem and the methods to deal with this non-linearity are presented in chapter 4 as well. At last, chapter 5 will be devoted to the actual results from the numerical simulations and the interpretation of the data.

Chapter 2

Role of symmetries

The Holey Sheet has a lot of internal symmetries, for instance a translation symmetry due to the periodic lattice structure. Another symmetry that is present is a rotational symmetry because of the circular pattern placed in a square array.

One way of classifying symmetries in periodic two-dimensional objects is by making use of the wallpaper group[6]. This group consists of all the 17 possible two-dimensional periodic structures which have some rotational or reflection symmetry in addition to a translational symmetry due to its periodicity. As we will see in the chapter 4, the symmetry can have a huge influence on the numerical simulations, by either preventing or stimulating collapse due to buckling. This is closely related to the fact that the symmetries play a major role in the bifurcation of these symmetric objects. Bifurcations, and pitchfork bifurcations in particular, often involve symmetry breaking. This chapter will explore the symmetries of both the undeformed and the deformed Holey Sheet as well as the additional role of the external forcing. To begin with, we will discuss the computational domain chosen for the numerical study of the Holey Sheet.

2.1 Computational domain

Upon glancing at the experimental force-displacement curve 1.3, one might see that the behaviour after buckling seems quite irregular and there might therefore be multiple processes simultaneously responsible for the precise response. It is for this reason that we decided to zoom in on the problem. The decision that we made in this project is to neglect all large length scale deformations and inhomogeneities. An example of this can be observed in 1.2b, where we can see that at the edge of the Holey Sheet a curvature is present, which is not seen in the rest of the material. Typical large length scale inhomogeneities can be found at the edges of the Holey Sheet and these are sometimes referred to as edge effects. The question is whether we can still explain the phenomena observed in the experiments when we neglect these features, as it might be a combined effect.

How does one accomplish such a study which only concentrates on the small length scales? The answer to this problem might seem strange, but we focus on infinite sized Holey Sheets. This is done by considering an infinitely periodically tiled sheet. In order to do so, one must choose a building block to tile the space with. The building block then needs to be given periodic boundary conditions in order to completely fill the space. There are many ways in which we can choose this fundamental tiling-element, but since we want to neglect large scale effects it seems logical to choose the smallest element possible, just one circular hole, also called the primitive cell. The periodic boundary conditions then make sure that only small length scale

effects are taken into consideration. However, as we can see in figure 2.1, there is more than initially meets the eye. In the buckled state the original symmetry has been broken and therefore the primitive cell does not simply tile the space any more. The pattern transformation thus demands that a larger building block is considered, which we call the (computational) unit cell, see figure 2.1. Now the whole two-dimensional space can be tiled by the unit cell with periodic boundary conditions, both in the pre-buckling phase as in the post-buckling phase. As an additional advantage of the unit cell for this thesis we can remark that it is computationally much more efficient to use the unit cell than large Holey Sheets, since computational time heavily depends on the problem size. For three dimensional problems it often scales at least cubically with the problem size, and for two dimensional problems mostly at least quadratically. It is also possible to carry out simulations which involve large wavelength deformations later on, based on the initial simulations on the unit cell with little adaption of the procedures. This, however, was not part of this particular thesis.

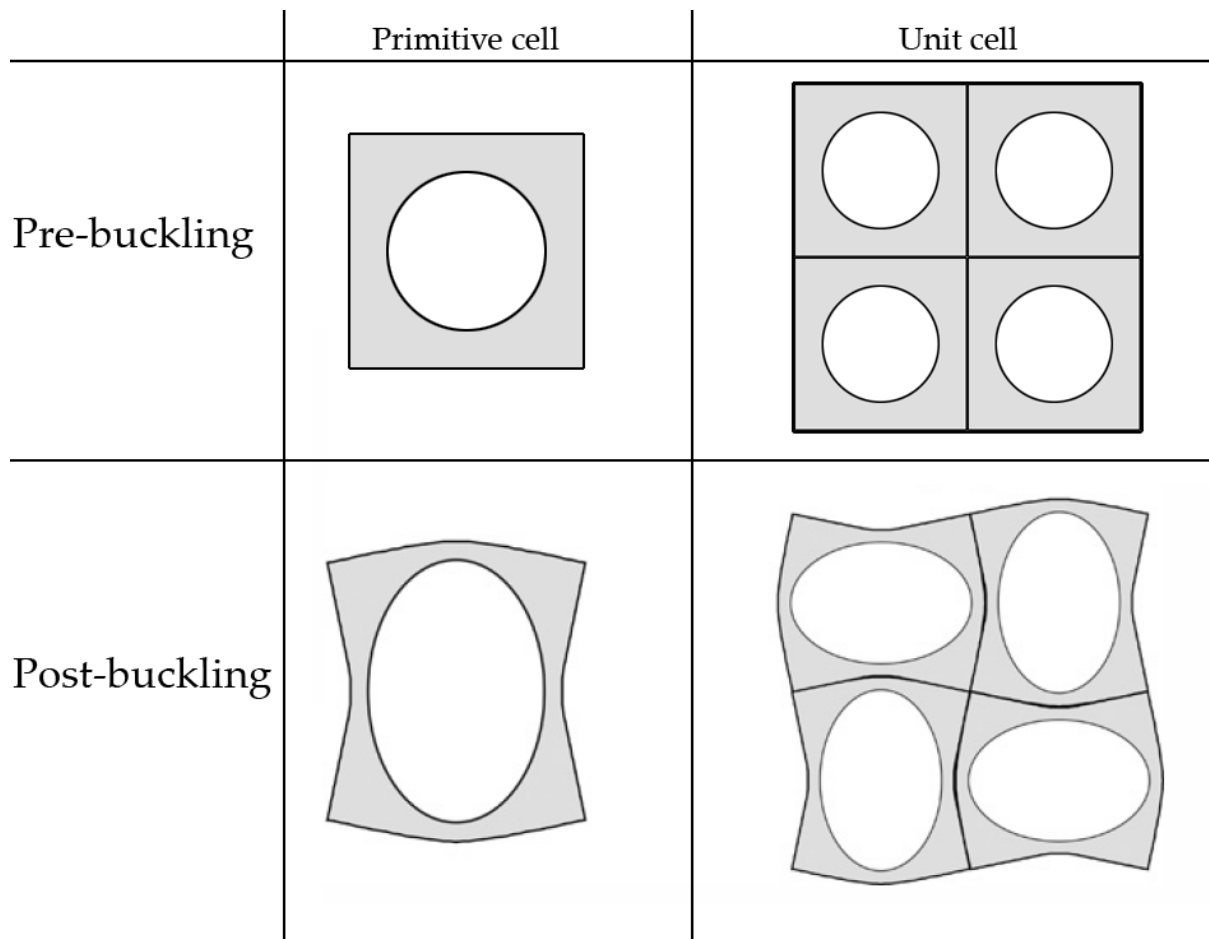


Figure 2.1: Sketch of the difference between the primitive cell and the unit cell for the Holey Sheet. After the buckling the primitive cell is not the building block of the periodic (translational) pattern any more and therefore a larger cell, the unit cell, needs to be studied. Figures adapted from [3].

2.2 Short introduction on notation wallpaper group

Before we can proceed to the discussion of the symmetries of the Holey Sheet some small remarks on the wallpaper group and its notation need to be made. First of all, the different kind of mappings representing symmetries are, to be precise, called isometries. There are three different kinds of these isometries present in the wallpaper group, namely rotations, reflections and glide reflections. The first two are well-known and we will not introduce them. The glide reflections may be less known and therefore we quickly discuss them here. Gilde reflections are a combination of a reflection in a certain line, together with a translation. This translation will always be over one half of a vector in the translation group of the object, such that it again matches the original domain.

In the sketches in this chapter the reflections will be denoted by a solid blue line, depicting the mirror line of the reflection. The glide reflections will be denoted by a dashed magenta line, which is equal to the reflection axis. The translational part of the glide reflection is not sketched. The rotations will be denoted by either a diamond for rotations over π , or a square for rotations over $\frac{\pi}{2}$. Rotations over other angles are not isometries of the Holey Sheet in any configuration and are therefore not discussed.

- - - - - Glide reflection axis.
- Reflection axis.
- ◆ Center of rotation over π .
- Center of otation over $\frac{\pi}{2}$.

Figure 2.2: Notation of the different isometries of the wallpaper group which are encountered in the Holey Sheet.

The notation for the different groups of the wallpaper group in the following sections will follow that of crystallography. This means that a code of 4 digits or letters is given to each group to summarize its isometries. The code starts with a p or a c. The p stands for a primitive cell and the c for a face-centered cell, of which the difference is not of much importance for this thesis. This letter is followed by an integer depicting the highest order of rotation, where 1 stands for no rotation. The last two symbols can be m, g or 1. The third symbol is reserved for an isometry normal to the left edge of the chosen cell, and the fourth one for an isometry axis which makes a predefined angle to the left edge[6]. The m stands for mirror, or an reflection axis and the g for a glide reflection axis. The 1 indicates that there is no isometry axis. Some of the symmetries can actually be deduced from a 3-digit instead of a 4-digit code and therefore these are often found in abbreviated form. The examples which are encountered when studying the Holey Sheet are p4mm (p4m), p4gm (p4g), p2mm (pmm) and c2mm (cmm).

2.3 Symmetry-breaking induced by buckling

2.3.1 Symmetry of undeformed geometry

In the undeformed state the Holey Sheet's repetitive unit of the periodic pattern is not the actual unit cell as mentioned in the introduction. It is actually a quarter of this unit cell, consisting only

of square with a hole. However, if we look at the Holey Sheet after it has buckled, we see that we need a larger repetitive unit to tile our space with to retrieve our object. This transition is due to a broken symmetry as a result of the buckling. Before the buckling the unit cell could be reflected in one of its diagonals or bimedians without changing the geometry. After buckling, this reflection symmetry is not present anymore and a larger repetitive cell consisting of four holes is needed to tile the sheet completely.

The symmetries of this object are determined by the symmetries of a square since the circular hole has even more symmetries. In terms of the wallpaper group the undeformed geometry has therefore symmetry group p4m, see figure 2.3.

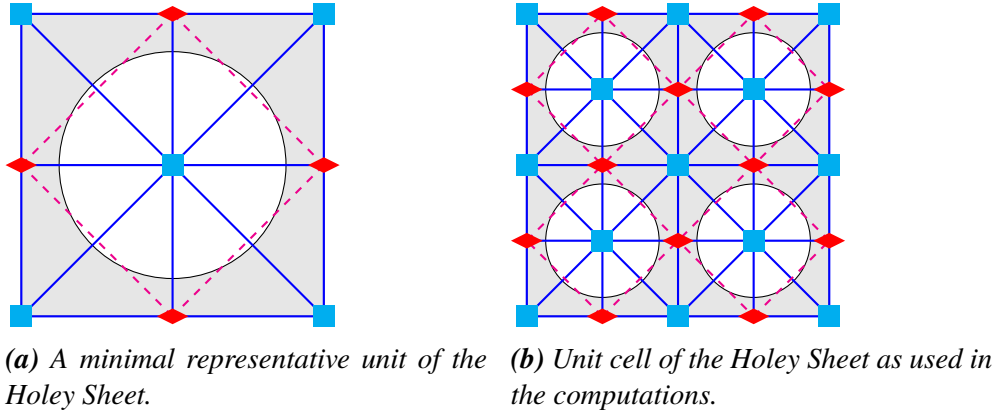
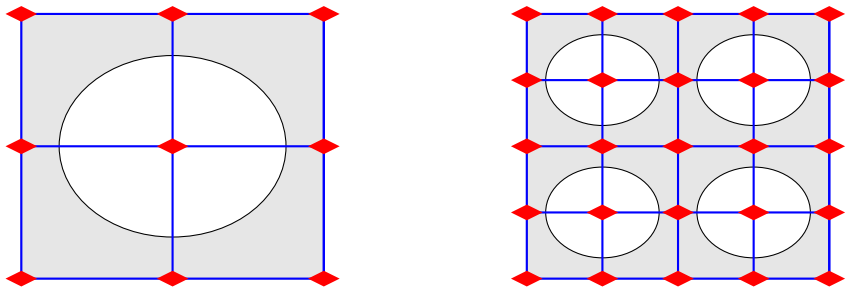


Figure 2.3: Symmetries of the undeformed geometry of the Holey Sheet, p4m. The symmetries of the Holey Sheet under bi-axial compression in the pre-buckling phase are equal to that of the undeformed geometry and are therefore represented by the above sketch as well.

Influence external forcing

The preceding discussion is only valid in the case of an equilibrium without any compression due to an external force. By imposing boundary conditions through forces on the boundary we influence the symmetries in the system. Of special interest for this thesis are two types of external forcing. The first type of forcing is applying a force on a single axis orthogonal to the original surfaces, therefore called uni-axial forcing. The equivalent situation in which we impose a displacement constraint on two opposing surfaces only, for which a uni-axial forcing is needed, is therefore called uni-axial compression. By imposing uni-axial compression we immediately break some of the symmetries of the system, for example the $\frac{\pi}{2}$ rotation around the center of the unit cell. This is due to the fact that the Poisson effect causes the Holey Sheet to expand in the horizontal direction.

Although it seems that this breaking of the symmetry has no influence on the buckling on first glance, because the symmetry which is broken by the bifurcation is a different one, it will turn out that significant differences can be observed if this symmetry is in fact preserved. The way this is done, is of course by imposing uniform forcing on the unit cell and thus applying an equal orthogonal force on every surface of the cell. This type of forcing is then called bi-axial forcing and has of course an equivalent bi-axial compression. In qualifying the symmetry groups of the Holey Sheet under external forcing we see that the bi-axial compression before the buckling point doesn't change the symmetries of the system and therefore the symmetry group is still p4m. In the case of the uni-axial compression we find a pmm symmetry, which thus lacks some rotational symmetry compared to p4m, see figure 2.4.



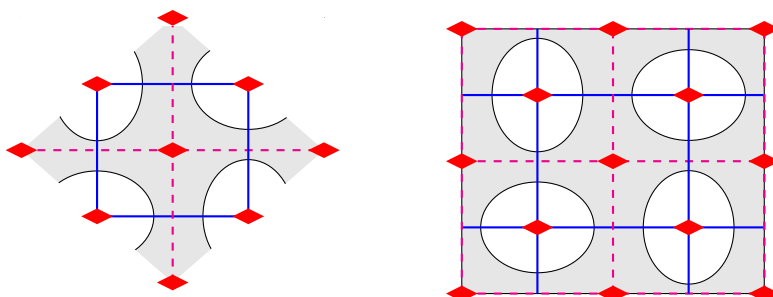
(a) A minimal representative unit of the Holey Sheet.
(b) Unit cell of the Holey Sheet as used in the computations.

Figure 2.4: Isometries of the Holey Sheet under uni-axial compression in the pre-buckling phase, pmm. The difference with 2.3 is due to the fact that the geometry now is not a perfect square any more due to the Poisson effect, which makes the Holey Sheet expand in the horizontal direction.

2.3.2 Symmetry of buckled geometry

Uni-axial compression

What is of course more interesting is the change of symmetry that is created by the buckling of the Holey Sheet. In the case of the uni-axial compression we first note that in the direction orthogonal to the forcing there is an expansion and the square unit cell has thus changed to a rectangular unit cell. This was already the case before the buckling took place and incorporated in the pmm group. However, after the buckling we loose the aforementioned reflection symmetry in the bimedian aligned with the external forcing and orthogonal to the forcing. They both change in glide reflections, just as the reflection axis on the sides of the computational unit cell. First the circles transform into aligned ellipses with their primary axis orthogonal to the external forcing. At the buckling point then we observe an abrupt pattern transformation, from aligned ellipses to orthogonal aligned ellipses. Therefore only a few of the original symmetries remain in the buckled state. Due to the change of reflections to glide reflections some rotations are lost as well, since they lie only at the intersection of two reflection axes or two glide reflection axes. The symmetry group of the buckled geometry is classified as the cmm group and the minimal representative unit cell now has the form of a rhombus, see figure 2.5.

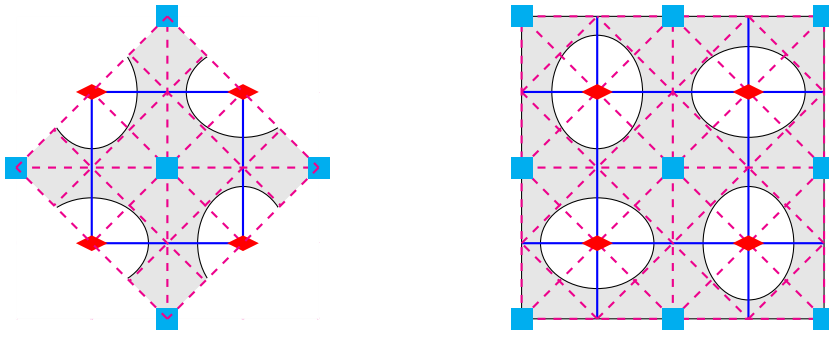


(a) A minimal representative unit of the Holey Sheet.
(b) Unit cell of the Holey Sheet as used in the computations.

Figure 2.5: Isometries of the Holey Sheet after the buckling has occurred under uni-axial compression, cmm. A minimal representative unit now is clearly distinct from the undeformed minimal representative units.

Bi-axial compression

As mentioned before the bi-axial compression starts with a p4m symmetry which remains intact until the buckling point is reached. After the buckling we observe a similar pattern transformation from circles to orthogonal aligned ellipses. Before the buckling point the circles of the unit cell shrink, but do not transform into ellipses. In this case a few more isometries are present, since we can still rotate over $\frac{\pi}{2}$ around the center and the four vertices and intersections of the bimedians. We see that in comparison with the pre-buckling isometries, a lot of the original reflections have transformed into glide reflections. Only the reflections along the ellipse-axes remain intact. This is accompanied by a loss of a number of rotation centers, namely all the original rotations over π . The rotation centers who were on the diagonal reflection axis change from rotations over $\frac{\pi}{2}$ to rotations over π . If we compare to the uni-axial compression, we see that the rotation centers are equally distributed, only the order of the rotations in the bi-axial case differs, because there is no shearing of the unit cell. Furthermore the reflection axes in the buckled case are equal as well, together with the horizontal and vertical glide reflections. The only big difference is the number of diagonally oriented glide reflections for the bi-axial compression case.

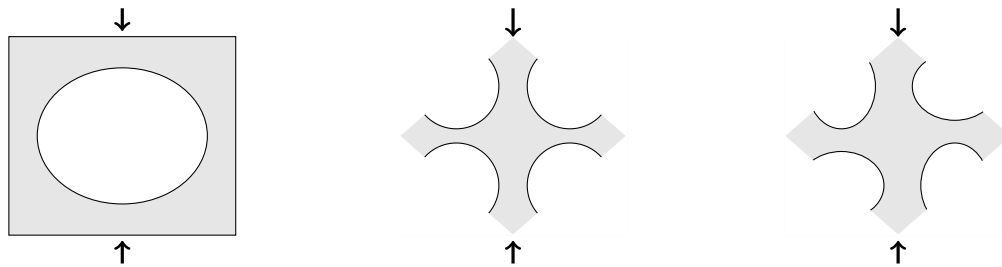


(a) A minimal representative unit of the Holey Sheet.
(b) Unit cell of the Holey Sheet as used in the computations.

Figure 2.6: Isometries of the Holey Sheet after the buckling has occurred under bi-axial compression, p4g. A minimal representative unit now is clearly distinct from the undeformed minimal representative units.

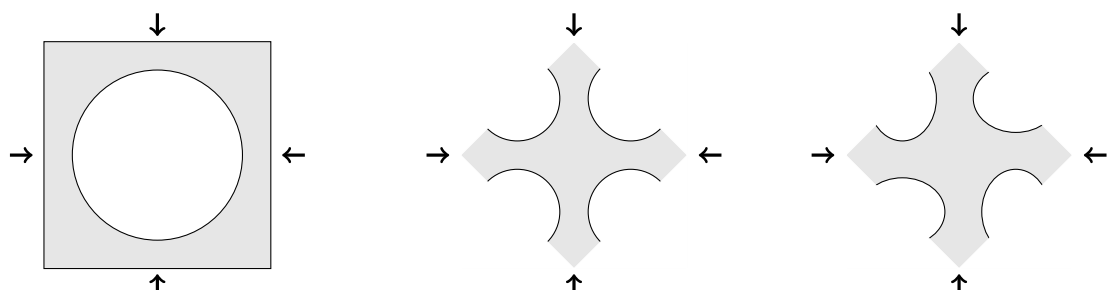
2.3.3 Minimal representative unit

To recap the results from the previous sections, we sketch for each phase a minimal representative unit. We see that there is in fact little difference between the uni-axial and the bi-axial case regarding the representative unit. The uni-axial ones are merely sheared, they have been elongated in the horizontal direction and compressed in the vertical direction. We also see that the minimal representative units, as sketched in figure 2.7 and 2.8, are smaller than the computational domain used in this thesis. These suggested representative units might help to make an even more efficient numerical scheme, as they suggest that a smaller unit cell could be chosen such that the whole space can be tiled. A smaller size cell means less computation time. Although the minimal representative units have not been used, they do single out the smallest building block of the Holey Sheet. It is an interesting question to see whether it is possible to check if the behaviour of this building block coincides with that of a Holey Sheet.



(a) A minimal representative unit of the pre-buckling Holey Sheet. (b) Unit cell of the pre-buckling Holey Sheet corresponding to the minimal representative unit cell of the buckled geometry on the right. (c) A minimal representative unit of the buckled Holey Sheet.

Figure 2.7: Representative units for the uni-axial compression of the Holey Sheet.



(a) A minimal representative unit of the pre-buckling Holey Sheet. (b) Unit cell of the pre-buckling Holey Sheet corresponding to the minimal representative unit cell of the buckled geometry on the right. (c) A minimal representative unit of the buckled Holey Sheet.

Figure 2.8: Representative units for the bi-axial compression of the Holey Sheet.

This page would be intentionally left blank if we would not wish to inform about that.

Mechanics of (hyper)elastic materials

In this first chapter the basic equations needed to describe an elastic material under deformations are derived and notation is introduced. Only a small part of a very large field known as continuum mechanics is covered here. Continuum mechanics is a branch of mathematical physics which tries to describe the mechanics of material bodies or systems, fluids and gasses. In this thesis we are mainly interested in the equilibrium configurations of materials and therefore in static situations. As a result, (almost) no time dependency will be covered here.

Firstly, a general description of material deformation in \mathbf{R}^3 will be given. Thereafter the specific structure of the Holey Sheet will allow us to restrict our three dimensional framework to two dimensions. This will turn out to be very helpful in our numerical simulations as it saves computation time. The main ingredients in the derivation of the basic equations are just the laws of Newton and certain conservation laws, such as conservation of linear momentum. After the framework of continuum mechanics has been set up properly the governing equations follow naturally.

3.1 General equations

3.1.1 Stretch and homogeneous deformation

To introduce the concept of stretch we start with a one dimensional line of length L , see figure 3.1. Then we stretch this line to a new configuration in which it has length l . The stretch λ is then defined to be the ratio of these lengths:

$$\lambda = \frac{l}{L}. \quad (3.1)$$

Now pick one reference point \tilde{x} on the line and another point x on the line as well. Their difference ‘vector’ will then be denoted by $y = x - \tilde{x}$. Note that the absolute value of this difference vector is the distance between the points. By stretching the line we change the coordinates of the points. This is mathematically described by a mapping Φ of the original configuration onto the deformed configuration. After the deformation the points will have new coordinates, say $\tilde{x}' = \Phi(\tilde{x})$ and $x' = \Phi(x)$. This allows us to write down their difference vector $y' = x' - \tilde{x}'$ just as we did before. The deformation of the line is said to be homogeneous if we have the following relation between y and y'

$$y' = \lambda y, \quad (3.2)$$

holding for arbitrary points on the line. This concept of stretch can easily be generalized to

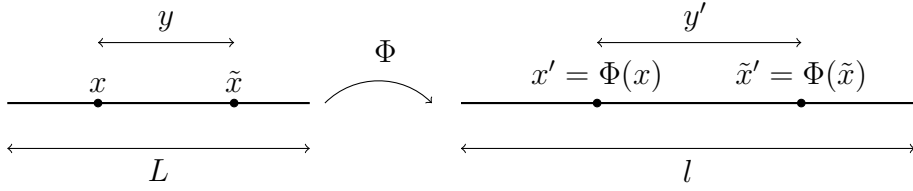


Figure 3.1: Sketch of stretch of a one-dimensional line deformed by Φ .

describe general deformations in \mathbf{R}^3 . We start with a material system $\Omega_0 \subset \mathbf{R}^3$ which deforms via the mapping Φ to the new system Ω' which thus is equal to $\Phi(\Omega_0)$. Ω_0 is often called the reference state whereas Ω' is called the current state. Take again a reference point $\tilde{\mathbf{x}} \in \Omega_0$ and an arbitrary point $\mathbf{x} \in \Omega_0$. Just as we saw in the one dimensional case, a difference vector $\mathbf{y} = \mathbf{x} - \tilde{\mathbf{x}}$ can be defined which will be mapped to a new vector $\mathbf{y}' \in \Omega'$. In general this can be expressed by using an operator $\bar{\mathbf{F}}$ which is called the deformation gradient;

$$\mathbf{y}' = \bar{\mathbf{F}}(\mathbf{y}). \quad (3.3)$$

To see why this is called the deformation gradient, we will write the difference vector \mathbf{y}' in terms of the deformation mapping Φ ,

$$\mathbf{y}' = \Phi(\mathbf{x}) - \Phi(\tilde{\mathbf{x}}). \quad (3.4)$$

Now the general multi-variable version of Taylor's Theorem [7] can be applied, which yields

$$\Phi(\mathbf{x}) = \Phi(\tilde{\mathbf{x}}) + \nabla\Phi(\tilde{\mathbf{x}}) \cdot (\mathbf{x} - \tilde{\mathbf{x}}) + o(||\mathbf{x} - \tilde{\mathbf{x}}||). \quad (3.5)$$

Due to this identity we can write

$$\mathbf{y}' = \nabla\Phi(\tilde{\mathbf{x}}) \cdot (\mathbf{x} - \tilde{\mathbf{x}}) + o(||\mathbf{x} - \tilde{\mathbf{x}}||) = \nabla\Phi(\tilde{\mathbf{x}}) \cdot \mathbf{y} + o(||\mathbf{x} - \tilde{\mathbf{x}}||). \quad (3.6)$$

Thus, neglecting $o(||\mathbf{x} - \tilde{\mathbf{x}}||)$, we see that by comparing (3.3) and (3.6) we find that $\bar{\mathbf{F}} = \nabla\Phi(\tilde{\mathbf{x}})$ and thus the operator $\bar{\mathbf{F}}$ equals the Jacobian of the deformation map Φ . This explains the name deformation gradient. The deformation is furthermore called homogeneous if the deformation gradient is independent of the position $\tilde{\mathbf{x}} \in \Omega_0$. Therefore, a homogeneous deformation has a deformation gradient which can be represented by a 3×3 matrix $\bar{\mathbf{F}}$ with constant entries. This immediately implies that the deformation gradient is a linear operator for homogeneous deformations. The restriction of homogeneous deformations is rather strict in the sense that only a limited number of different transformations are allowed. To be more specific, only the affine transformations are homogeneous transformations. This can be seen if we plug the deformation gradient back into the Taylor expansion (3.6) and neglect the rest term to get

$$\Phi(\mathbf{x}) = \Phi(\tilde{\mathbf{x}}) + \bar{\mathbf{F}} \cdot (\mathbf{x} - \tilde{\mathbf{x}}) = \bar{\mathbf{F}} \cdot \mathbf{x} + \mathbf{c}, \quad (3.7)$$

for some constant vector \mathbf{c} . Examples of affine transformations are translation, rotation, stretch, compression, and shear transformations.

However, general transformations don't need to be homogeneous. It is possible to have a deformation gradient field which isn't uniform over Ω_0 . As a result, straight lines don't need to get mapped to straight lines by Φ . Although not true on a global scale, if we look at a small local scale then every transformation will be a homogeneous transformation, because $\bar{\mathbf{F}}$ will not vary much over a short distance. Therefore we can look at the action of an inhomogeneous

deformation as being composed of many homogeneous transformations patched together. Having introduced the deformation gradient $\bar{\mathbf{F}}$ one can also wonder how distances between points change under Φ . Using the deformation gradient one finds that $\Phi(\mathbf{x}) - \Phi(\tilde{\mathbf{x}}) \simeq \bar{\mathbf{F}} \cdot (\mathbf{x} - \tilde{\mathbf{x}})$. Therefore we can define a new tensor $\mathbf{C} = \bar{\mathbf{F}}^T \bar{\mathbf{F}}$, the right Cauchy-Green deformation tensor, such that $|\Phi(\mathbf{x}) - \Phi(\tilde{\mathbf{x}})|^2 \simeq (\mathbf{x} - \tilde{\mathbf{x}})^T \mathbf{C} (\mathbf{x} - \tilde{\mathbf{x}})$. This new tensor thus relates the distortion of distances in our domain to the deformation map Φ .

Rigid deformations

A special kind of homogeneous transformations are the so called rigid deformations. They possess the property that all the distances between points in our domain Ω_0 are invariant under these transformations. They are composed of translations and rotations and thus form indeed a subclass of the affine or homogeneous transformations. Translations are due to the constant vector \mathbf{c} in (3.7) whereas rotations are a result of $\bar{\mathbf{F}}$. In order to be a rotation $\bar{\mathbf{F}}$ must be an orthogonal matrix and thus $\bar{\mathbf{F}}^T \bar{\mathbf{F}} = \mathbf{I}$ must hold. As a result we know that $\mathbf{C} = \mathbf{I}$ for a rigid transformation, which indeed implies that $|\Phi(\mathbf{x}) - \Phi(\tilde{\mathbf{x}})|^2 = |\mathbf{x} - \tilde{\mathbf{x}}|^2$.

3.1.2 Displacement and strain

In addition to the description above in terms of deformations we can also write the preceding equations in terms of actual displacements. Given a point $\mathbf{x} \in \Omega_0$ we define the displacement-vector $\mathbf{u}(\mathbf{x}) = \Phi(\mathbf{x}) - \mathbf{x}$. With this new definition we can write $\Phi(\mathbf{x}) = \mathbf{u}(\mathbf{x}) + \mathbf{x}$ and therefore rewrite the aforementioned Cauchy-Green tensor in terms of u . This yields

$$\mathbf{C} = (\nabla \mathbf{u} + \mathbf{I})^T (\nabla \mathbf{u} + \mathbf{I}) = \mathbf{I} + (\nabla \mathbf{u})^T + \nabla \mathbf{u} + (\nabla \mathbf{u})^T \cdot \nabla \mathbf{u}. \quad (3.8)$$

A concept commonly encountered in continuum mechanics is *strain*, which is supposed to be a measure of the local difference between the actual deformation and a rigid deformation. In the preceding section it was shown that in the case of a homogeneous deformation there must hold $\mathbf{C} = \mathbf{I}$ whenever the transformation is rigid. Therefore a new tensor $\mathbf{E} = \frac{1}{2}(\mathbf{C} - \mathbf{I})$ can be introduced, the so called Green-Lagrange strain tensor. This tensor indeed vanishes if we have a rigid body transformation. Furthermore, it generalizes the one-dimensional Lagrange strain $\eta = \frac{1}{2}(\lambda^2 - 1)$ with λ the stretch ratio. Another measure for strain which is often encountered is the engineering strain. It is defined for one dimension as $\varepsilon = \frac{l-L}{L}$ and generalized to three dimensions as:

$$\varepsilon = \frac{1}{2}(\nabla \mathbf{u} + (\nabla \mathbf{u})^T). \quad (3.9)$$

We see that for small displacements \mathbf{u} (and thus neglecting $\mathcal{O}(|\mathbf{u}|^2)$) we have that $\varepsilon \approx \frac{1}{2}(\mathbf{C} - \mathbf{I}) = \mathbf{E}$, the engineering strain and Lagrange strain thus coincide.

3.1.3 Forces

In continuum mechanics a distinction is made between two different types of forces. On the one hand there are body forces, which act on a whole system $\Omega \subset \mathbf{R}^3$, for example gravity or electromagnetic forces which can penetrate a body and act on all its constituents. On the other hand there are forces which only act on a surface S and they are of course called surface forces. These surface forces are for example internal forces in a system which keep the system together and are thus cohesion forces. In both cases a (vector) force density function can be defined for

reasons to be shown in a minute, which after integrating over a suitable domain gives the total force

$$\mathbf{F}_{body} = \iiint_{\Omega} \mathbf{f}(\mathbf{x}) dV, \quad (3.10)$$

$$\mathbf{F}_{surface} = \iint_S \mathbf{T}(\mathbf{x}) dS. \quad (3.11)$$

The most interesting of these two, which is of great importance in continuum mechanics, is the surface force density $\mathbf{T}(\mathbf{x})$, also sometimes referred to as the stress vector. A very common made assumption on this density (introduced by Cauchy and nowadays known as Cauchy's Postulate) is that it only depends on the position $\mathbf{x} \in \Omega$ and on the normal vector \mathbf{n} to the surface S . It immediately follows from Newton's third law that we then must have that $\mathbf{T}(\mathbf{x}, \mathbf{n}) = -\mathbf{T}(\mathbf{x}, -\mathbf{n})$.

Cauchy stress tensor

The relation between the normal direction and the surface force density can be described by the so called Cauchy stress tensor $\boldsymbol{\sigma}$. This is a second order tensor such that

$$\mathbf{T}(\mathbf{x}, \mathbf{n}) = \mathbf{n} \cdot \boldsymbol{\sigma}(\mathbf{x}). \quad (3.12)$$

Components of the stress tensor are often written in the index notation σ_{ij} . Using the conservation of angular momentum it can be shown that the stress tensor's components are not independent, in fact the stress tensor is symmetric, i.e. $\sigma_{ij} = \sigma_{ji}$ [8]. This leaves us with 6 independent components. The stress tensor is often written in matrix form as:

$$\boldsymbol{\sigma} = \begin{pmatrix} \sigma_{xx} & \sigma_{xy} & \sigma_{xz} \\ \sigma_{xy} & \sigma_{yy} & \sigma_{yz} \\ \sigma_{xz} & \sigma_{yz} & \sigma_{zz} \end{pmatrix}. \quad (3.13)$$

3.1.4 Newton's laws for a continuum body

The goal of continuum mechanics is to rewrite the governing equations of mainly classical mechanics to equations for continuum material systems. Therefore we have to rewrite Newton's law and in particular his second law, $\mathbf{F}_{ext} = m\mathbf{a}$. Although we will only be interested in the static situations, for the moment we will also consider time-dependency. Therefore we look at a certain body $\Omega_t \subset \mathbf{R}^3$ at time t . The mass m is replaced by a mass-density-function $\rho(\mathbf{x}, t)$. The first step is then to rewrite the right-hand side using a continuum version of \mathbf{a} ,

$$\mathbf{F}_{ext} = \iiint_{\Omega_t} \rho(\mathbf{x}, t) \mathbf{a}(\mathbf{x}, t) dV = \iiint_{\Omega_t} \rho(\mathbf{x}, t) \frac{\partial^2 \Phi(\mathbf{x}, t)}{\partial t^2} dV = \iiint_{\Omega_t} \rho(\mathbf{x}, t) \frac{\partial^2 \mathbf{u}(\mathbf{x}, t)}{\partial t^2} dV. \quad (3.14)$$

After this we simply replace F_{ext} with the body and surface force equations that we saw earlier on. For the surface forces only the edge $\partial\Omega_t$ of the body Ω_t is considered, because only the external forces are of interest this time.

$$\iiint_{\Omega_t} \rho(\mathbf{x}, t) \frac{\partial^2 \mathbf{u}(\mathbf{x}, t)}{\partial t^2} dV = \mathbf{F}_{body} + \mathbf{F}_{surface} = \iiint_{\Omega_t} \mathbf{f}(\mathbf{x}, t) dV + \iint_{\partial\Omega_t} \mathbf{T}(\mathbf{x}, t) dS \quad (3.15)$$

Now this can be rewritten by using the stress-tensor and Stoke's Theorem,

$$\iiint_{\Omega_t} \rho(\mathbf{x}, t) \frac{\partial^2 \mathbf{u}(\mathbf{x}, t)}{\partial t^2} dV = \iiint_{\Omega_t} \mathbf{f}(\mathbf{x}, t) dV + \iint_{\partial\Omega_t} \mathbf{n}(\mathbf{x}) \cdot \boldsymbol{\sigma}(\mathbf{x}, t) dS \quad (3.16)$$

$$= \iiint_{\Omega_t} \mathbf{f}(\mathbf{x}, t) dV + \iiint_{\Omega_t} \nabla \cdot \boldsymbol{\sigma}(\mathbf{x}, t) dV \quad (3.17)$$

$$= \iiint_{\Omega_t} \mathbf{f}(\mathbf{x}, t) + \nabla \cdot \boldsymbol{\sigma}(\mathbf{x}, t) dV. \quad (3.18)$$

This expression can be written as one integral which equals zero,

$$\iiint_{\Omega_t} \mathbf{f}(\mathbf{x}, t) + \nabla \cdot \boldsymbol{\sigma}(\mathbf{x}, t) - \rho(\mathbf{x}, t) \frac{\partial^2 \mathbf{u}(\mathbf{x}, t)}{\partial t^2} dV = \mathbf{0}. \quad (3.19)$$

Since this holds for an arbitrary body we can omit the integrals [9] and find for every $t \in \mathbf{R}$ and $\mathbf{x} \in \Omega_t$ Newton's second law in continuum form:

$$\rho(\mathbf{x}, t) \frac{\partial^2 \mathbf{u}(\mathbf{x}, t)}{\partial t^2} = \mathbf{f}(\mathbf{x}, t) + \nabla \cdot \boldsymbol{\sigma}(\mathbf{x}, t) \quad \forall \mathbf{x} \in \Omega_t. \quad (3.20)$$

This partial differential equation must of course be accompanied by a set of boundary conditions which depend on the typical problem involved.

Equilibrium

For this thesis plays (almost) no role since we study equilibria, which are static deformations and configurations. As a result all time-dependency can be omitted most of the time and we thus arrive at the general equilibrium equations for a body $\Omega \subset \mathbf{R}^3$,

$$\mathbf{0} = \mathbf{f}(\mathbf{x}) + \nabla \cdot \boldsymbol{\sigma}(\mathbf{x}) \quad \forall \mathbf{x} \in \Omega. \quad (3.21)$$

3.2 Constitutive laws

When trying to solve the basis equations of continuum mechanics one needs to have as much equations as unknown variables. It is therefore convenient to check what the actual unknown variables in most of the problems are. If we assume that the density ρ is known* then we are left in general with the three components of displacement u and the stresses from the stress-tensor $\boldsymbol{\sigma}$. Since $\boldsymbol{\sigma}$ is symmetric there are six independent components and thus 6 unknowns in general. Therefore we are left in general with 9 unknowns.

If we now look at the equations (3.21) or (3.20) we come to the conclusion that so far only 3 equations have been derived and thus still 6 equations are missing. This is where the constitutive laws come into play, they will provide the missing equations. These laws do not follow from (classical) mechanics, but are the result of modelling and are therefore material specific. As a result, a large variety of different sets of equations can be found, all with their own applicability and validation. Here we will only briefly introduce the model which is of direct interest to the modelling of the non-linear behaviour of the Holey Sheet, namely the Neo-Hookean model. This model describes a non-linear elastic material and more specific a hyperelastic material.

*If ρ is not known an extra equation can easily be introduced, the continuity equation. This equation can be derived rather easily from the conservation of mass assumption[8].

However, before we go to this model, we first introduce a linear limit case, the Hookean model, which is mainly of interest for small deformations. Since this is a linear elastic model it will be much simpler than the Neo-Hookean model.

Almost all constitutive laws are stress-strain relations in the sense that they relate the stress σ to the strain $\varepsilon(\mathbf{u})$.

3.2.1 Hookean materials (linear)

When deformations are small it often suffices to describe the material by a linear stress-strain relation, i.e.

$$\sigma = c : \varepsilon, \quad (3.22)$$

which means:

$$\sigma_{ij} = \sum_{k=1}^3 \sum_{l=1}^3 c_{ijkl} \varepsilon_{kl}. \quad (3.23)$$

Note that since for the Hookean model only small displacements \mathbf{u} are considered it is equivalent to take ε or E as a strain measure since they are equal. The coefficients c_{ijkl} are called the elastic coefficients and in total there are 81 of them. However, for many materials having internal symmetries can reduce the amount of independent elastic coefficients drastically. In the case of an isotropic material the number of independent coefficients can even be reduced to two[10]. In this case the stress-strain relation can be given in terms of two independent elastic moduli. An elastic modulus is a number describing the reaction of the material to deformations due to an external force. Multiple elastic moduli are defined, all describing a different direction along which the force is applied, such as the Young's modulus which relates the axial strain to axial stresses. Other moduli which are often used are the shear modulus μ relating shear forces and strains, and the bulk modulus B , relating the volume change to an uniform applied load. A standard choice for the elastic moduli is to take the aforementioned Poisson's ratio ν (1.1), and the Young's modulus E . In terms of these parameters the relation takes on the form

$$\sigma = \frac{E\nu}{(1+\nu)(1-2\nu)} \text{tr}(\varepsilon) I + \frac{E}{1+\nu} \varepsilon. \quad (3.24)$$

The ease at which we can describe σ comes at the price that expression (3.24) is only valid for small deformations. In our case this means that as soon as the Holey Sheet starts to buckle we will need to reconsider the small deformation assumption made and therefore the use of this model. As a result this model will not be used in the numerical simulations. Although not of much use in the numerical analysis, this linear relation is a good description of the behaviour of a Holey Sheet before it has buckled, because deformations are rather small in the pre-buckling phase.

3.2.2 Neo-Hookean materials (non-linear)

Since we are interested in phenomena around the critical buckling point of the Holey Sheet, where displacements can become large, we need another constitutive law to fill the gap of the 6 missing equations. The domain of continuum mechanics which is concerned with these large displacements is often called Finite Strain Theory (FST) as opposed to its linearised counterpart Infinitesimal Strain Theory to which the Hookean model belongs.

One class of models in FST is the class of hyperelastic materials. These models are all based on a scalar quadratic energy functional $W(\bar{\mathbf{F}})$ [8] such that

$$\boldsymbol{\sigma} = \frac{1}{J} (\bar{\mathbf{F}} \cdot \nabla_{\bar{\mathbf{F}}^T} W(\bar{\mathbf{F}})). \quad (3.25)$$

Where $J = \det(\bar{\mathbf{F}})$ and thus J is a measure of volume change under the transformation Φ . The exact form of $W(\bar{\mathbf{F}})$ is the part where modelling must be used. One of these hyperelastic models is the Neo-Hookean model. It has the nice feature that for small displacements it coincides with the Hookean model if the correct parameters are chosen. However, if we go to large displacements it must deviate from the Hookean model as materials do not obey a linear relation any more. A function, such as W , which only depends on a tensor \mathbf{F} , should be independent of a change in coordinates by orthogonal transformations, such as rotations, and we call such functions objective. If a function is objective then it can be shown that the function depends only on invariants of $\bar{\mathbf{F}}$ [11]. The invariants can be chosen to be precisely the coefficients in the Cayley-Hamilton equation of the tensor. For the Neo-Hookean model one uses the left Cauchy-Green tensor $\mathbf{B} = \bar{\mathbf{F}} \cdot \bar{\mathbf{F}}^T$ and its invariants $I_1 = \text{tr}(\mathbf{B})$ and $I_3 = \det(\mathbf{B}) = J^2$ to describe W ,

$$W = \frac{\mu}{2} \left(I_1 I_3^{-\frac{1}{3}} - 3 \right) + \frac{B}{2} (\sqrt{I_3} - 1)^2 = \frac{\mu}{2} \left(I_1 J^{-\frac{2}{3}} - 3 \right) + \frac{B}{2} (J - 1)^2. \quad (3.26)$$

Here μ and B are the aforementioned shear and bulk modulus. They can both be expressed in terms of the aforementioned elastic parameters E and ν in three dimensions,

$$\mu = \frac{E}{2(1 + \nu)}, \quad B = \frac{E}{3(1 - 2\nu)}. \quad (3.27)$$

Using matrix and vector calculus [12] we can substitute (3.26) into (3.25) to derive the Neo-Hookean constitutive law,

$$\begin{aligned} \boldsymbol{\sigma} &= \mu J^{-\frac{5}{3}} \left(\mathbf{B} - \frac{1}{3} \text{tr}(\mathbf{B}) \mathbf{I} \right) + B (J - 1) \mathbf{I} \\ &= \frac{E}{2(1 + \nu)} J^{-\frac{5}{3}} \left(\mathbf{B} - \frac{1}{3} \text{tr}(\mathbf{B}) \mathbf{I} \right) + \frac{E}{3(1 - 2\nu)} (J - 1) \mathbf{I}. \end{aligned} \quad (3.28)$$

On close inspection we can see that this relation again yields a relation between $\boldsymbol{\sigma}$ and \mathbf{u} , which is precisely what is needed to close our system of equations.

As a limit case for small displacements this law should return the Hookean-model. To see this we take $|\mathbf{u}| \ll 1$ and thus $\mathbf{B} \approx \mathbf{I} + 2\boldsymbol{\varepsilon}$. Then we know that $J = \det(\mathbf{F}) \approx 1 + \text{tr}(\boldsymbol{\varepsilon})$ and $\text{tr}(\mathbf{B}) \approx 3 + 2\text{tr}(\boldsymbol{\varepsilon})$ [12]. Inserting this all and neglecting quadratic terms in $\boldsymbol{\varepsilon}$ we get

$$\begin{aligned} \boldsymbol{\sigma} &= \frac{E}{2(1 + \nu)} J^{-\frac{5}{3}} \left(\mathbf{B} - \frac{1}{3} \text{tr}(\mathbf{B}) \mathbf{I} \right) + \frac{E}{3(1 - 2\nu)} (J - 1) \mathbf{I} \\ &\approx \frac{E}{2(1 + \nu)} (1 + \text{tr}(\boldsymbol{\varepsilon}))^{-\frac{5}{3}} \left(\mathbf{I} + 2\boldsymbol{\varepsilon} - \frac{1}{3}(3 + 2\text{tr}(\boldsymbol{\varepsilon})) \mathbf{I} \right) + \frac{E}{3(1 - 2\nu)} (1 + \text{tr}(\boldsymbol{\varepsilon}) - 1) \mathbf{I} \\ &= \frac{E}{2(1 + \nu)} (1 + \text{tr}(\boldsymbol{\varepsilon}))^{-\frac{5}{3}} \left(2\boldsymbol{\varepsilon} - \frac{2}{3}\text{tr}(\boldsymbol{\varepsilon}) \mathbf{I} \right) + \frac{E}{3(1 - 2\nu)} \text{tr}(\boldsymbol{\varepsilon}) \mathbf{I} \\ &\approx \frac{E}{2(1 + \nu)} \left(2\boldsymbol{\varepsilon} - \frac{2}{3}\text{tr}(\boldsymbol{\varepsilon}) \mathbf{I} \right) + \frac{E}{3(1 - 2\nu)} \text{tr}(\boldsymbol{\varepsilon}) \mathbf{I} \\ &= \frac{E\nu}{(1 + \nu)(1 - 2\nu)} \text{tr}(\boldsymbol{\varepsilon}) \mathbf{I} + \frac{E}{1 + \nu} \boldsymbol{\varepsilon} \end{aligned} \quad (3.29)$$

which is precisely the Hookean law. The Neo-Hookean model is the constitutive law of choice in this project. Although the Neo-Hookean model is quite an old model and since its invention many other models have been created [11], it is one of the standard choices for non-linear elastic analysis.

3.3 Plane strain

The Holey Sheet is a three-dimensional structure as it has a certain depth d which is much larger than the filament thickness t . If we choose our axis such that the surface \mathcal{A} with the holes of the Holey Sheet lies in the x, y -plane, then the direction of the depth will be denoted by the z -coordinate. When compressing the Holey, it is not expected that there is a dependency in the behaviour on z . Furthermore, no substantial displacement or force is expected in the z direction as well. These assumptions lead to the so called plane strain framework of continuum mechanics[13]. As a result, we can write for the displacement vector \mathbf{u} and force vector \mathbf{f}

$$\mathbf{u} = \begin{pmatrix} u_1(x, y) \\ u_2(x, y) \\ 0 \end{pmatrix} = \begin{pmatrix} \tilde{\mathbf{u}}(x, y) \\ 0 \end{pmatrix}, \quad \mathbf{f} = \begin{pmatrix} f_1(x, y) \\ f_2(x, y) \\ 0 \end{pmatrix} = \begin{pmatrix} \tilde{\mathbf{f}}(x, y) \\ 0 \end{pmatrix}. \quad (3.30)$$

Upon inspection of equation (3.8), we see that our strain tensors, both engineering and Green-Lagrange, will have a more economical form. For the engineering strain we can derive that

$$\boldsymbol{\varepsilon} = \begin{pmatrix} \varepsilon_{xx} & \varepsilon_{xy} & 0 \\ \varepsilon_{xy} & \varepsilon_{yy} & 0 \\ 0 & 0 & 0 \end{pmatrix}. \quad (3.31)$$

But this also has implications for the stress-tensor $\boldsymbol{\sigma}$ as these are related by a constitutive law. Assuming the Hookean law we can show, using (3.24), that

$$\boldsymbol{\sigma} = \begin{pmatrix} \sigma_{xx} & \sigma_{xy} & 0 \\ \sigma_{xy} & \sigma_{yy} & 0 \\ 0 & 0 & \sigma_{zz} \end{pmatrix} = \begin{pmatrix} \tilde{\boldsymbol{\sigma}} & \mathbf{0} \\ \mathbf{0}^T & \sigma_{zz} \end{pmatrix}. \quad (3.32)$$

Since there is no dependency on z , our equilibrium equations (3.21) simplify to two equations instead of three:

$$\tilde{\mathbf{f}}(x, y) + \tilde{\nabla} \cdot \tilde{\boldsymbol{\sigma}}(x, y) = \mathbf{0} \quad \forall (x, y) \in \mathcal{A}, \quad (3.33)$$

where $\tilde{\nabla}$ is the two-dimensional del operator. This must be accompanied by the equation for the out-of-plane stress $\sigma_{zz} = \nu(\sigma_{xx} + \sigma_{yy})$. However, since we are interested in the behaviour in the plane, we can neglect this equation and only mention it for completeness. In rewriting the Hookean law one can find new relations between the elastic moduli which are valid for the plane strain formulation instead of the three-dimensional one.

Elastic moduli in plane strain

Following Jasluk et al.[14] we can derive the relations between the three-dimensional elastic moduli and the two-dimensional elastic moduli. This is needed, because in the experiments and simulations the elastic moduli for three dimensions are known or given, but we transfer our problem to the plane strain formulation with accompanying elastic moduli. We will from now

on denote the three-dimensional elastic moduli primed, i.e. $E_{3D} = E'$, and the two-dimensional ones unprimed, i.e. $E_{2D} = E$. The Hookean law simplifies in plane strain to

$$\begin{pmatrix} \sigma_{xx} \\ \sigma_{yy} \\ \sigma_{xy} \end{pmatrix} = \frac{E'}{(1 + \nu')(1 - 2\nu')} \begin{pmatrix} 1 - \nu' & \nu' & 0 \\ \nu' & 1 - \nu' & 0 \\ 0 & 0 & 1 - 2\nu' \end{pmatrix} \begin{pmatrix} \varepsilon_{xx} \\ \varepsilon_{yy} \\ \varepsilon_{xy} \end{pmatrix}. \quad (3.34)$$

To derive an expression for ν we apply a stress along the x -axis only, so $\sigma_{yy} = \sigma_{xy} = 0$ and then we find the relation

$$0 = \frac{E'}{(1 + \nu')(1 - 2\nu')} ((1 - \nu')\varepsilon_{yy} + \nu'\varepsilon_{xx}). \quad (3.35)$$

This can be rewritten to

$$(1 - \nu')\varepsilon_{yy} = -\nu'\varepsilon_{xx}. \quad (3.36)$$

The Poisson's ratio is defined equivalent to (1.1) and thus reads

$$\nu = -\frac{\varepsilon_{yy}}{\varepsilon_{xx}} = \frac{\nu'}{1 - \nu'}. \quad (3.37)$$

In a similar fashion we can derive E , as it is the ratio of the axial stress to the axial strain. If we apply a stress σ_{xx} then we find

$$E = \frac{\sigma_{xx}}{\varepsilon_{xx}} = \frac{E'}{(1 + \nu')(1 - 2\nu')\varepsilon_{xx}} ((1 - \nu')\varepsilon_{xx} + \nu'\varepsilon_{yy}). \quad (3.38)$$

Using the Poisson's ratio this can then be rewritten to

$$E = \frac{E'}{(1 + \nu')(1 - 2\nu')} \left((1 - \nu') - \frac{\nu'^2}{1 - \nu'} \right) = \frac{E'}{1 - \nu'^2} \quad (3.39)$$

Finally we can derive an expression for the bulk modulus B , which we will use later on. The bulk modulus relates the stress σ , applied uniformly to the body, to the relative volume change $\frac{\Delta V}{V}$ of an unit volume. Since we are now in two dimensions this changes to the relative area change, $\frac{\Delta A}{A}$. For a unit area, a square, we find that up to first order approximation that

$$\frac{\Delta A}{A} = \frac{A(1 + \varepsilon_{xx})(1 + \varepsilon_{yy}) - A}{A} \approx \varepsilon_{xx} + \varepsilon_{yy} = 2\varepsilon, \quad (3.40)$$

because the strains are equal in each direction. Therefore the relation between stress and strain is

$$\sigma = 2B\varepsilon. \quad (3.41)$$

Upon inspection of (3.34) we derive that

$$\sigma = \sigma_{xx} = \frac{E'}{(1 + \nu')(1 - 2\nu')} ((1 - \nu') + \nu') \varepsilon = \frac{E'}{(1 + \nu')(1 - 2\nu')} \varepsilon. \quad (3.42)$$

Thus the bulk modulus B is related to the other elastic moduli by

$$B = \frac{E'}{2(1 + \nu')(1 - 2\nu')} = \frac{E}{2(1 - \nu)}. \quad (3.43)$$

These relations allow us to compare the two-dimensional results to the ones as measured in the laboratory on three-dimensional samples.

This page would be intentionally left blank if we would not wish to inform about that.

Non-linear numerical analysis of elastic materials

As mentioned in the introduction, it is experimentally difficult and time-consuming to perform a parameter study on the influence of the hole-size in the Holey Sheet. One way to overcome this problem is by performing accompanying numerical experiments on the Holey Sheet. This procedure is highly flexible in nature since one can easily vary the size, geometry, material properties and boundary conditions of the sheet. Furthermore, circumstances which might be very hard to achieve in experiments can be created in numerics rather easily. Therefore, the numerical study of the Holey Sheet forms the main body of this thesis.

In addition to the aforementioned advantages, the numerical methods are extremely suitable for the study of size-effects due to the scalability of the numerical procedures. The unit-cell introduced in the introduction will be the domain studied in our simulations. The option to use the plane strain formalism in combination with this relatively small system, allows us to computationally explore the effect of the hole-size in the Holey Sheet.

This chapter provides a brief introduction into the Finite Elements Method applied to elasticity problems. This method is the method used to perform numerical studies of the Holey Sheet. Additionally, some notes on numerical buckling analysis are given, since it is of great importance for the study of behaviour around the buckling point of the Holey Sheet.

4.1 Finite element method for elasticity problems

Numerical simulations on a Holey Sheet basically need to solve the elastic equations (3.21) numerically on the domain of the sheet. There are a lot of different methods available for solving (partial) differential equations approximately and one of the better known is the method of finite differences (FD). This method first discretizes the domain on which the equations need to be solved and then approximates all derivatives in the equations by algebraic difference formulas between nearby grid-points [15]. This method is normally very easy to implement and provides good measures for the approximation errors. Therefore this method is widely used in branches where numerics are needed to solve differential equations. However, if the domain becomes sufficiently complicated (such as a Holey Sheet) FD becomes hard to implement due to the fact that it gets more difficult to specify which points are needed in the approximation of each derivative in each point. One has to rely on other numerical methods in this case. One of these methods to solve differential equations on complicated domains is the finite elements method (FEM)[16]. A crucial ingredient for this method is an alternative formulation of the governing

differential equations, known as the weak formulation.

4.1.1 Weak formulation

To begin with, we repeat the equations for a solid material in equilibrium and formulate the two most encountered type boundary conditions related to these equations. Let $\Omega \subset \mathbf{R}^3$ be a body and $\partial\Omega$ its edge. Then we know that in equilibrium must hold

$$\mathbf{0} = \mathbf{f}(\mathbf{x}) + \nabla \cdot \boldsymbol{\sigma}(\mathbf{x}) \quad \forall \mathbf{x} \in \Omega. \quad (4.1)$$

Furthermore, on parts of the edge we can prescribe a displacement $\bar{\mathbf{u}}$ or a surface-force $\bar{\mathbf{T}}$. The edge $\partial\Omega$ will be divided in $\Gamma_d \subseteq \partial\Omega$ and $\Gamma_f \subseteq \partial\Omega$ such that

$$\bar{\mathbf{u}}(\mathbf{x}) - \mathbf{u}(\mathbf{x}) = \mathbf{0} \quad \forall \mathbf{x} \in \Gamma_d, \quad (4.2)$$

$$\bar{\mathbf{T}}(\mathbf{x}) - \mathbf{n}(\mathbf{x}) \cdot \boldsymbol{\sigma}(\mathbf{x}) = \mathbf{0} \quad \forall \mathbf{x} \in \Gamma_f. \quad (4.3)$$

If these equations have to hold everywhere inside the body Ω and on its edge than for an (almost) arbitrary function $\delta v : \mathbf{R}^3 \rightarrow \mathbf{R}^3$ it must be the case that

$$\mathbf{0} = \iiint_{\Omega} (\mathbf{f}(\mathbf{x}) + \nabla \cdot \boldsymbol{\sigma}(\mathbf{x})) \cdot \delta v(\mathbf{x}) dV, \quad (4.4)$$

$$\mathbf{0} = \iint_{\Gamma_f} (\bar{\mathbf{T}}(\mathbf{x}) - \mathbf{n}(\mathbf{x}) \cdot \boldsymbol{\sigma}(\mathbf{x})) \cdot \delta v(\mathbf{x}) dA, \quad (4.5)$$

$$\mathbf{0} = \bar{\mathbf{u}}(\mathbf{x}) - \mathbf{u}(\mathbf{x}) \quad \forall \mathbf{x} \in \Gamma_d. \quad (4.6)$$

This is the so-called weak formulation. The function δv cannot be completely arbitrary since we are only interested in those functions for which the aforementioned integrals converge and therefore in general we would like δv to be at least a bounded function over Ω . Furthermore we put the restriction on δv that it must be equal to zero on Γ_d , which can be justified if we see δv as a perturbation to the displacement field \mathbf{u} in combination with equation (4.6). 'Arbitrary' functions which satisfy the aforementioned assumptions are known as kinematically admissible virtual velocity fields in continuum mechanics. The weak formulation is also known by the name of the principle of virtual work. This can be understood if we indeed regard δv as a displacement, because then the integrals in the weak formulation are integrals over force times displacement which gives work. Because we have a virtual displacement, the work done by it is also called virtual work.

Although the name suggests that this formulation is in some sense inferior to the original formulation, (4.1), (4.2) and (4.3), it can be easily proven that if the weak formulation holds for every δv the equations of the strong formulation are automatically satisfied as well. To see this we assume that the weak formulation is valid for every δv and then we suppose that there is a region where the strong formulation does not hold. As a result, a function δv can be found which is non-zero over this region. This implies that the integrals of the weak formulation don't vanish any more, which in turn contradicts the weak formulation. Therefore the strong formulation must hold. This makes the strong and weak formulation equivalent in some sense.

Now equations (4.4) and (4.5) can be combined and rewritten with the help of product rule for

differentiation and the divergence theorem,

$$\begin{aligned}
0 &= \iiint_{\Omega} (\mathbf{f}(\mathbf{x}) + \nabla \cdot \boldsymbol{\sigma}(\mathbf{x})) \cdot \delta v(\mathbf{x}) dV + \iint_{\Gamma_f} (\bar{\mathbf{T}}(\mathbf{x}) - \mathbf{n}(\mathbf{x}) \cdot \boldsymbol{\sigma}(\mathbf{x})) \cdot \delta v(\mathbf{x}) dA \\
&= \iiint_{\Omega} \mathbf{f}(\mathbf{x}) \cdot \delta v(\mathbf{x}) + \nabla(\boldsymbol{\sigma}(\mathbf{x}) \cdot \delta v(\mathbf{x})) - \boldsymbol{\sigma}(\mathbf{x}) : (\nabla \delta v(\mathbf{x})) dV \\
&\quad + \iint_{\Gamma_f} (\bar{\mathbf{T}}(\mathbf{x}) - \mathbf{n}(\mathbf{x}) \cdot \boldsymbol{\sigma}(\mathbf{x})) \cdot \delta v(\mathbf{x}) dA \\
&= \iiint_{\Omega} \mathbf{f}(\mathbf{x}) \cdot \delta v(\mathbf{x}) - \boldsymbol{\sigma}(\mathbf{x}) : (\nabla \delta v(\mathbf{x})) dV + \iint_{\partial\Omega} (\mathbf{n}(\mathbf{x}) \cdot \boldsymbol{\sigma}(\mathbf{x})) \cdot \delta v(\mathbf{x}) dA \\
&\quad + \iint_{\Gamma_f} (\bar{\mathbf{T}}(\mathbf{x}) - \mathbf{n}(\mathbf{x}) \cdot \boldsymbol{\sigma}(\mathbf{x})) \cdot \delta v(\mathbf{x}) dA \\
&= \iiint_{\Omega} f(\mathbf{x}) \cdot \delta v(\mathbf{x}) - \boldsymbol{\sigma}(\mathbf{x}) : (\nabla \delta v(\mathbf{x})) dV + \iint_{\Gamma_f} \bar{\mathbf{T}}(\mathbf{x}) \cdot \delta v(\mathbf{x}) dA + \iint_{\Gamma_d} (\mathbf{n}(\mathbf{x}) \cdot \boldsymbol{\sigma}(\mathbf{x})) \cdot \delta v(\mathbf{x}) dA \\
&= - \iiint_{\Omega} \boldsymbol{\sigma}(\mathbf{x}) : (\nabla \delta v(\mathbf{x})) dV + \iiint_{\Omega} \mathbf{f}(\mathbf{x}) \cdot \delta v(\mathbf{x}) dV + \iint_{\Gamma_f} \bar{\mathbf{T}}(\mathbf{x}) \cdot \delta v(\mathbf{x}) dA
\end{aligned} \tag{4.7}$$

We can rewrite this slightly using the fact that $\boldsymbol{\sigma}$ is symmetric,

$$\begin{aligned}
\boldsymbol{\sigma} : (\nabla \delta v) &= \frac{1}{2}(\boldsymbol{\sigma} : (\nabla \delta v) + \boldsymbol{\sigma} : (\nabla \delta v)) \\
&= \frac{1}{2}(\boldsymbol{\sigma} : (\nabla \delta v) + \text{tr}(\boldsymbol{\sigma}(\nabla \delta v)^T)) \\
&= \frac{1}{2}(\boldsymbol{\sigma} : (\nabla \delta v) + \text{tr}((\nabla \delta v)^T \boldsymbol{\sigma})) \\
&= \frac{1}{2}(\boldsymbol{\sigma} : (\nabla \delta v) + \text{tr}(\boldsymbol{\sigma}^T(\nabla \delta v))) \\
&= \frac{1}{2}(\boldsymbol{\sigma} : (\nabla \delta v) + \text{tr}(\boldsymbol{\sigma}(\nabla \delta v))) \\
&= \frac{1}{2}(\boldsymbol{\sigma} : (\nabla \delta v) + \boldsymbol{\sigma} : (\nabla \delta v)^T) \\
&= \boldsymbol{\sigma} : \frac{1}{2}((\nabla \delta v) + (\nabla \delta v)^T) \\
&= \boldsymbol{\sigma} : \delta \mathbf{D}
\end{aligned} \tag{4.8}$$

Where now $\delta \mathbf{D}$ represents a virtual engineering strain. This yields the weak formulation relation

$$-\iiint_{\Omega} \boldsymbol{\sigma}(\mathbf{x}) : \delta \mathbf{D}(\mathbf{x}) dV + \iiint_{\Omega} \mathbf{f}(\mathbf{x}) \cdot \delta v(\mathbf{x}) dV + \iint_{\Gamma_f} \bar{\mathbf{T}}(\mathbf{x}) \cdot \delta v(\mathbf{x}) dA = 0. \tag{4.9}$$

This is not necessarily an easier problem to solve than the strong formulation if we need to solve this for every kinematically admissible δv . However, we were interested in a numerical approximation and that is exactly what FEM does. It does not solve for every δv but instead for a subspace of $B(\Omega)$, the space of all bounded functions on Ω , which is often called the test-space V . This approach is often called the Galerkin-approach.

4.1.2 Test-space

A crucial choice in the FEM is that of the test-space. A smart choice for a test-space would be a space of which a basis is known, say b_1, \dots, b_n . The advantage then is that we can expand

our arbitrary virtual velocity field δv on this basis, $\delta v = \sum_i \mathbf{c}_i b_i$ where now \mathbf{c}_i are the arbitrary coefficients and b_i the basis functions. In the FEM we choose to take the basis functions to be scalar functions and therefore the coefficients are vector-valued. If this expansion is then substituted in (4.7) we get

$$\sum_{i=1}^n \left[- \iiint_{\Omega} \nabla b_i(\mathbf{x}) \cdot \boldsymbol{\sigma}(\mathbf{x}) dV + \iiint_{\Omega} b_i(\mathbf{x}) \mathbf{f}(\mathbf{x}) dV + \iint_{\Gamma_f} b_i(\mathbf{x}) \bar{\mathbf{T}}(\mathbf{x}) dA \right] \cdot \mathbf{c}_i = 0. \quad (4.10)$$

and since this equation must hold for arbitrary parameters \mathbf{c}_i , the result of our particular choice of a test-space is a system of n vector-equations,

$$- \iiint_{\Omega} \nabla b_i(\mathbf{x}) \cdot \boldsymbol{\sigma}(\mathbf{x}) dV + \iiint_{\Omega} b_i(\mathbf{x}) \mathbf{f}(\mathbf{x}) dV + \iint_{\Gamma_f} b_i(\mathbf{x}) \bar{\mathbf{T}}(\mathbf{x}) dA = 0 \quad i = 1, \dots, n. \quad (4.11)$$

This leaves us still with n unknown basis functions which we need to choose. The core idea of the FEM is to choose these basis functions by first discretizing the domain to create a mesh covering the original domain and then to define a class of functions on this mesh. This discretization is mostly done by tiling the domain with polygons which are called elements (hence the name FEM). When considering two dimensional problems, one mostly uses triangular or quadrilateral elements to tile the domain, see f.e. figure 4.12. If the domain is a polygon it can be completely tiled by these small polygons, however if the domain differs from a polygon, for example if it is a circle, then an approximation of the domain will be made. The quality of this approximation depends on the size of the elements, the smaller they are the better the approximation.

Each resulting element consists of a number of nodes, see figure 4.1. The number of the nodes and their position depends on the type of element and the order of the elements. For example a linear quadrilateral element will only have nodes on its four vertices whereas a quadratic quadrilateral element has not only nodes at its vertices but at the middle of their edges and at the intersection of its bi-medians as well. The result of this discretization procedure is a set of nodes and it is on these nodes that the displacement field will be calculated.

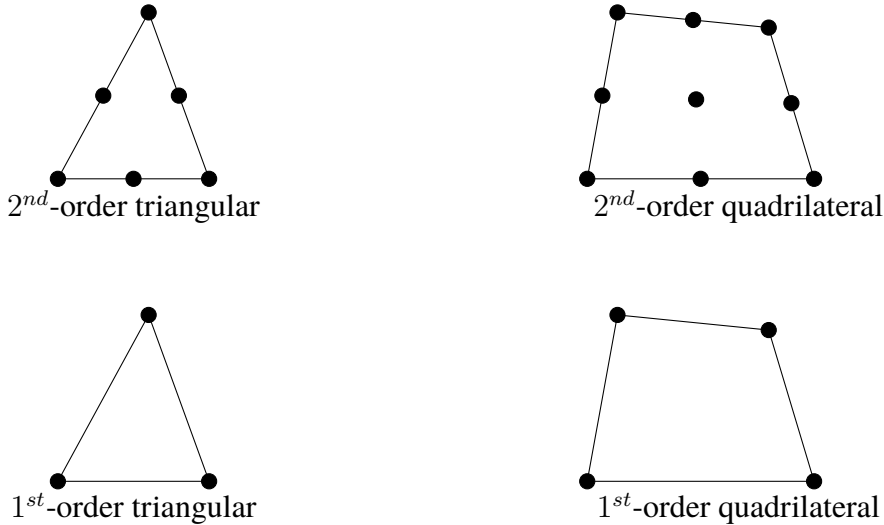


Figure 4.1: Nodal position for triangular and quadrilateral elements of first and second order for Lagrange shape functions.

In most practical and traditional implementations of FEM piecewise linear or quadratic functions on the nodes of elements are used as basis functions, known as shape functions. The order of the elements basically defines the number of nodes of an element and thus the number of degrees of freedom one has in choosing parameters of a test function. Therefore it determines the order of the approximation polynomials used on the elements. Here we will only cover the simplest type of shape functions, the Lagrange interpolation polynomials. A myriad of different shape functions does exist[16], but the underlying idea is the same.

Lagrange shape functions

We denote the shape functions by $N_i(\mathbf{x})$ and the nodal positions by \mathbf{x}^a where a is the number of the node, both i and a lie between 1 and n . Since we want to approximate the displacements on the nodes we impose the following condition:

$$N_i(\mathbf{x}^a) = \delta_{ia} \quad (4.12)$$

where δ_{ia} is the Kronecker delta function. Many possible ways exist to fulfil this condition, but as said, we will only describe one option, the Lagrange interpolation polynomials. Given $k+1$ points on a line x_1, \dots, x_{k+1} , the k -th order Lagrange basis polynomials are defined as:

$$l_j^k(x) = \prod_{\substack{i=1 \\ i \neq j}}^k \frac{x - x_i}{x_j - x_i}. \quad (4.13)$$

These polynomials are exactly such that $l_j(x_i) = \delta_{ij}$. We can use these interpolation polynomials to define element shape functions. If we want to create multidimensional element shape functions we can simply multiply multiple Lagrange basis polynomials. Let $\mathbf{x} = (\zeta, \eta) \in \mathbf{R}^2$, and suppose that $\mathbf{x}^i = (\zeta_{i'}, \eta_{i''})$, then

$$N_i(\mathbf{x}) = l_{i'}^\alpha(\zeta) l_{i''}^\beta(\eta). \quad (4.14)$$

The order of the element shape functions is determined by the number of nodes as was mentioned before. A few of the low order element shape functions are given in figures 4.2 and 4.3.

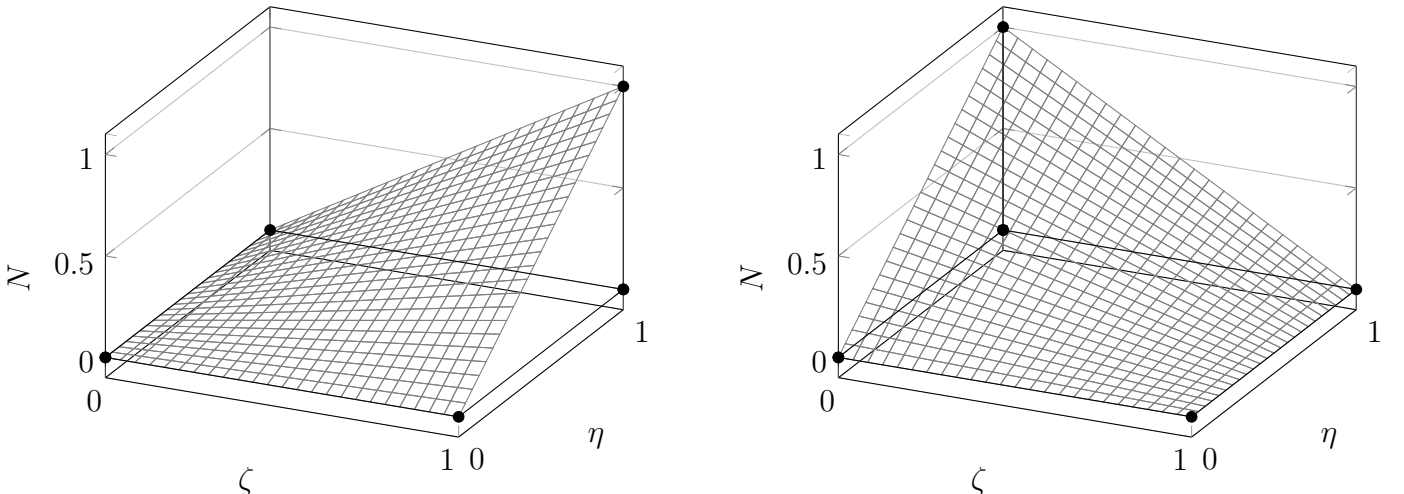


Figure 4.2: Plots of 2 of the possible 4 linear order Lagrangian element shape functions on a quadrilateral element.

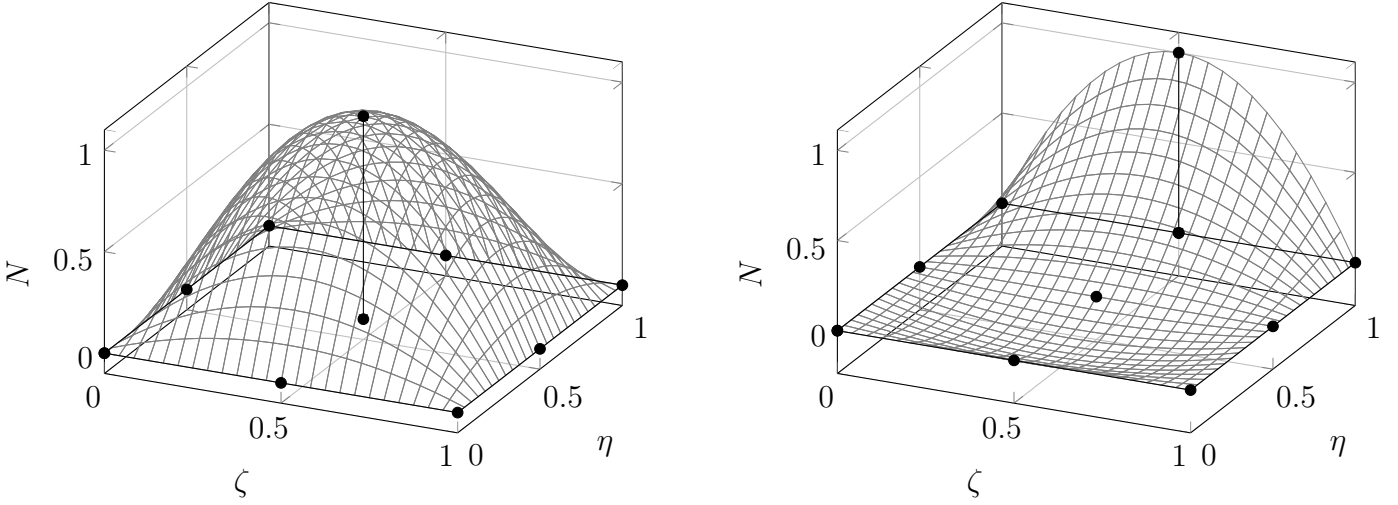


Figure 4.3: Plots of 2 of the possible 9 quadratic order Lagrangian element shape functions on a quadrilateral element.

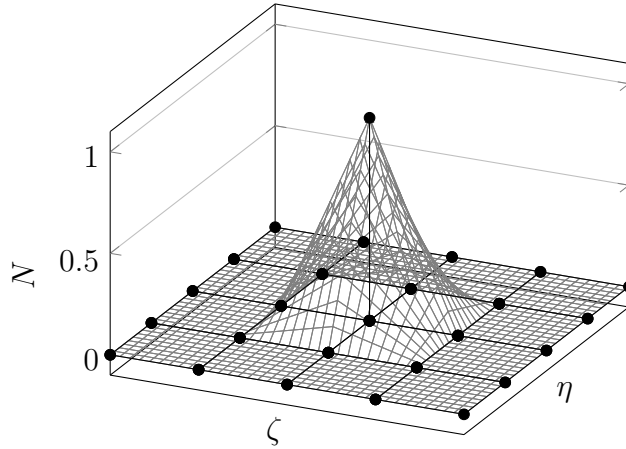


Figure 4.4: Combination of Lagrangian element shape functions (linear order) to create a shape function on a whole domain Ω .

To define the shape functions $N_i(\mathbf{x})$ on the whole domain Ω one combines element shape functions such that equation (4.12) is satisfied, see figure 4.4.

To see how many nodes are needed for a given polynomial order we look at the number of degrees of freedom for a n -th order two dimensional polynomial. This can be done by constructing a Pascal triangle 4.5. Each level of the triangle represents an order for the polynomial and we see the number of degrees of freedom needed for higher order polynomials growing rapidly. Although higher order polynomials will improve convergence in general they also need more nodes and therefore more calculations will be involved (larger system of equations). Therefore only first and second order polynomials are used in most practical implementations of the FEM. In the above derivation of shape functions only rectangular elements are used. However, in real analysis elements are likely to deviate from this perfect rectangle, f.e. in the Holey Sheet. In this case the shape functions are mapped from rectangles onto the true quadrilateral elements via a coordinate transformation [16].

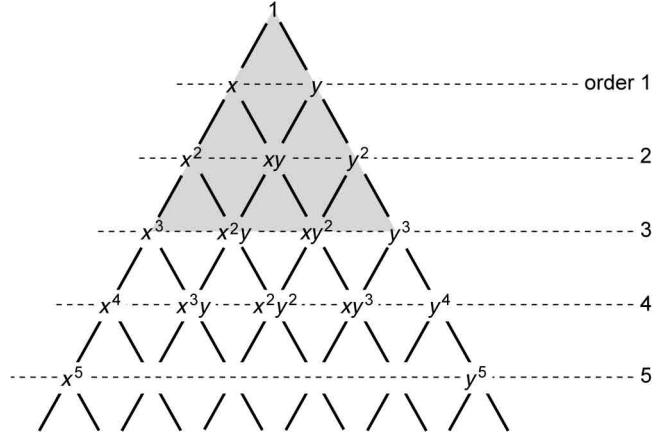


Figure 4.5: Pascal triangle showing number of degrees of freedom in a two dimensional polynomial of order n .[16]

4.1.3 Search-space

Having determined a suitable test-space results in an under-determined system of equations since we haven't used our constitutive law yet. This law will get rid of the appearance of $\sigma(x)$ in our system. The crucial remark here is that our constitutive law will yield a relation between σ and \mathbf{u} and therefore we will end up with an expression involving \mathbf{u} which is still unknown. However, now the number of equations and the number of unknowns match and therefore \mathbf{u} could be calculated from the resulting equations. These equations are as follows,

$$-\iiint_{\Omega} \nabla N_i(\mathbf{x}) \cdot \boldsymbol{\sigma}[\mathbf{u}(\mathbf{x})] dV + \iiint_{\Omega} N_i(\mathbf{x}) \mathbf{f}(\mathbf{x}) dV + \iint_{\Gamma_f} N_i(\mathbf{x}) \bar{\mathbf{T}}(\mathbf{x}) dA = 0 \quad i = 1, \dots, n. \quad (4.15)$$

Unfortunately, these equations are in no way easy to solve and therefore FEM makes another approximation as well, we look for the 'best possible' \mathbf{u} in a certain search-space. If we choose the search-space different from our test-space the procedure is called a Petrov-Galerkin approach. However, we can just as easily take the test-space and search-space equal and that is what most of the FEM implementations do. Therefore we expand $\mathbf{u}(\mathbf{x})$ on the same basis,

$$\mathbf{u}(\mathbf{x}) = \sum_{i=1}^n N_i(\mathbf{x}) \mathbf{u}_i, \quad (4.16)$$

where \mathbf{u}_i are the unknown coefficients which we want to compute. The exact form of σ determines the set of equations that needs to be solved. We'll first explain the most simple case, the linear Hookean model and thereafter we'll consider the more involved non-linear case which is more applicable to the simulations carried out for this thesis.

Hookean model (linear)

To derive the FEM equations for Hooke's law we start with the following equations:

$$\mathbf{u}(\mathbf{x}) = \sum_{i=1}^n N_i(\mathbf{x}) \mathbf{u}_i; \quad (4.17)$$

$$\delta v(\mathbf{x}) = \sum_{i=1}^n N_i(\mathbf{x}) \mathbf{c}_i; \quad (4.18)$$

$$0 = - \iiint_{\Omega} \boldsymbol{\sigma}(\mathbf{x}) : \delta \mathbf{D}(\mathbf{x}) dV + \iiint_{\Omega} \mathbf{f}(\mathbf{x}) \cdot \delta v(\mathbf{x}) dV + \iint_{\Gamma_f} \bar{\mathbf{T}}(\mathbf{x}) \cdot \delta v(\mathbf{x}) dA; \quad (4.19)$$

$$\boldsymbol{\sigma} = \frac{E\nu}{(1+\nu)(1-2\nu)} \text{tr}(\boldsymbol{\varepsilon}) I + \frac{E}{1+\nu} \boldsymbol{\varepsilon} = \lambda \text{tr}(\boldsymbol{\varepsilon}) \mathbf{I} + 2\mu \boldsymbol{\varepsilon}; \quad (4.20)$$

$$0 = \bar{\mathbf{u}}(\mathbf{x}) - \mathbf{u}(\mathbf{x}) \quad \forall \mathbf{x} \in \Gamma_d. \quad (4.21)$$

Combining these equations we get to the following equation,s

$$0 = \sum_{i=1}^n \left(\sum_{j=1}^n -\mathbf{u}_j^T \left[\lambda \iiint_{\Omega} (\nabla N_i(\mathbf{x})) (\nabla N_j(\mathbf{x}))^T dV \right. \right. \\ \left. \left. + \mu \iiint_{\Omega} ((\nabla N_j(\mathbf{x})) (\nabla N_i(\mathbf{x}))^T + (\nabla N_i(\mathbf{x})) (\nabla N_j(\mathbf{x}))^T) dV \right] \right. \\ \left. + \iiint_{\Omega} N_i(\mathbf{x}) \mathbf{f}(\mathbf{x}) dV + \iint_{\Gamma_f} N_i(\mathbf{x}) \bar{\mathbf{T}}(\mathbf{x}) dA \right) \cdot \mathbf{c}_i. \quad (4.22)$$

Because the \mathbf{c}_i are arbitrary we have for $i = 1, \dots, n$ that

$$0 = \sum_{j=1}^n -\mathbf{u}_j^T \left[\lambda \iiint_{\Omega} (\nabla N_i(\mathbf{x})) (\nabla N_j(\mathbf{x}))^T dV \right. \\ \left. + \mu \iiint_{\Omega} ((\nabla N_j(\mathbf{x})) (\nabla N_i(\mathbf{x}))^T + (\nabla N_i(\mathbf{x})) (\nabla N_j(\mathbf{x}))^T) dV \right], \\ + \iiint_{\Omega} N_i(\mathbf{x}) \mathbf{f}(\mathbf{x}) dV + \iint_{\Gamma_f} N_i(\mathbf{x}) \bar{\mathbf{T}}(\mathbf{x}) dA \quad (4.23)$$

which is the FEM system to be solved for linear elasticity problems. From this system one needs to solve the unknown \mathbf{u}_j . Another common way to rewrite this system is in matrix-vector notation. In order to do so we define $\mathbf{U} = [\mathbf{u}_1 \ \mathbf{u}_2 \ \dots \ \mathbf{u}_n]^T$ and write the system as

$$\mathbf{U}^T \mathbf{K} = \mathbf{F}^T, \quad (4.24)$$

with the external force vector \mathbf{F}

$$\mathbf{F}_i^T = \iiint_{\Omega} N_i(\mathbf{x}) \mathbf{f}(\mathbf{x}) dV + \iint_{\Gamma_f} N_i(\mathbf{x}) \bar{\mathbf{T}}(\mathbf{x}) dA, \quad (4.25)$$

and the $n \times n$ stiffness matrix \mathbf{K}

$$\mathbf{K}_{ji} = \lambda \iiint_{\Omega} (\nabla N_i(\mathbf{x})) (\nabla N_j(\mathbf{x}))^T dV + \mu \left(\iiint_{\Omega} ((\nabla N_j(\mathbf{x})) (\nabla N_i(\mathbf{x}))^T + (\nabla N_i(\mathbf{x})) (\nabla N_j(\mathbf{x}))^T) dV \right). \quad (4.26)$$

The system of equations to be solved is generally written in the transposed form as

$$\mathbf{K} \mathbf{U} = \mathbf{F}. \quad (4.27)$$

To solve such a system, which often involves large matrices, advanced techniques can be applied which are outside the scope of this thesis [17]. When \mathbf{u} has been extracted, $\boldsymbol{\sigma}$ can be computed as well by simply substituting the approximation of \mathbf{u} in the constitutive law.

Neo-Hookean model (non-linear)

Unfortunately things are not always as easy as in the linear case and this definitely holds for elasticity problems. Although the general derivation follows the same route as in the linear case, the non-linear constitutive law makes the problem much more troublesome. Using the Neo-Hookean law we arrive at a system of non-linear equations of the form

$$\mathbf{H}(\mathbf{U}) = \mathbf{F}, \quad (4.28)$$

where \mathbf{F} is again an external force vector. However, \mathbf{H} is a non-linear operator and therefore we cannot simply use matrix manipulation to find \mathbf{U} . In addition to the non-linearity there is another complication in the case of hyperelasticity. Because the small strain assumption is not in general valid one has to take care over which body Ω the integration of \mathbf{H} and \mathbf{F} needs to be done. All preceding derivations of the integrals are over the current state which is in fact unknown. Of course it is possible to rewrite these integrals to get integrals over the reference state which we do know. However, in order to do so extra calculations are required, since inverse Jacobians of the transformation Φ are now needed as well.

4.1.4 Solving the non-linear FEM system

Whereas the solution to the linear model is quite 'straightforward' the method to solve the non-linear case requires some special attention. To solve equation (4.28) Newton-Raphson methods are often used. These methods try to find the roots of equations and therefore we rewrite our system such that the solution is a root of the system,

$$0 = \mathbf{G}(\mathbf{U}) = \mathbf{H}(\mathbf{U}) - \mathbf{F}. \quad (4.29)$$

Newton-Raphson starts with an initial guess \mathbf{U}^0 which does not need to be a solution. Then we perturb our guess to yield $\mathbf{U}^1 = \mathbf{U}^0 + \Delta\mathbf{U}$. Substituting this in our equation gives us the change to linearise the non-linear equations,

$$0 = \mathbf{G}(\mathbf{U}^1) \approx \mathbf{G}(\mathbf{U}^0) + \nabla\mathbf{G}(\mathbf{U}^0) \cdot \Delta\mathbf{U} = \mathbf{H}(\mathbf{U}^0) - \mathbf{F} + \nabla\mathbf{H}(\mathbf{U}^0) \cdot \Delta\mathbf{U}. \quad (4.30)$$

The result is a linear system of equations which we want to solve for $\Delta\mathbf{U}$,

$$\nabla\mathbf{H}(\mathbf{U}^0) \cdot \Delta\mathbf{U} = -\mathbf{H}(\mathbf{U}^0) + \mathbf{F}. \quad (4.31)$$

For hyperelastic materials this linearized system will bear resemblance to the linear FEM equations in the sense that it can be written as

$$\mathbf{K}' \cdot \Delta\mathbf{U} = \mathbf{F} - \mathbf{R}. \quad (4.32)$$

As a matter of fact \mathbf{K}' can be written in the form

$$\mathbf{K}' = \mathbf{K}_m + \mathbf{K}_g, \quad (4.33)$$

where \mathbf{K}_m is the material stiffness due to the constitutive law and thus similar to \mathbf{K} in the linear case. In addition to this there is an extra term \mathbf{K}_g which is due to the changes in geometry and are therefore a form of geometrical stiffening, a feature that cannot be captured by linear elasticity equations. After the system has been solved for $\Delta\mathbf{u}$ the displacement \mathbf{u}^1 can be constructed. To see whether this has converged towards the real solution we can probe the magnitude of \mathbf{G} or that of $\Delta\mathbf{u}$. If convergence has not yet been achieved the procedure can be started again, now with \mathbf{u}^1 as the starting guess. In this way the solution to the non-linear system of equations is stepwise approximated.

Numerical integration

In order to solve both the linear and the non-linear system of equations one needs to calculate a few volume and surface integrals before the unknowns can be solved from the system. These integrals are in practice approximated as well. This is mostly done by a method known as Gaussian quadrature[16], but this is outside the scope of this thesis.

4.1.5 Abaqus

In this project we use a commercial software package called Abaqus for numerical simulations. Abaqus is a so called Finite Element Analysis (FEA) software program. It can be used to model the object which must be simulated and to actually apply FEM to it, because it includes several mesh generation algorithms and FEM solving procedures. Furthermore it has a Graphical User Interface (GUI), but it can be controlled by use of Python scripts as well. The scripting control is most used in this project, mainly because of the possibility to perform parameter studies and reproducibility of the experiments.

4.2 Periodic boundary conditions

In order to simulate an infinite Holey Sheet without any edges periodic boundary conditions need to be imposed on the edges of the unit cell. That way we can periodically repeat the unit cell to get a periodic lattice of unit cells which is precisely an infinite Holey Sheet. The way this is done in Abaqus is by imposing constraints on the boundaries of the unit cell. Let a be the lattice size. Now we introduce two virtual points at position \mathbf{v}, \mathbf{w} originally placed in the origin $(0, 0)$. These virtual points are just for computational ease and do not represent any physical entities, but they are allowed to move as point particles without any interaction. Then we impose the following constraints, first on the left edge of the unit cell

$$\mathbf{u}(x, y) - \mathbf{u}(x + a, y) = \mathbf{v},$$

and on the bottom of the unit cell

$$\mathbf{u}(x, y) - \mathbf{u}(x, y + a) = \mathbf{w}.$$

If the virtual points stay in the origin this imposes the constraints that the movement of the left wall is equal to the movement of the right wall and the movement of the bottom is the same as that of the top. So why bother with these virtual points \mathbf{v}, \mathbf{w} ? If we want the edges of the unit cell to move relative to each other, which happens if for example one side is compressed, we can now implement this very by simply moving the virtual points. If we want to compress in the vertical direction all we have to do is move \mathbf{w} in the vertical direction, up for elongation and down for compression. Or we can track the relative motion of the edges by letting the virtual points move freely while compressing the unit cell, the position of the virtual points then reflects the boundary motion. Since the analysis is done on the mesh rather than on the original domain, these constraints have to be imposed on the mesh. This is done by imposing the same constraints on the nodes at the boundary of the unit cell. If the mesh is made symmetric then there is for each node on the side a node on the opposed edge. Therefore the constraints on the nodes coincide with the constraints which would be imposed on the original continuous domain and thus they are a discretization of the original constraints.

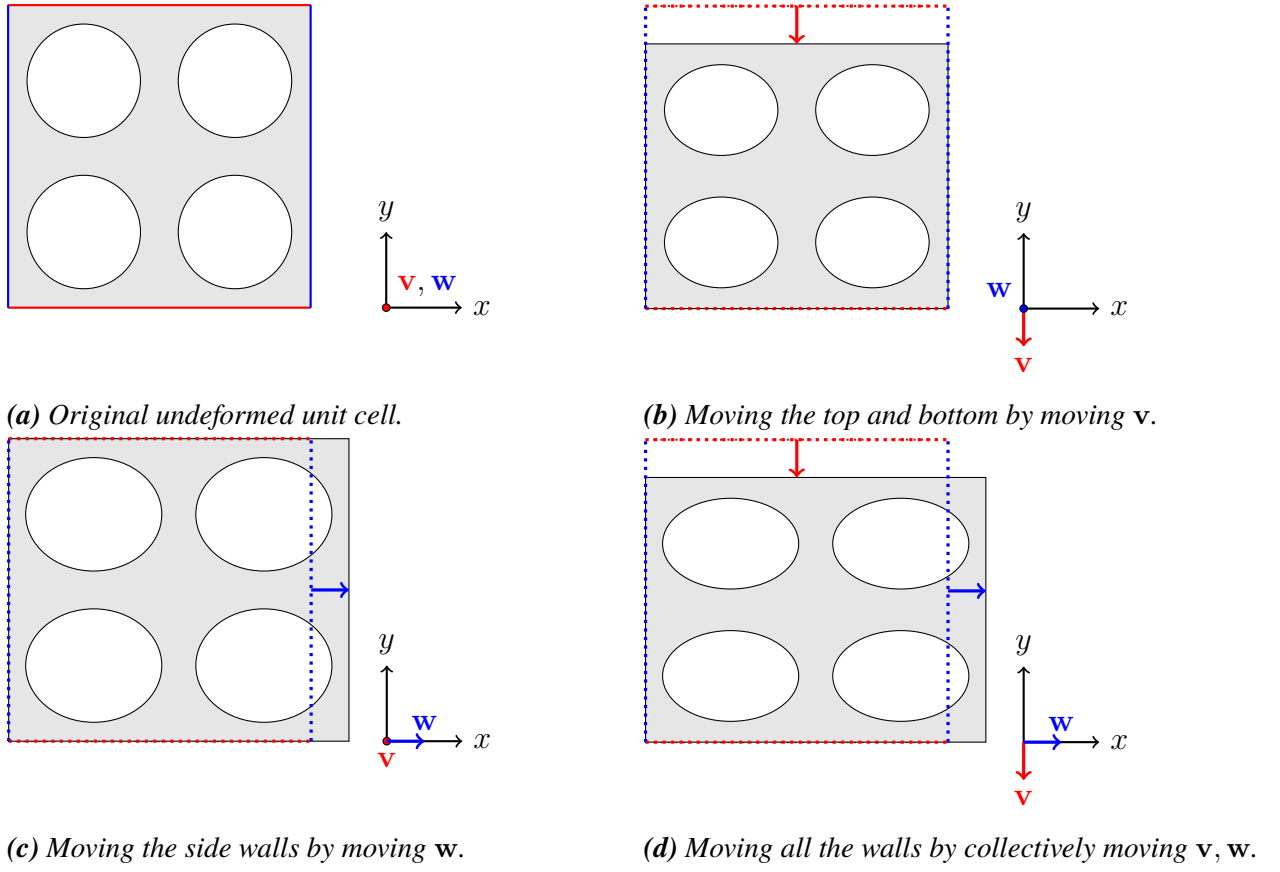


Figure 4.6: Effect of moving the virtual points at v and w as a compression on the unit cell.

4.3 Buckling analysis

We could already conclude that the way the unit cell reacts to compression can depend on the mesh (see figure 4.14). In particular it can influence whether and if so how the sheets buckle. When performing numerical simulations one would like to have a robust mechanism which does not depend on numerical parameters such as the mesh-size or type. Furthermore we would like to control the way the unit cell buckles, because it is this crucial aspect that we want to investigate. We know that the initial unbuckled configuration becomes unstable after the first buckling load has been applied, but this does not immediately mean that every numerical simulation of an unit cell will buckle in the first buckling-mode after this load has been applied. Laboratory experiments in contrast show that every Holey Sheet buckles in the first mode if compressed in one direction and therefore we are mostly interested in this first mode. It is thus needed to control the way the numerical simulation buckles. This can be done by slightly perturbing the system out of its symmetric state and thus lifting the degeneracy of the bifurcation point and unfolding the bifurcation.

4.3.1 Bifurcations and buckling

To introduce the concept of a bifurcation we look at a system of ordinary differential equations

$$\dot{\mathbf{y}} = \mathbf{P}(\mathbf{y}, \lambda). \quad (4.34)$$

One can look for the equilibrium solutions of this system of equations, which thus have to satisfy $\mathbf{P}(\mathbf{y}, \lambda) = 0$. When the parameter λ is varied, the equilibrium solution could change.

The curve(s) that it traces out is then called an equilibrium curve. Multiple equilibrium curves can exist, and therefore, it is possible that these curves intersect each other as well. Another possibility is two equilibrium curves colliding, but not necessarily intersecting. Exactly these intersection points or collision points of equilibrium curves are called the bifurcation points. It is in these points that multiple equilibrium solutions come together and form an equilibrium solution of higher multiplicity. The existence of bifurcation points is closely related to the Jacobian matrix of P and its eigenvalues and this will prove to be important in the numerical analysis later on.

Pitchfork bifurcation

There is an intimate link between buckling and bifurcations since the buckling of a bar is an example of one type of bifurcation, namely the pitchfork bifurcation. This type of bifurcation is closely linked to symmetry and more specific the breaking of symmetry, which we also see in the buckling of bars and the Holey Sheet. A (supercritical) pitchfork bifurcation starts with one equilibrium branch before the critical parameter λ_c has been reached. However, after the critical value of λ has been reached and λ is increased beyond this value, two new branches of equilibrium solutions emerge from the bifurcation point.

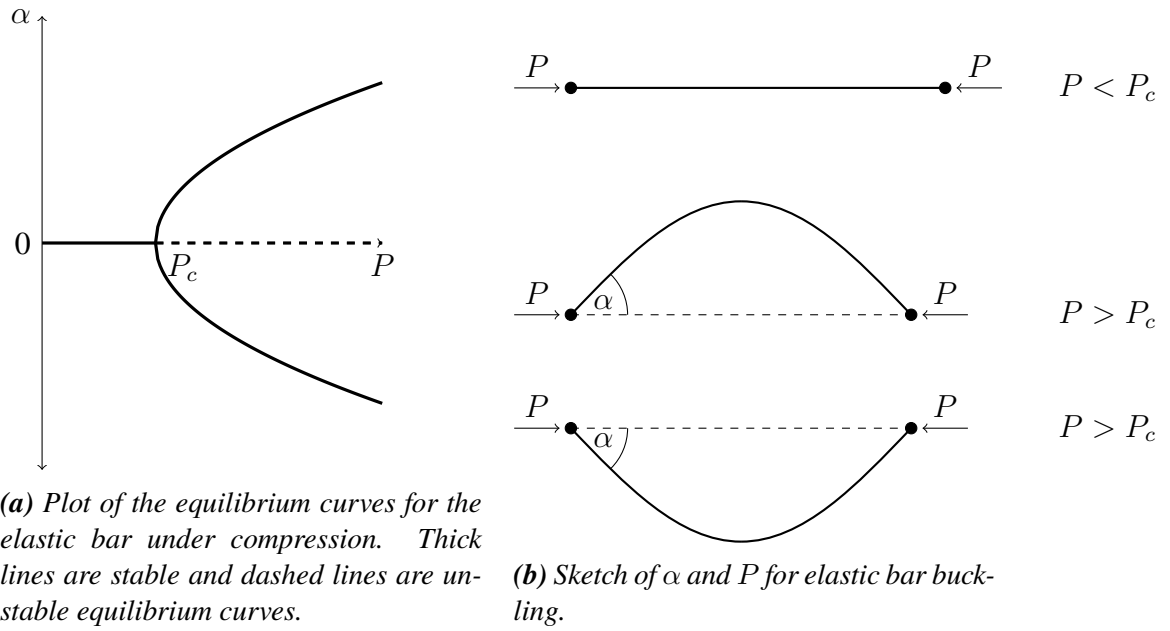


Figure 4.7: Buckling of an elastic bar described by the angle α with the original configuration at the left endpoint and the force P .

As an example we can look at a simple elastic beam. Although this system might seem unrelated to the Holey Sheet, it could in fact be of great importance, since a promising model of the Holey Sheet is that of a network of these simple beams joined together. Extensive research has been done to this situation, for example by Robbin Bastiaansen and Willem Schouten in their theses [18, 19]. Therefore we'll only briefly use this example to introduce some concepts. A sketch of the problem is given in figure 4.7. We compress a beam on both endpoints by a force P . When some critical load P_c has been passed the beam will buckle, and therefore, make an angle with the horizontal axis at the endpoints. This angle α therefore changes from a zero-value before P_c to a non-zero value after the critical load has been applied. This is represented in the bifurcation diagram which shows the angles α of the equilibria for a given

force P . The bifurcation diagram shows a reflection symmetry in the P -axis, which is very typical for the pitchfork bifurcation. The original system is symmetric under the reflection of the beam. However, after the bifurcation point has been passed, this symmetry is broken and now two non-trivial solutions appear which are each others mirrors. This is also what can be observed in the Holey Sheet. The presence of multiple solutions in one point, a degeneracy in some sense, makes it numerically troublesome to cross the bifurcation point. Therefore special attention is given to this in the next paragraphs.

Stability

For the pitchfork bifurcation of the elastic beam we start with the original undeformed beam. This is a stable configuration, in the sense that if we perturb our configuration slightly and then let it evolve, it will converge towards the original undeformed configuration, see figure 4.8. After the critical load has been reached and the load is increased further, we saw that two new branches emerged from the bifurcation point. The original branch now becomes unstable in contrast to the new branches which are stable. Unstable means that if we start close to a certain branch and we let the system evolve then it will move away from the equilibrium branch.

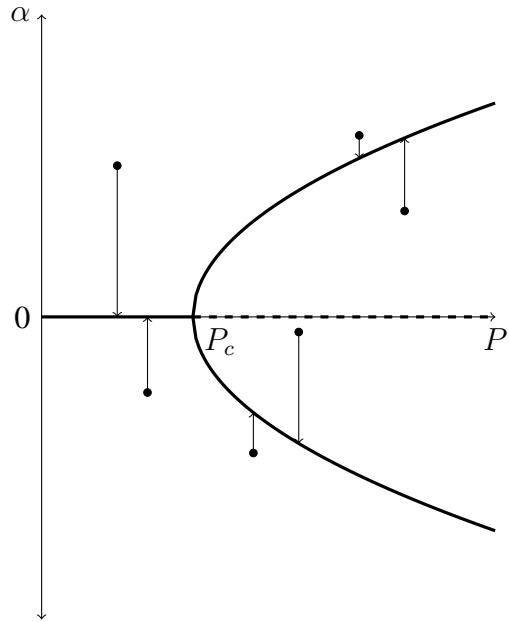


Figure 4.8: Stability of the multiple equilibrium branches. If a perturbation moves towards a branch, that branch is called stable. If it moves away from the branch, it is an unstable equilibrium.

Buckling modes

When compressing the beams beyond the critical load, they can attain different shapes due to the symmetry in the system. However, there are also other configurations possible which do not follow from a reflection. These other solutions are known as higher buckling modes. They do satisfy the same set of boundary conditions as the ones found in 4.7, but are very different, see figure 4.9. The critical point for which these higher modes can be attained is different for each of the higher mode and gets increasingly bigger with mode number increasing. The mode which is actually attained and observed is most of the times that specific mode which minimizes

the elastic energy, while satisfying all the boundary constraints.

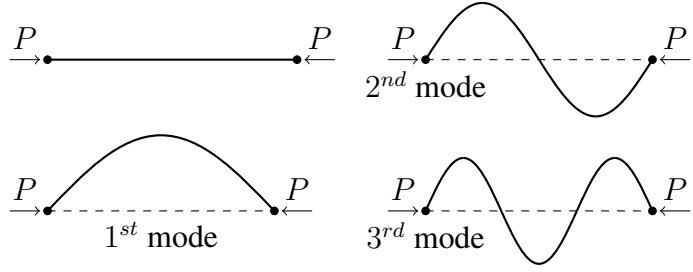


Figure 4.9: Different buckling modes for a single initially straight beam under uni-axial compression.

Just as the one-dimensional beam, the Holey Sheet has multiple buckling modes. These again have all different elastic energies and the one observed in the experiments thus has the least energy. In the numerical experiments however, other modes can be found and explored as well, as can be seen in figure 4.14, where 4.14e corresponds to the first buckling mode, which is the one observed in the laboratory experiments, and 4.14f to the first higher mode of the unit cell.

4.3.2 Linearised buckling analysis

A crude way to overcome the problems with the bifurcation point of the Holey Sheet is to first linearise the system of equations. As a result we throw away crucial information, but on the same time it allows us to actually calculate a linearised buckling load and the accompanying buckling mode which should be an approximation to the true buckling load and mode. So how does one calculate a buckling load from the FEM system of equations? The important thing to notice is that the system should become singular at the buckling point, since multiple solutions should emerge at the same time. Therefore we can try to find the point where our stiffness matrix \mathbf{K} becomes singular, i.e. it has an eigenvalue equal to zero. For this thesis two possible ways to calculate these eigenvalues have been used.

Abaqus buckling prediction

As mentioned before, the finite element system of equations needs to be linearised first. We start with a base state $\mathbf{U}^B, \mathbf{F}^B$ and then add a small perturbation $\Delta\mathbf{U}, \Delta\mathbf{F}^B$ to the base state. Then we linearise our system using the same procedure as the Newton-Raphson method, as was introduced in section 4.1.4. This yields a linear system of equations involving the Jacobian matrix. As noted before it is when this matrix becomes singular that the bifurcation point has been reached. Therefore we see that in our numerical analysis we are interested in the Jacobian matrix of the function $\mathbf{G}(\mathbf{U})$ as in section 4.1.4. The method starts with the equation

$$(\mathbf{K}_m + \mathbf{K}_g)\Delta\mathbf{U} = 0. \quad (4.35)$$

In calculating these two matrices [20] one finds that \mathbf{K}_m only depends on \mathbf{U}^B whereas \mathbf{K}_g by assumption of the linear perturbation depends linearly on $\Delta\mathbf{U}$. Therefore we could as well add a perturbation $\lambda\Delta\mathbf{U}$, which then yields the system

$$(\mathbf{K}_m + \lambda\mathbf{K}_g)\Delta\mathbf{U} = 0. \quad (4.36)$$

The question then is for what value λ a non-trivial $\Delta\mathbf{U}$ (which is prescribed) can be found as a solution to this system. Abaqus determines this value by regarding this as a generalized

eigenvalue problem and solving it for the eigenvalue λ . With this value a new prediction for the buckling displacement, $\mathbf{U} = \mathbf{U}^B + \lambda \Delta \mathbf{U}$, can be constructed.

Abaqus frequency calculation

For this method not the equilibrium equation, but the full dynamical elastic equation (3.20) is used and converted into finite element equations. The extra term concerning time derivatives of \mathbf{u} adds an extra term

$$\mathbf{M}\ddot{\mathbf{U}} + \mathbf{K}\mathbf{U} = \mathbf{F}, \quad (4.37)$$

where \mathbf{M} is called the mass matrix, which stems from the integral involving $\rho(\mathbf{x}, t)$. The frequency calculation then searches for a non-trivial eigensolution of the unforced problem, so with $\mathbf{F} = \mathbf{0}$. It assumes a solution of the form $\mathbf{U}(t) = e^{\lambda t} \bar{\mathbf{U}}$, where λ is called the natural frequency of the mode $\bar{\mathbf{U}}$. This changes the equations to

$$\mathbf{0} = \lambda^2 \mathbf{M} \bar{\mathbf{U}} + \mathbf{K} \bar{\mathbf{U}} = (\lambda^2 \mathbf{M} + \mathbf{K}) \bar{\mathbf{U}}. \quad (4.38)$$

Which is a generalized eigenvalue problem for λ . We are interested in the $\bar{\mathbf{U}}$ such that $\lambda = 0$ because than we would have that $\mathbf{K} \bar{\mathbf{U}} = \mathbf{0}$ and therefore we would have arrived at the buckling point since we have a non-trivial solution which satisfies the equilibrium equations. The advantage of this method is that it provides a good measure of the nearness of the buckling point, since we can just see how much the smallest λ deviates from zero. However, it doesn't provide us a critical force or critical displacement, which we are after. Therefore this method needs to be accompanied by a method to calculate \mathbf{u}_c from λ . But just as the buckling prediction in Abaqus does, this method produces a deformed mesh ($\bar{\mathbf{u}}$) which bears resemblance to the buckle modes. This will turn out to be useful to cross the buckling point as we'll see soon.

Crossing the buckling point: break the symmetry

Having found a (rough) approximation to the critical point still leaves us with the problem of how to switch branches at the critical point. If we just compress the original configuration it will start at the stable branch, but it won't generally depart from it at the buckling point. There is no reason for it to do so since symmetry prevents it from choosing one of the two possible new non-trivial stable branches and therefore it continues to move on the unstable branch. Numerical simulations on unstable branches are hard since the matrix \mathbf{K} is not positive-definite any more, a feature that is used in most solution methods and therefore the simulations often are starting to have trouble converging beyond the critical point on the unstable branch.

One simple way to solve this problem is by breaking the symmetry that is preventing the sheet from buckling and therefore forcing it to buckle. This can be done by adding the approximated first buckling mode as computed by one of the two aforementioned methods as an perturbation to our original problem. Now (part) of the geometrical symmetry has been broken and we can then perform the compression experiment. This procedure of adding some perturbation to the original mesh is called seeding the mesh in the case of FEM. In a more general sense this procedure of unfolding a pitchfork bifurcation by breaking the symmetry is called the addition of imperfection to the system to get an imperfect pitchfork bifurcation.

In the case of the elastic beam we could apply an initial torque at the endpoints to break the symmetry. Therefore the initial stable solution has an angle α which is non-zero and it will buckle without any problem if the force is increased since it simply follows the stable branch which doesn't come across a problematic point such as a buckling point, see figure 4.10. The reason why this method is crude is that it immediately breaks the symmetry of the system and

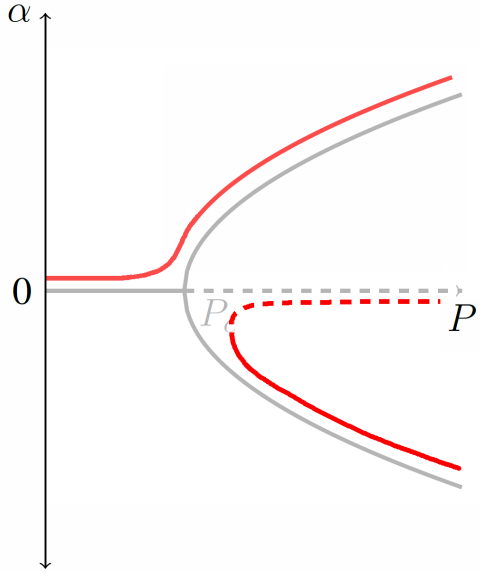


Figure 4.10: Imperfect bifurcation diagram of the elastic beam where symmetry has been broken. The branches of equilibrium solutions have been disconnected to form two disjoint sets.

thus unfolds the bifurcation point. Therefore our curves get rounded off around the bifurcation point and can not get to the actual bifurcation point itself, we only get smooth curves around it. We introduce an error due to the imperfection and if we want to carefully study our system we need to perform an error-study every time we use this method. Since we want to perform a large batch of numerical simulations exploring the parameter space of the hole size, this method will become very time-consuming. A reason to still implement this method is that it is fast, since the procedure is fairly easy and only one step of linearisation needs to be done. Furthermore it is robust since we force the initial geometry to break into the first buckling mode. It can therefore serve as a first approximation and method to quickly check the properties of the simulation, but is not very suited for close study of the behaviour around the buckling point.

4.3.3 Non-linear buckling analysis

One of the major drawbacks of the imperfection methods just prescribed is that it immediately destroys the symmetry of the system and thus makes it impossible to closely study the bifurcation point. Furthermore an error analysis is needed to check whether we have approximated our original curves sufficiently. One way to overcome this is to use non-linear buckling analysis. This procedure converges towards the bifurcation point via successive application of the linearised buckling analysis. The calculated bifurcation point by the linear buckling analysis will not be the correct value, because the real response of the Holey Sheet will slightly differ from a perfect linear Hookean material as the geometry changes slightly. Therefore we can go to the calculated buckling point and then start the linear buckling analysis again. The big difference this time being that the geometry now has changed and the new reference state is the old current state. Therefore in each iteration the matrices involved change. This makes the method of course computationally more costly. The advantage on the other hand is that it provides a much more accurate result and therefore we can get very close to the real buckling point, the relative order being of the order 10^{-6} for most geometries. We track λ during our calculations, whether we use frequency extraction or buckling prediction, to see if we converge towards the critical point. As a stopping criterion is chosen that as soon as $|\lambda| < \epsilon$, for some small ϵ , the iteration is

stopped. Furthermore we use a very naive line-search method in order to prevent that we cross the bifurcation point, since calculations are hard if the buckling point has been exceeded. The problem with computations after the bifurcation point has been crossed, is that the matrix K fails being positive definite, a property heavily used in the computational schemes.

If $\Delta\mathbf{u}$ is the correction to the i -th iteration compression \mathbf{u}_i then we construct the $i+1$ -th iteration as

$$\mathbf{u}_{i+1} = \mathbf{u}_i + \alpha \Delta\mathbf{u}, \quad (4.39)$$

where α is the line search parameter. This method can also be viewed as a successive over-relaxation method for an iterative method. The method is naive in the sense that we only check if $0 < \lambda_{i+1} < \lambda_i$ and if this is not the case we halve α , thus $\alpha \rightarrow \frac{\alpha^*}{2}$. The first inequality makes sure that we stay under the critical displacement. The second inequality is used to make sure that we converge towards the critical point, if the increments get bigger in each iteration then that means that one is moving away from the buckling point in general. The result of this method is a much more accurate prediction of the critical displacement.

Crossing the buckling point

Although our prediction of the critical point is much better in the non-linear case we still need to find a way to cross the buckling point, because symmetry still prevents buckling. The strategy we follow encloses on the bifurcation point and then slightly tweaks the system out of its symmetric configuration by applying some tiny force or rotation constraint. Then we compress slightly beyond the bifurcation point and let loose the earlier applied constraint. In this way the system evolves back to one of the two stable non-trivial equilibrium branches which we can now simply follow, see figure 4.11. By using this method we can get very close to the buckling point and still follow the equilibrium branches we want to investigate.

4.4 Influence of the mesh

4.4.1 Mesh density

A crucial part of the FEM is the choice of the mesh used to discretize the geometry. As mentioned before, Abaqus has some built-in mesh generators which automatically provide a suitable mesh based on a few input parameters. The parameters which we controlled in Abaqus to create our mesh are the size of the mesh elements, a deviation factor for the deviation of the prescribed size and the element type which we use to mesh the geometry. All the parameters are of crucial importance in the set-up of the analysis. Taking a too coarse grid may result in large numerical inaccuracies, because not enough information is taken into account during the computations, and thus convergence can be lacking. Furthermore, crucial parts of the geometry can be missed if a too coarse mesh is chosen. This is especially crucial in the simulation of Holey Sheets since circles need to be approximated by elements with straight edges. As a result there is inherently a little loss of geometry and we want to keep this as small as possible, see figure 4.12. On the other hand taking a too fine mesh results in an enormous system of equations since we need to solve equations on every element. A finer mesh will thus result in a larger runtime. For these reasons a short study on the influence of the mesh density is needed in order to see whether the results depend on the mesh density or not. After this study we are ideally able to choose an

*There might be more clever ways to improve convergence by choosing α based on an energy method, i.e. choose α such as to minimize a certain elastic energy. However this was not necessary for this thesis.

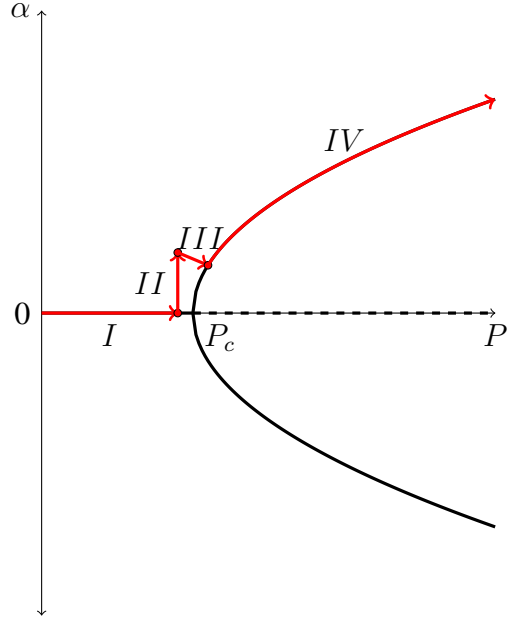


Figure 4.11: Illustration of the non-linear buckling analysis steps. Step I: closing in on the buckling point. Step II: tweaking the system by some constraint out of symmetry. Step III: crossing the buckling point whilst releasing the constraint. Step IV: continuing along the stable buckled branch.

optimal mesh density which is both coarse enough to be fast and fine enough to be accurate.

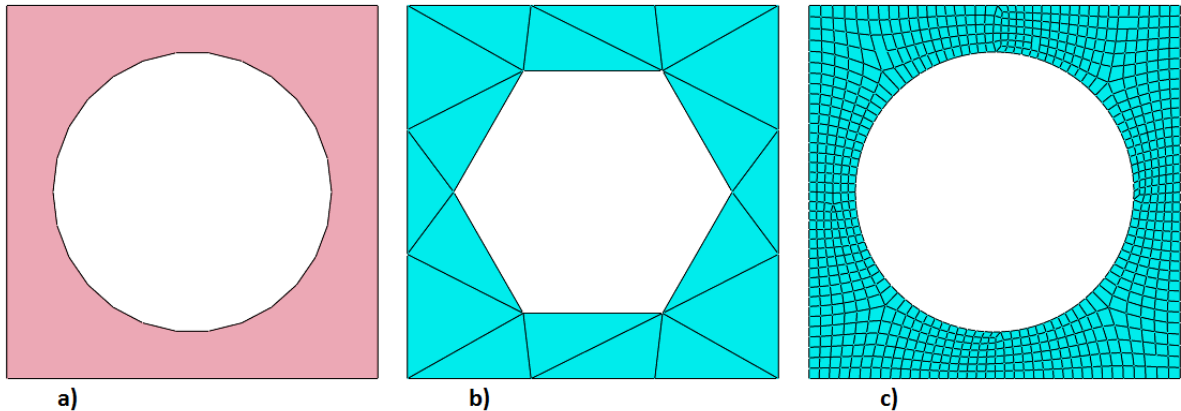


Figure 4.12: Effects of meshing on a building block of the Holey Sheet. It can be seen that the geometry of the mesh can substantially differ from the original geometry if parameters aren't chosen wisely. **a):** Original geometry. **b):** Too coarse mesh. **c):** Finer mesh.

4.4.2 Symmetry considerations

When doing analysis on bifurcations of systems with a lot of symmetries we are very sensitive to a disturbance of this symmetry as it can unfold the bifurcation and therefore make study of the bifurcation point troublesome. Therefore it might be advantageous to have a mesh which

preserves the symmetry of the original geometry. However, the standard algorithms in Abaqus cannot do this, so some adaptations have to be made. One way of getting more control over the meshing of the unit cell is to partition the unit cell manually before the mesh is made. Abaqus will then mesh this subdomains separately. If this subdividing is done in such a way that the original symmetry is preserved, the mesh will hopefully be more symmetric. This assumes that if Abaqus needs to mesh partitions which are equal up to translation and or rotations then the meshing is done in exactly the same way[†]. The next chapter explores in some more depth the symmetries of the Holey Sheet, but for now it is sufficient to state that in order to preserve the original symmetries of the unit cell we need to partition our geometry according to the reflection and translation axis. If we furthermore want to preserve the translational symmetry of the Holey Sheet so that we are able to shift each circle one separation distance up, down or to the left or right, then we should look even smaller at the primitive cell of the Holey Sheet, consisting of only one circular hole in a square. This smallest building block has the same symmetries as the unit cell. If we partition now along the reflection axis of the primitive cell, see figure 4.13, and then let Abaqus mesh these partitions with a suitable meshing technique we will end up with a mesh which is not only periodic but also preserves the symmetries.

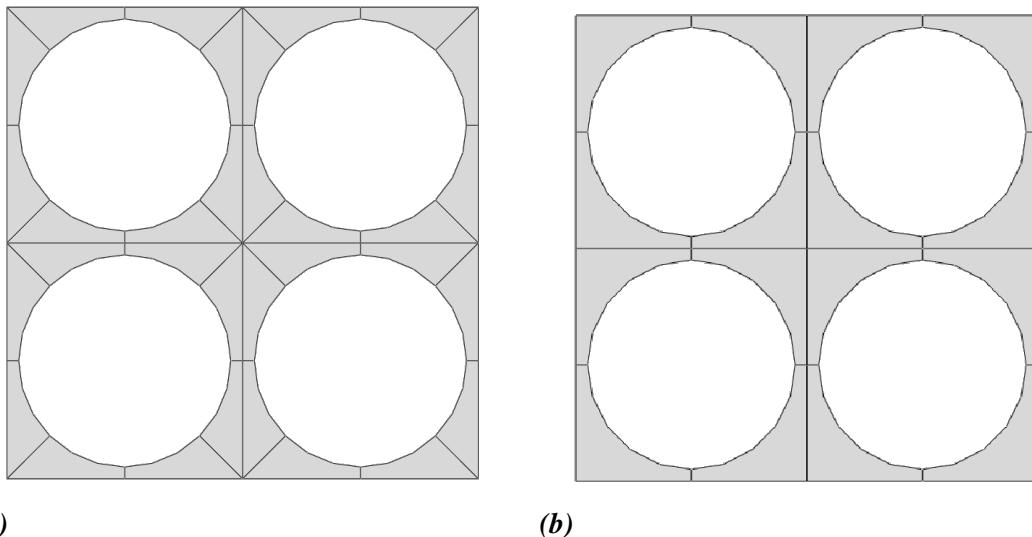


Figure 4.13: Different partitions of the unit cell into smaller equal subdomains. 4.13a Partition taking into account the $p4m$ symmetry (see chapter 2) of the primitive cell. 4.13b: Partition according to the symmetries of the unit cell not incorporating reflections along the diagonals of the primitive cell reflects the pmm symmetry of the pre-buckled Holey Sheet under uni-axial compression.

Meshing algorithms

Examples of such suitable meshing techniques are the Sweep and Structured meshing techniques. A swept mesh is a technique where Abaqus defines elements on one edge of the partition and then copies these elements one element layer at a time to the opposing edge of the element. This has the nice feature that when applied to the primitive cell it will concentrate

[†]This is a safe assumption since most mesh algorithms in Abaqus use mappings of the partitions to a standard geometry on which they create a mesh. This mesh on the standard geometry is then mapped back onto the original geometry.

more elements in the thin regions than in the island regions. This is advantageous because the buckling occurs at the thin parts and therefore the largest variations in strain and stresses are in these thin regions. The result of the meshing technique is that more and smaller elements are concentrated at the regions of large displacement. The structured meshing technique maps a simple mesh on a rectangle onto the partitioned parts.

Effects on simulation

A nice illustration of why this symmetry is indeed important can be seen in figure 4.14. Depending on the type of the mesh and the way it preserves the symmetries, the unit cell will buckle in different modes, which dramatically influences the simulations. All cases represent the result of

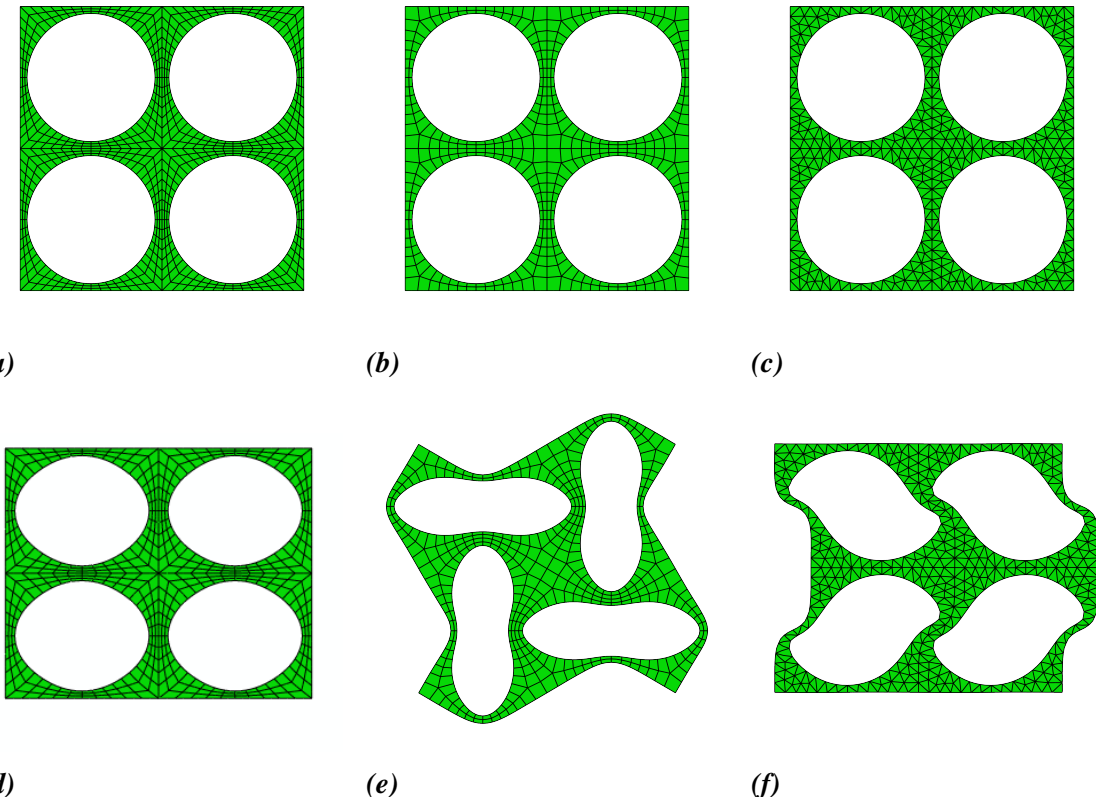


Figure 4.14: Effect of different meshing techniques and partitioning on simulations. Depending on the mesh a different buckling mode is found under uni-axial compression. All filament thickness $t = 0.1$.

4.14a,4.14d: Meshed using the swept mesh algorithm and the partition from 4.13a.

4.14b,4.14e: Meshed by Medial Axis algorithm and the partition from 4.13b.

4.14c,4.14f: Free meshing algorithm with triangular elements and the partition from 4.13b.

an uni-axial compression of an unit cell of the Holey Sheet (the amount of compression is the same in all cases). The only differences between the cases are the element type that is used and the partitions that are made before the mesh is generated. Figures 4.14a,4.14d are partitioned as in figure 4.13a. Therefore the uncompressed mesh has the same symmetry group as the original domain, p4m. In contrast, figures 4.14b,4.14e are partitioned according to figure 4.13b, so the reflection symmetries at the diagonals of the primitive cell are not incorporated in this mesh. Both figures 4.14a and 4.14b are meshed by using quadrilateral elements. The technique used

the aforementioned sweep meshing technique. The algorithm used to mesh figure 4.14b is the Medial Axis algorithm, which partitions the original geometry in smaller parts divided by the medial axis of the structure and creates the mesh on this subdomains. The medial axis is the set of all points in the structure which have more than one point on the edge which they are closest to. The mesh is therefore more structured than the rightmost example, figure 4.14c. This object is meshed by using triangular elements and the mesh is constructed in a 'free' way, which simply says that apart from partitions of the original geometry the algorithm does not create any other extra partitions to exploit the geometrical structure.

The fact that the 4.14d does not show any buckling should not come as a surprise, since the situation is completely symmetric along the central vertical axis. In order to buckle this symmetry must be spontaneously broken, but the force is symmetric along the same axis as well and thus does not break the symmetry. As a result the unit cell will stay in the unbuckled ground mode, although this may not be the state of the minimum energy and a small perturbation of the system will kick it out of this unstable configuration into one of the stable buckling modes if enough load is applied.

This page would be intentionally left blank if we would not wish to inform about that.

Results

This chapter is devoted to the analysis of the numerical results on the Holey Sheet obtained with the finite element method. Of special interest in this analysis is the comparison of the numerical results of the Holey Sheet to the mechanical behaviour of ordinary beams. In this way we hope to capture the mechanics of the Holey Sheet in a simpler model of which results are already known, namely simple one or two dimensional beams under compression.

The material properties such as density and elastic moduli of the Holey Sheet do not vary in the simulations, it is the geometry which we can change. This is accomplished by tuning geometrical parameters, in our case the size of the holes in the unit cell, or equivalently the filament thickness parameter t as depicted in figure 5.4. The subsequent mechanical response as a function of t is the main subject of interest in this thesis.

5.1 Force-displacement curves

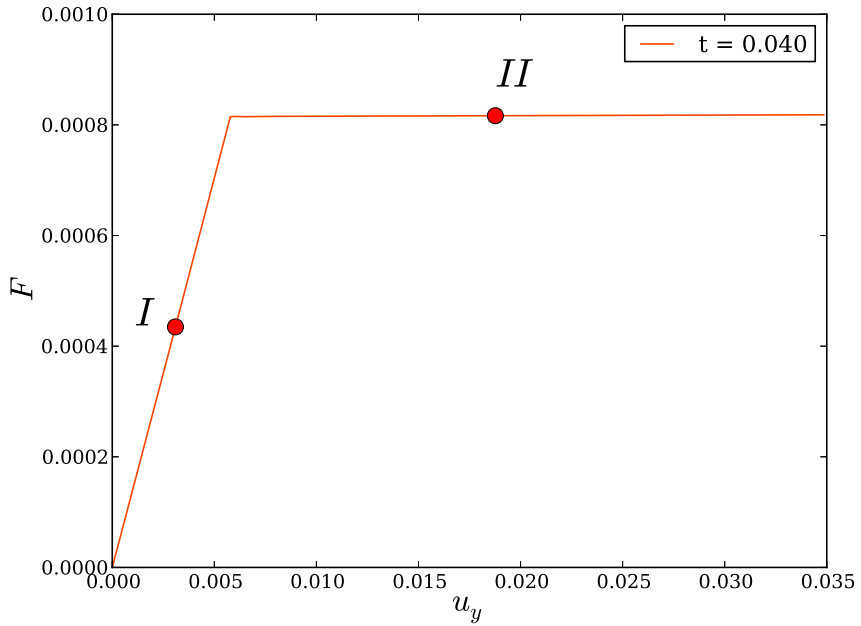
The results of the experiments on the Holey Sheet can be graphically presented by a force-displacement curve, representing the force resulting from a given displacement or vice versa, just as we saw in the introduction, figure 1.3. In the numerical simulations we impose a certain displacement on the edges of the Holey Sheet and extract the resultant force from the data. Typical examples of these curves and the corresponding geometries are given in figures 5.1 and 5.2.

It is the exact form of the force displacement curves which is the subject of study in this thesis. We see that a peak is formed in 5.2, but not in 5.1. Therefore it is expected that in the parameter space of t there is transition between behaviour with and without a peak.

As we can observe there are two distinct phases corresponding to different geometries as well. This, of course, has everything to do with the buckling instability of the Holey Sheet. The transition point of these phases is exactly the buckling point of the sheet. At the transition point the symmetry of the system breaks abruptly and this dramatically changes the mechanical response of the material.

There is a clear distinction between the two phases, namely the displacements taking place. In the pre-buckling phase only small displacements take place, as the material responds linear to the compression. In contrast, in the post-buckling phase, large deformations can be observed due to the extensive bending of the filaments. The two phases are thus very different and will be treated separately, because different methods are needed for each one.

The observed behaviour is not unique for the Holey Sheet, similar responses can be found in (thick) beams as well. This prototype model also exhibits buckling and different pre- and post-



(a) *Undeformed unit cell.*

(b) *I: Pre-buckling.*

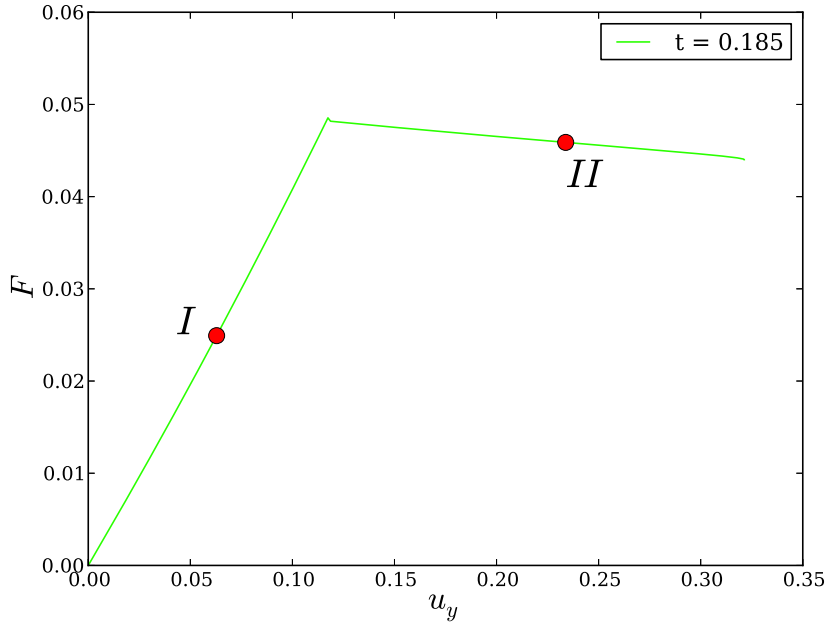
(c) *II: Post-buckling.*

Figure 5.1: Force-displacement curve of numerical simulation of uni-axial compression of the unit cell with $t = 0.04$. The stills correspond to the indicated points on the graph. The colors on the unit cell represent the Von Misses stress, a scalar measure for the total amount of stress σ at a point. The color ranges from blue, for low Von Misses stress, via green, to red, for high values.

buckling behaviour. If one compares the force curves of the Holey Sheet to that of certain beams, see figure 5.3, one sees that their behaviour looks very similar. This motivates the question whether it is possible to model the Holey Sheet as a beam which has exactly the same mechanical response, but has a simpler geometry and is easier to understand.

5.2 Mapping the Holey Sheet to a beam

In addition to the resemblance in the force curves in the preceding section, another motivation can be provided for the study of the Holey Sheet as a beam, which we will call the effective beam. This effective beam will be a modelled beam which reacts identical to the Holey Sheet upon compression. The link between these two systems can be motivated from the pre-buckle phase, where the compression of the Holey Sheet seems to boil down to the compression of the



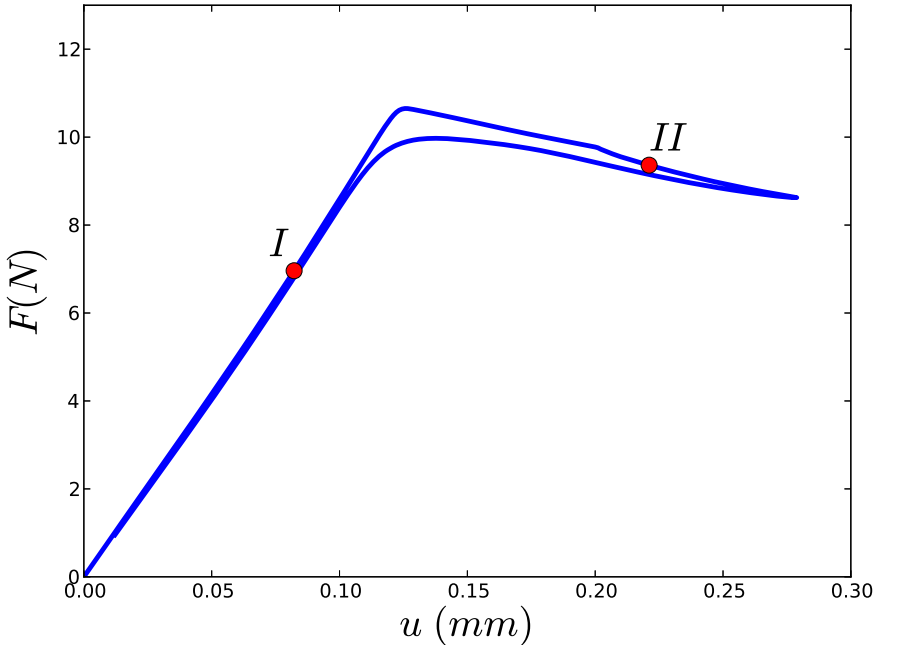
(a) Undeformed unit cell. (b) I: Pre-buckling. (c) II: Post-buckling.

Figure 5.2: Force-displacement curve of numerical simulation of uni-axial compression of the unit cell with $t = 0.185$. The stills correspond to the indicated points on the graph. The color ranges from blue, for low Von Misses stress, via green, to red, for high values.

filaments aligned with the external forcing. These filaments are expected to behave as beams and can thus be modelled by the compression of a simple two-dimensional effective beam of length L and width A for which results are known. It is interesting as well to see whether this effective beam theory still holds in the post-buckling phase which we investigated in this thesis as well. Therefore, the overall goal of this investigation is to see whether an effective length $L^*(t)$ can be found such that the behaviour of a Holey Sheet, with filament thickness t , coincides with that of a beam of length $L^*(t)$ and uniform width t under the same compression, see figure 5.4. In this way we can define an effective beam which exhibits the same mechanics as the Holey Sheet, but is easier to understand and therefore hopefully sheds some light on the underlying theory of the mechanical behaviour of the more complex Holey Sheet.

5.2.1 Theoretical predictions on non-uniform beams

Following the analysis of Day et al.[21] we can derive a theoretical prediction for the dependency of the effective length on the thickness. First, we need to know the results for the uni-axial



(a) Undeformed beam. (b) I: Pre-buckling. (c) II: Post-buckling.

Figure 5.3: Force-displacement curve of the compression of a beam with a length of 45 mm, a depth of 35 mm and a width of 8.30mm. The stills correspond to the indicated points on the graph.

The two different curves originate from the fact that the experiment compresses the sample and then returns progressively to the original uncompressed state. The return is observed to be slightly different from the compression.

compression of an uniform bar of length L and width A by a force F , see figure 5.5. In the beginning we are interested in the pre-buckling phase, and therefore, can assume small displacements and strains. As a result we are allowed to use the linear Hookean law to describe the relation between stress and strain. Furthermore, small displacements justify the use of the engineering strain expression.

Under the assumption that the stresses are zero in every other direction than that of the applied force, the stress strain relation in the direction where the force is applied reads [8]

$$\sigma_{xx} = E \varepsilon_{xx}. \quad (5.1)$$

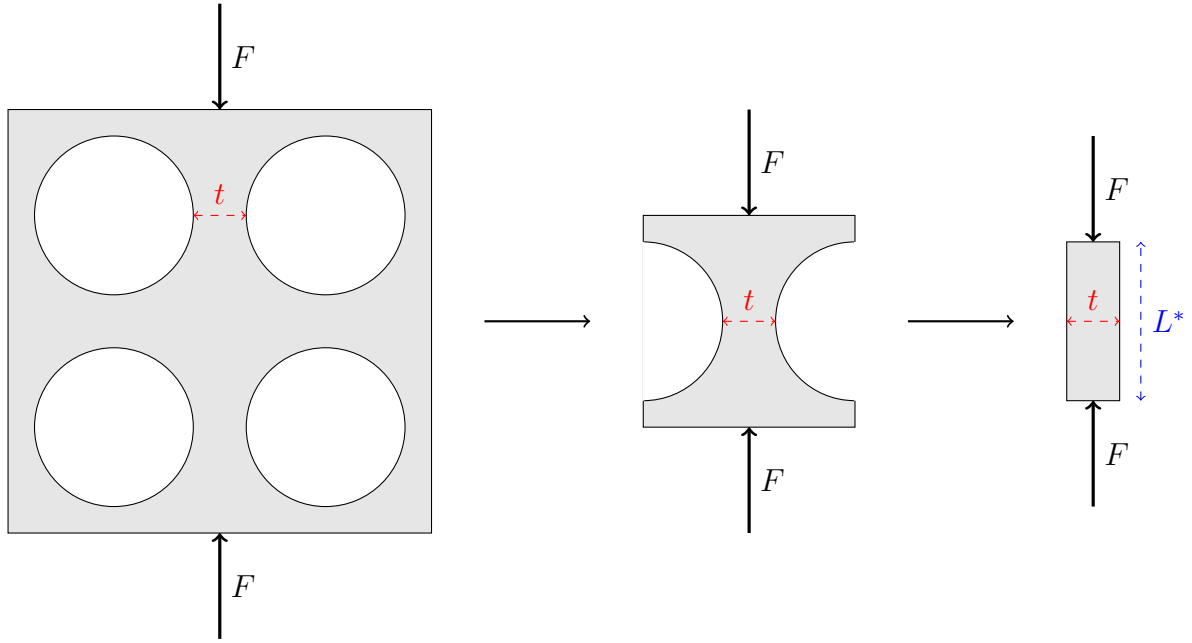


Figure 5.4: Different modelling phases: Before buckling of the sheet the compression can be regarded as a compression of the vertical filaments only. This simplification is shown in the first step. We then study whether this compression can be modelled by a simple uniform beam as shown on the right.

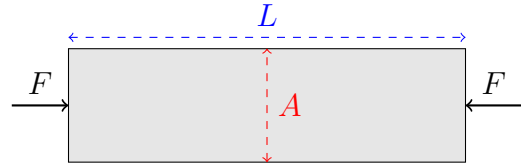


Figure 5.5: Compression of an uniform beam of width A and length L by a force F .

If we assume that σ is constant over the surface and plug it in equation (3.11), we can relate the stress to the force by

$$F = \sigma_{xx}A \quad (5.2)$$

Furthermore the strain is related to the displacement u by

$$\varepsilon_{xx} = \frac{u}{L}. \quad (5.3)$$

After combining these expressions we arrive at a relation between F and u for beam compression,

$$F = \frac{EA}{L}u = ku, \quad (5.4)$$

where k is called the stiffness of the beam. Upon taking a non-uniform beam, such as our vertical filaments, we need to adapt equation (5.4).

In order to do so, we begin with a local expression for the relation between F and u ,

$$F = EA(x) \frac{\Delta u(x)}{\Delta x}, \quad (5.5)$$

where x is some variable describing the position on the beam. This can be rewritten to

$$\Delta u(x) = \frac{F}{EA(x)}\Delta x. \quad (5.6)$$

In order to find a global relation between F and u we integrate (5.6) (take Δx infinitesimal small), because u is simply the integral over the beam length of $\Delta u(x)$,

$$u = \int \frac{F}{EA(x)} dx = \frac{F}{E} \int \frac{1}{A(x)} dx. \quad (5.7)$$

Under the assumption that F does not vary with position and that the material is homogeneous (E is a constant), we can now see that the only term remaining under the integral sign is a geometrical term $A(x)$ depicting the local width to which the force is applied. This width $A(x)$ will therefore depend on t in the case of the Holey Sheet and we thus write $A(x, t)$. To determine the integral for the specific filaments we make $A(x)$ explicit as a function of the thickness t , see figure 5.6,

$$A(x, t) = t + 2R(1 - \cos \phi). \quad (5.8)$$

If we look at figure 5.1c, we see that the regions of interesting behaviour of the Holey Sheet

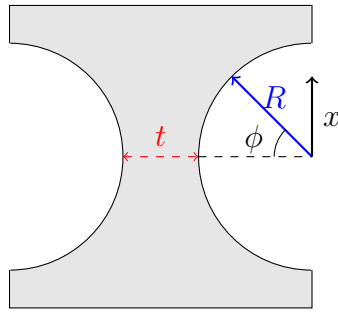


Figure 5.6: Sketch of the geometry in the derivation of the effective beam length of a thin filament following Day et al.[21].

seem to be really concentrated at the thin parts of the filaments. Those are the regions where the internal stresses seem to be concentrated. Therefore it might be a good assumption to assume that most of the strains and stresses are concentrated at the thinnest regions, i.e. where $\phi \approx 0$. So suppose we are primarily interested in the behaviour of $A(x, t)$ for small ϕ . Then we expand the cosine into its Taylor series and truncate it after the second order term,

$$A(x, t) \approx t + 2R \frac{\phi^2}{2}. \quad (5.9)$$

Assuming a small angle ϕ one can derive the expression $\phi \approx \sin \phi = \frac{x}{R}$. When we combine these two approximations we arrive at

$$A(x, t) \approx t + \frac{x^2}{R}. \quad (5.10)$$

Since the strains are localized in the thin parts of the filaments only it is expected that the contributions from areas away from the center of the filaments are negligible. As a result we change our limits of integration and integrate x from $-\infty$ to ∞ ,

$$u = \frac{F}{E} \int_{-\infty}^{\infty} \frac{1}{t + \frac{x^2}{R}} dx = \frac{\pi F}{E} \sqrt{\frac{R}{t}} = \frac{\pi F}{E} \sqrt{\frac{1-t}{2t}}. \quad (5.11)$$

This can be rewritten in a more familiar form using the stiffness k ,

$$F = k(t)u, \quad (5.12)$$

where we now have a stiffness depending on t ,

$$k(t) = \frac{E}{\pi} \sqrt{\frac{2t}{1-t}}. \quad (5.13)$$

Bi-axial compression

The above analysis will not be valid for the bi-axial compression case. For this setting we use a more appropriate elastic modulus, namely the bulk modulus B . This modulus relates the stress to the strain in the case of a uniform isotropic compression of a material, which for 2D is exactly equal to bi-axial compression. We have in both the x and y -direction

$$\sigma = 2B\varepsilon. \quad (5.14)$$

In the case of plain strain the bulk modulus is related to the Young's modulus E and Poisson's ratio ν of the material as we saw in (3.43)

$$B = \frac{E}{2(1-\nu)}. \quad (5.15)$$

Therefore our aforementioned expressions for the uni-axial case change by a factor of $(1-\nu)$,

$$F = (1-\nu) \frac{EA}{L} u = (1-\nu) k u. \quad (5.16)$$

Which transforms in the case of non-uniform beams to

$$F = (1-\nu) k(t) u. \quad (5.17)$$

5.3 Pre-buckling phase: small deformations

The first stage of the compression of beams and the Holey Sheet will not induce large displacements and strains. Therefore, we can use the infinitesimal strain theory and linear constitutive laws. In order to arrive at an effective length, two methods are proposed. The first one relates the stiffness of the Holey Sheet as measured to an effective length and therefore is only related to the behaviour of the sheet before buckling has occurred. The second method uses information on the buckling point itself to define an effective length and therefore can result in different estimates.

5.3.1 Method I: Pre-buckling stiffness

If we want to model the pre-buckling phase for uni-axial compression as the compression of an uniform beam we use expression (5.12). We assume for our effective beam that it has constant width $A(t) = t$. The effective length L^* is then found by using the relation between stiffness k and length L ,

$$L^* = \frac{EA(t)}{k(t)} = \frac{Et}{k(t)}. \quad (5.18)$$

Since the stiffness $k(t)$ can be extracted from the simulations this provides a direct way of calculating L^* . The theoretical prediction by Day et al. then yields that

$$L^* = \frac{\pi}{\sqrt{2}} \sqrt{t(1-t)}. \quad (5.19)$$

As a result of the difference between uni-axial and bi-axial compression, the expressions for the effective length have to be adjusted for the bi-axial case,

$$L_{bi}^* = (1 - \nu)L_{uni}^*. \quad (5.20)$$

The only problem now is that ν is not known as a function of t . But in the simulations it can be calculated of course by simply using the definition of ν (1.1). This calculated ν can then be used to rescale L_{uni}^* onto L_{bi}^* .

Discrepancy between simulation and prediction

As we can see from figure 5.7 the predictions of Day et al.[21] are not sufficient to predict the simulations correctly. Only for $t < 0.01$ it seems that there is agreement. For larger t the predictions fail in both the uni-axial and the bi-axial case as it rises far too quickly. This might be due to the fact that the approximation made in the derivation of L^* is simply too crude. If the filaments get thicker the strains might be not only localized at the center of the filaments and therefore contributions outside the center of the filaments need to be considered. For the really thin filaments it seems that the approximation holds and that our assumption that the stresses and strains are localized in the center thus seems to be valid.

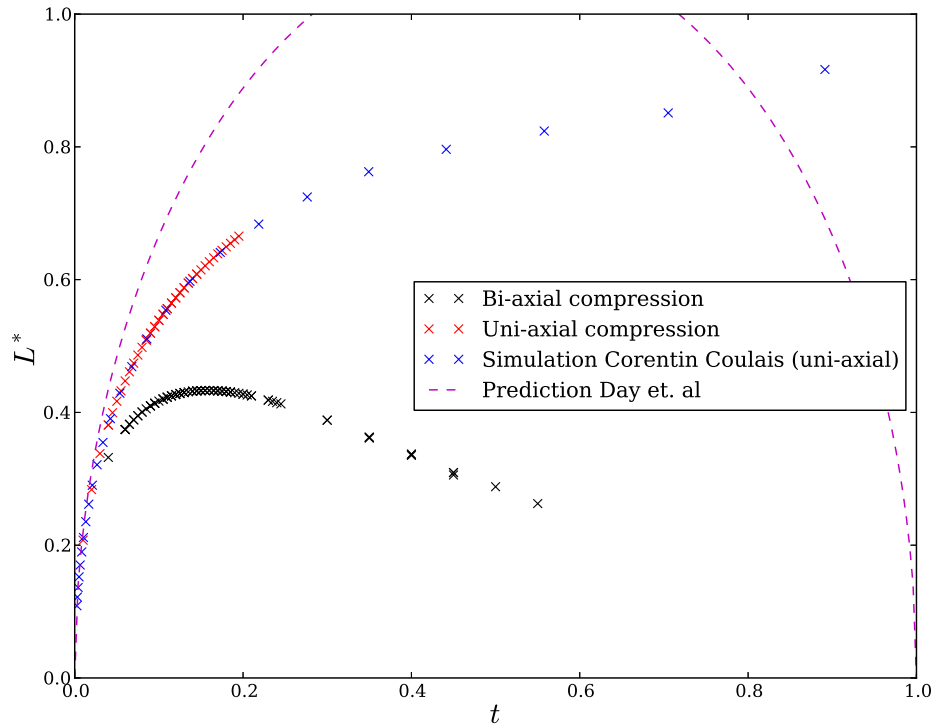


Figure 5.7: Effective beam length estimation following equation (5.18) for both uni-axial and bi-axial compression. In addition to the experiments carried out for this thesis, simulations from Coulais et al. have been added[22] and the prediction from Day et al.[21].

Correction to predicted effective length

The calculated effective length by Day et al.[21] doesn't seem to work in the case of the Holey Sheet for almost all filament thickness's as we saw in figure 5.7. Therefore we could try to see whether the assumptions made in their derivation of the effective length are the cause of this failure or whether other explanations must be found. We therefore return to figure 5.6 and the accompanying integral in equation (5.7). This time we integrate over the whole filament and do not approximate the function $A(x, t)$. Furthermore we split the integral in three parts, one part over the curved part of the filament, others over the top and bottom:

$$\int \frac{1}{A(x, t)} dx = \int_R^{\frac{1}{2}} \frac{1}{A(x, t)} dx + \int_{-R}^R \frac{1}{A(x, t)} dx + \int_{-\frac{1}{2}}^{-R} \frac{1}{A(x, t)} dx. \quad (5.21)$$

Here we have used that the filaments have a normalized length of 1. In addition it is useful to notice that $t + 2R = 1$, so that all terms involving R can be rewritten to a dependency on t . In the first and the last integral $A(x, t)$ is a very simple function, namely $A(x, t) = 1$. Therefore we find

$$\int \frac{1}{A(x, t)} dx = 1 - 2R + \int_{-R}^R \frac{1}{A(x, t)} dx = t + \int_{-R}^R \frac{1}{A(x, t)} dx. \quad (5.22)$$

For the curved part we change variables to ϕ using the fact that $x = R \sin \phi$. This yields

$$\int \frac{1}{A(x, t)} dx = t + \int_{-\frac{\pi}{2}}^{\frac{\pi}{2}} \frac{R \cos \phi}{t + 2R(1 - \cos \phi)} d\phi = t + 2 \int_0^{\frac{\pi}{2}} \frac{R \cos \phi}{1 - 2R \cos \phi} d\phi. \quad (5.23)$$

This integral can be carried out exactly to yield

$$\int \frac{1}{A(x, t)} dx = t + 2 \left(-\frac{\pi}{4} + \frac{1}{\sqrt{1 - 4R^2}} \tan^{-1} \left(\frac{\sqrt{1 - 4R^2}}{1 + 2R} \right) \right). \quad (5.24)$$

We want to have an expression that only depends on the filament thickness t , and therefore, rewrite

$$G(t) = \int \frac{1}{A(x, t)} dx = t - \frac{\pi}{2} + \frac{2}{\sqrt{1 - 4R^2}} \tan^{-1} \left(\sqrt{\frac{1 - 2R}{1 + 2R}} \right) = t - \frac{\pi}{2} + \frac{2}{\sqrt{t(2-t)}} \tan^{-1} \left(\sqrt{\frac{t}{2-t}} \right). \quad (5.25)$$

We see that $G(t)$ is equal to the ratio of the length of the effective beam to its width. The expression derived here has the nice feature that $G(t) \rightarrow 1$ for $t \rightarrow 1$, which is what we would expect, since for $t = 1$ we are simply compressing a square without holes, and thus, the ratio of length and width is the identity.

From this expression we find a different effective length, namely

$$L^* = tG(t) = t \left(t - \frac{\pi}{2} + \frac{2}{\sqrt{t(2-t)}} \tan^{-1} \left(\sqrt{\frac{t}{2-t}} \right) \right). \quad (5.26)$$

Uni-axial compression

The corrected prediction of L^* is plotted in figure 5.8 and it can be observed that it describes the overall picture of the simulations much better than the original prediction by Day et al.[21], which is expected since the original prediction makes assumptions which are only valid in the limit of small t . However, the corrected prediction is still off and seems only to be correct for

small t as well, for larger t it underestimates the simulated values. In the limit of $t \rightarrow 1$ the prediction and simulation seem to agree again and both converge to the expected value of 1. The measurements seem to indicate that there are some other factors contributing to the exact behaviour. One of these might be a non-uniform F over the filaments. The integrals then have to include $F(x)$ as well and this might change the predictions to better match the observations.

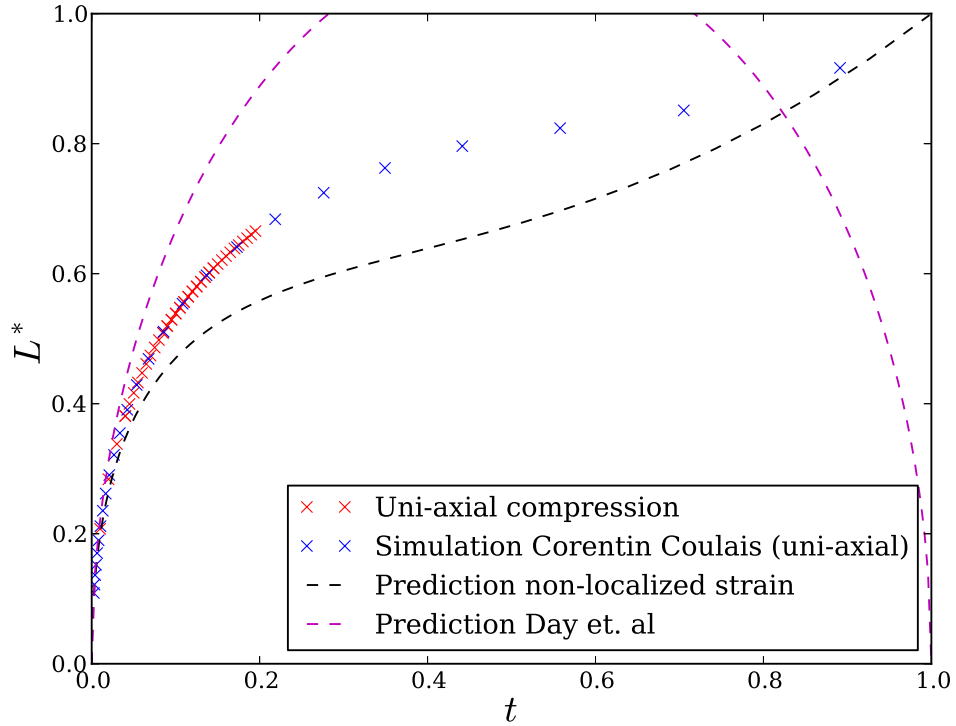


Figure 5.8: Effective beam length estimation following equation (5.18) for uni-axial compression with the corrected prediction of Day et al.[21]. In addition to the experiments carried out for this thesis, simulations from Coulais et al. have been added[22].

Bi-axial compression

Another key feature can be seen from figure 5.7, namely the difference between uni-axial and bi-axial compression. The effective length for the uni-axial compression is always higher. This can be understood by considering the Poisson's ratio of the Holey Sheet and equation equation (5.20). We see that ν plays a role in the effective beam length. Since ν relates the compression and expansion of the x and y direction to each other, this offers the explanation of the different behaviour of bi-axial and uni-axial. Since ν will lie in between 0 and 1 we can already anticipate that $L_{uni}^* \geq L_{bi}^*$ from (5.20).

For the limit of really thin filaments $t \ll 1$ we can imagine that $\nu \approx 0$ because there is almost no link between the horizontal and vertical beams. Therefore the compression in one direction will have minimal influence on its orthogonal direction. When we take the limit $t \rightarrow 1$ we shrink the circles and will approximate a solid rubber material which is incompressible and therefore has $\nu = 1$. This explains the fact that $L_{bi}^* \rightarrow 0$ for $t \rightarrow 1$ as seen in the simulations. In between these limits it seems that there is a competition between the effect of Poisson's ratio, which shrinks the effective length, and the geometrical extra contribution to the effective area, which

makes the effective length larger.

We can find $\nu(t)$ from the uni-axial simulations and use it to rescale the effective lengths of the uni-axial simulations. We see that they coincide with the actual bi-axial simulations. This is of course expected since the effect of ν is purely a mechanical feature and has nothing to do with the actual structure of the Holey Sheet.

The re-scaled uni-axial simulations using ν are plotted together with the original bi-axial compression simulations and they collapse onto the same curve, see figure 5.9. Furthermore a new predicted effective length is plotted based on the the aforementioned integrals. The only difference now being the region over which the integration is carried out. Since we perform a bi-axial compression there is no room for the center islands to be compressed or to expand. Therefore we propose to integrate over only that part of the filaments that is not bi-axially compressed as sketched in figure 5.10. The function $G(t)$ therefore changes to

$$G(t) = \int \frac{1}{A(x)} dx = \int_{-\frac{\pi}{4}}^{\frac{\pi}{4}} \frac{R \cos \phi}{1 - 2R \cos \phi} d\phi = -\frac{\pi}{4} + \frac{2}{\sqrt{t(2-t)}} \tan^{-1} \left(\sqrt{\frac{t}{2-t}} \tan \left(\frac{\pi}{8} \right) \right). \quad (5.27)$$

A similar conclusion regarding the corrected prediction of L^* can be made compared to the uni-

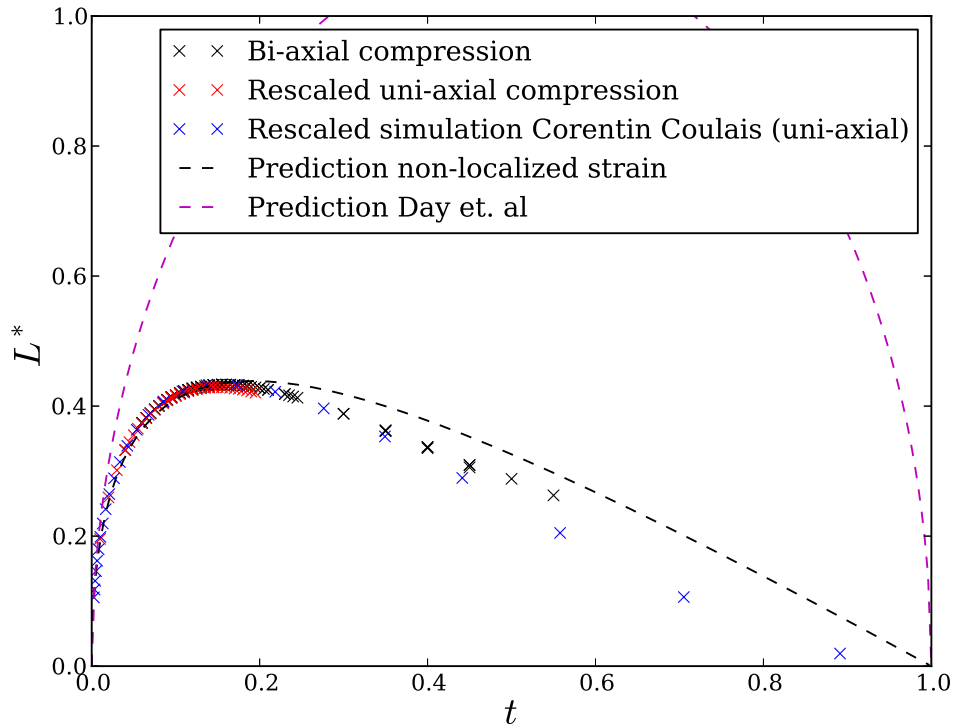


Figure 5.9: Effective beam length estimation following equation (5.18) for bi-axial compression with the corrected prediction of Day et al.[21]. The uni-axial compression simulations are in presented in re-scaled version using (5.20). Data from Coulais et al. has been added and re-scaled as well[22].

axial case. It can be observed that it describes the overall picture of the simulations much better than the original prediction, but it now seems to overestimate the effective length, the actual simulations show therefore a more stiff response as shorter beams are harder to compress.

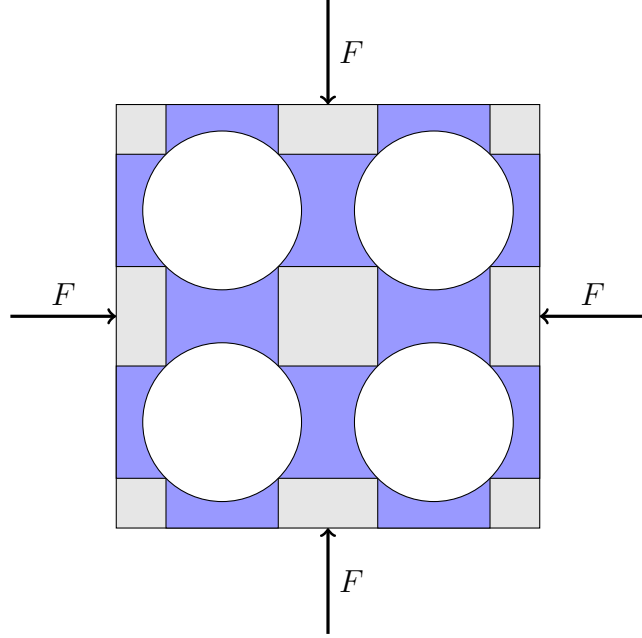


Figure 5.10: Sketch of the beam filaments (in blue) which are considered to be responsible for the effective beam length in the bi-axial compression simulations.

5.3.2 Method II: Critical Euler load

From the Euler elastica theory [23] we know that for a two dimensional beam which is compressed at both ends, the predicted Euler buckling load is given by

$$F_c = \frac{\pi^2 EI}{L^2}, \quad (5.28)$$

where I is the two dimensional moment of inertia. Now using the relations between F and u we can find an expression for the critical displacement,

$$u_c = \frac{1}{k} F_c = \frac{L}{EA} \frac{\pi^2 EI}{L^2} = \frac{\pi^2 I}{AL}. \quad (5.29)$$

Then we compare again to a uniform beam with length L^* and width t . For this setting we have that

$$I = \frac{t^3}{12} \quad (5.30)$$

and substituting all this in (5.29) we get the expression relating u and t ,

$$u_c = \frac{\pi^2}{t L^*} \frac{t^3}{12} = \frac{\pi^2 t^2}{12 L^*}. \quad (5.31)$$

Using this equation we can get L^* from measurements of u_c and t via

$$L^* = \frac{\pi^2 t^2}{12 u_c}. \quad (5.32)$$

On first inspection of (5.31) we expect $u_c \sim t^2$. However, since L^* doesn't have to be a constant function of t we can try to capture deviations from perfect quadratic behaviour of u_c in the effective length L^* of the beam. Figure 5.11 shows the computed critical displacements for different filament thickness's for both uni-axial and bi-axial compression. We can already observe on first glance that the uni-axial case shows more similarities to a quadratic behaviour than the bi-axial case, especially for moderate values of t .

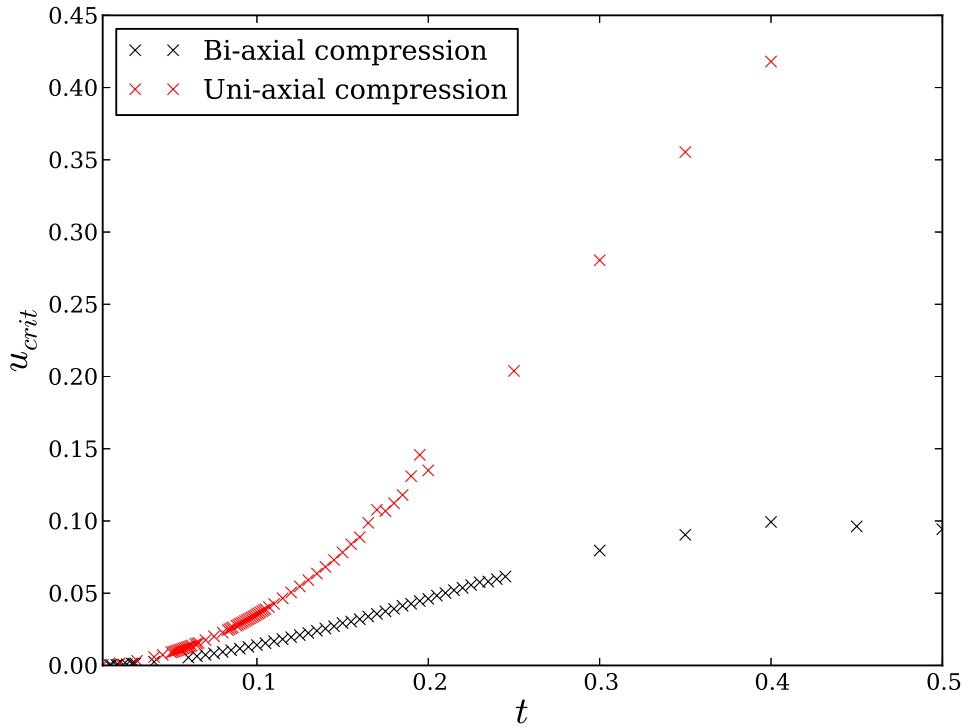


Figure 5.11: Critical buckling displacement as a function of filament thickness parameter on a log-log scale for both uni-axial (red) and bi-axial (black) compression. Inset shows the linear scale plot.

Uni-axial compression

We first compare the uni-axial compression critical loads with a t^2 like behaviour in a log-log plot, see figure 5.12. It can be seen that the simulations seem to collapse on a quadratic curve. The relative error of this fit is quite small over a wide range of t .

As a result the calculated effective length L^* using (5.32) will result in a nearly constant effective length, see figure 5.14.

Bi-axial compression

For the bi-axial case we observe something very different, see figure 5.13. As t grows u_c starts to deviate from t^2 -like behaviour, which can be clearly seen by looking at the relative error of a quadratic fit. We see that there is a peak in the critical displacement around $t \approx 0.4$.

Whereas the difference between the uni-axial and bi-axial case could be explained by a mechanical transformation for the first method, we observe here probably a more fundamental difference between the uni-axial and bi-axial compression. Due to the coupling between the beams in the horizontal and vertical direction the behaviour of the critical point might change as we have observed.

Different effective lengths

Our previous results show that there is a difference in the behaviour of the critical displacement depending on the type of forcing. We now try to see how the effective length defined by equa-

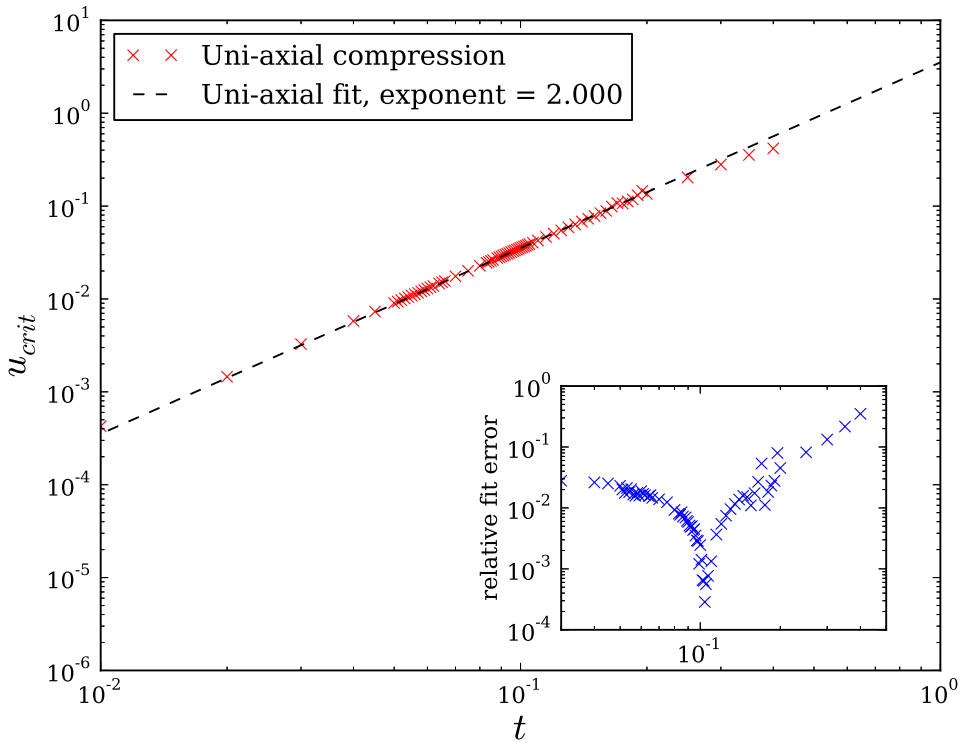


Figure 5.12: Critical buckling displacement as a function of filament thickness parameter on a log-log scale for the bi-axial compression and a quadratic fit (dashed). Inset shows the error made in the fit relative the the value of the u_c .

tion (5.32) behaves as a function of t . Indeed it seems that the estimated effective length for uni-axial compression is nearly constant and has a value of about $L^* \approx 0.5$. For the bi-axial case the effective length seems to start at 1.0, two times as high, but only to deviate from this value quite quickly soon after $t \approx 0.1$. It even reaches values larger than 1.0, which would mean that we model the Holey Sheet as a beam with an increasing aspect ratio of width versus length. The aspect ratio gives a rough indication for the softness of a beam, as slender beams are easy to compress whereas thick beams resist more to compression. The predicted effective length by Day et al. seems to be totally off, which is suspicious. The approximation should hold at least for the slender limit of small t .

A possible explanation for these observations might be that we have been too quick in substituting formulas into each other in deriving (5.32). Since buckling is really a competition between compression of the beam and bending of the beam there might be two different effective lengths at work, both with different behaviour depending on t . We might need to consider one length for compression and one for bending. In the article of Day et al.[21] they also derive different expressions for bending and compression. However, these are related by a simple factor,

$$L_{bend}^* = \frac{3}{16} L_{compress}^*. \quad (5.33)$$

Now the question is how these different length scales have to be incorporated in the calculations. The stiffness of the pre-buckling phase is purely a result of compression and therefore we expect the following to hold

$$k = \frac{EA}{L_{compress}}. \quad (5.34)$$

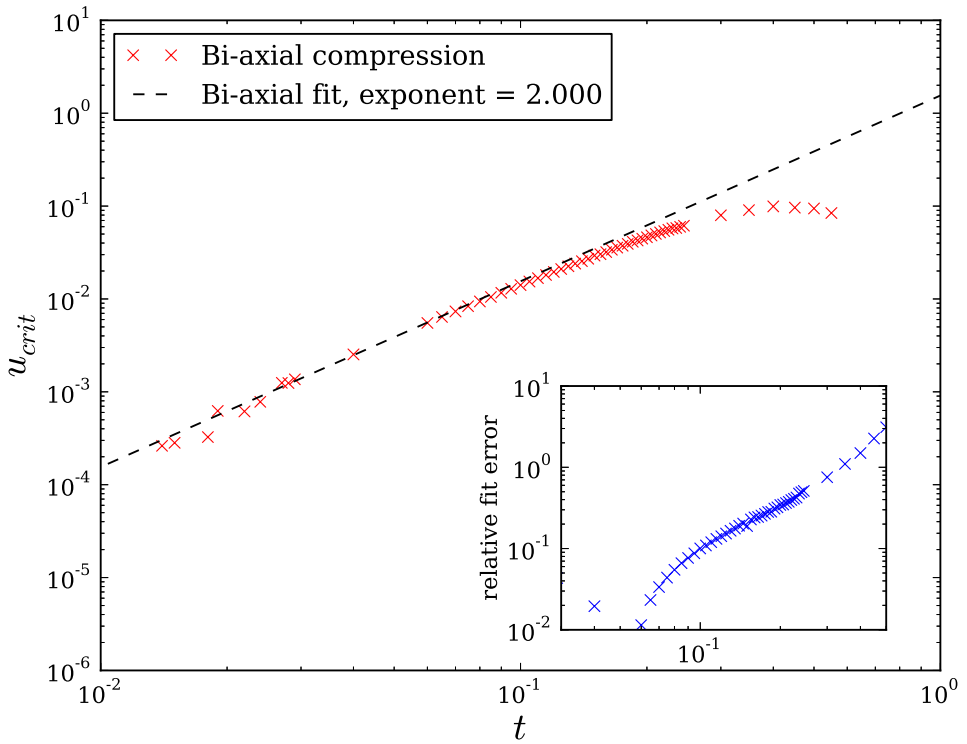


Figure 5.13: Critical buckling displacement as a function of filament thickness parameter on a log-log scale for the uni-axial compression and a quadratic fit (dashed). Inset shows the error made in the fit relative the the value of the u_c .

In contrast, the buckling of a beam really has to do with both the bending of the beam and its compression. The question is at which force does it become energetically more favourable for the beam to bend than to compress. Two possible forms of F_c can be proposed depending on the interpretation of the L^2 factor,

$$F_c = \frac{\pi^2 EI}{L_{bend}^2} \quad (5.35)$$

and

$$F_c = \frac{\pi^2 EI}{L_{bend} L}, \quad (5.36)$$

where L is now the length of the actual filament and thus equal to 1 in our case. The first one can be derived by simply substituting L_{bend} for L . The other one can be motivated by a different kind of modelling of the filaments, namely as beams with hinges, see figure 5.15. Since the bending of the filaments is localized at the thin parts only, we can model this by a hinge part in the beam. This model is likely to be valid only for small t where we expect deformations to be localized whereas for larger t displacements will be more spread out over the filaments. We can derive for this model a similar buckling equation by balancing the moments on the hinge. The moment exerted by the force can be expressed as

$$M = F \frac{L}{2} \sin \alpha. \quad (5.37)$$

Furthermore elastic theory predicts that

$$M = EI\kappa', \quad (5.38)$$

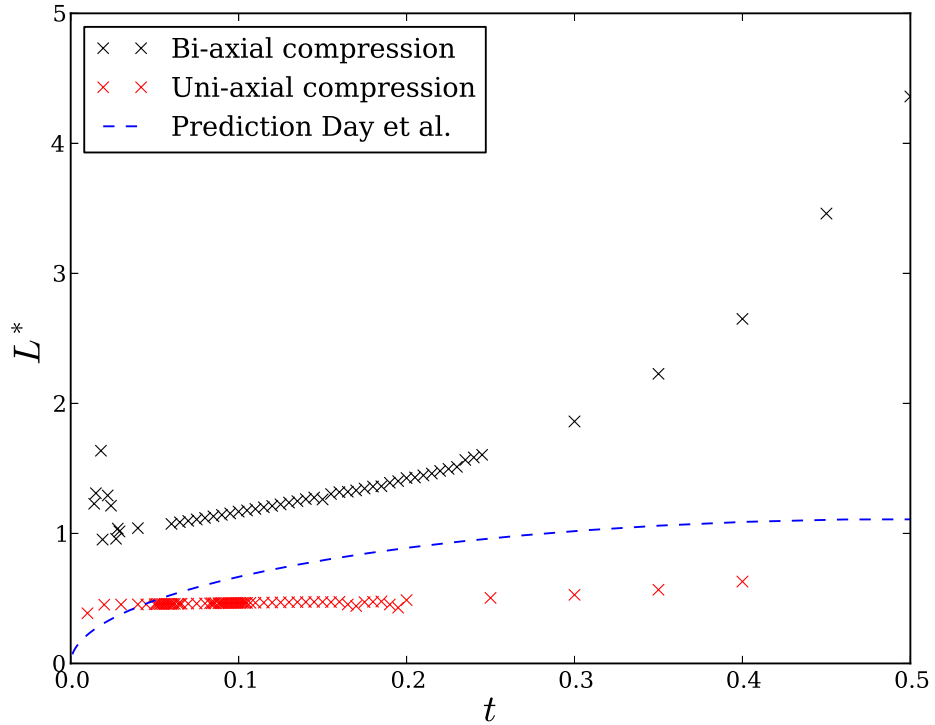


Figure 5.14: Effective length as a function of filament thickness estimated by use of (5.32) for both the uni-axial and bi-axial compression. In addition to the data the predicted value of L^* as given by (5.19) is plotted which does not seem to match the data.

where κ' is the curvature of the hinge. Since we are interested in the buckling point, we can assume that the angle α is small. This allows us to approximate the curvature $\kappa' \approx \frac{2\alpha}{L_{bend}}$. Only the length of the hinge comes into play, since the curvature is due to the hinge only. As a result we get a new relation for F ,

$$F = \frac{4EI}{LL_{bend}} \frac{\alpha}{\sin \alpha}. \quad (5.39)$$

This relation models the buckled phase, but we are interested in the actual buckling point. Therefore we let $\alpha \rightarrow 0$ and get an expression for F_c ,

$$F_c = \frac{4EI}{LL_{bend}}. \quad (5.40)$$

The steps that follow to derive an expression for u_c are similar to the ones we already saw and therefore we immediately state that

$$u_c = \frac{4t^2}{12L} \frac{L_{compress}}{L_{bend}}. \quad (5.41)$$

Therefore the actual expression for u_c , not only for small t , is expected to be related to effective lengths like

$$u_c \propto \frac{t^2}{L} \frac{L_{compress}}{L_{bend}}. \quad (5.42)$$

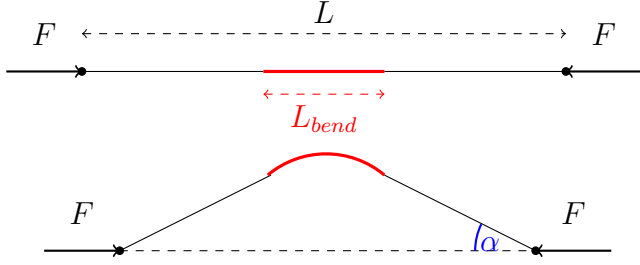


Figure 5.15: Model for the filaments as beams with a hinge part which will bend when the beam buckles. The hinge part is modelled with a length L_{bend} which is supposed to be much smaller than L . The angle that the beams make with the horizontal direction is denoted by α .

As a result, our earlier prediction L^* is not a measure of an effective beam length, but actually measures

$$L^* = L \frac{L_{bend}}{L_{compress}}. \quad (5.43)$$

Now the prediction that $L_{bend} \propto L_{compress}$ by Day et al.[21] implies that we actually should measure a constant L^* in the uni-axial case and this is exactly what we saw in figure 5.14. To check how the different length scales come out of the simulations we plot L_{bend} from $L_{compress}$ and L^* ,

$$L_{bend} = L^* \frac{L_{compress}}{L}. \quad (5.44)$$

The result is presented in figure 5.16 and it shows that for small t the prediction of Day et al. indeed seems to be valid. However, just as we saw in the earlier predictions, the validity of the predictions is severely limited by the size of t . The bi-axial bending length turns out to be bigger than that found for uni-axial simulations. Furthermore, the behaviour as t grows is very different. It seems that L_{bend} increases quickly for moderate values of t , even to values above 1, the actual length of the filaments. This of course could be given as the explanation for the difference in behaviour of the critical displacement u_c between uni-axial and bi-axial. However, this merely seems as shifting the problem from one parameter to another since no explanation for the behaviour of L_{bend} could be found so far.

On the other hand we can use L^* as a measure of the ratio between bending and compression as we saw in (5.43). Therefore the fact that L^* increases for the bi-axial case implies that it gets more favourable for the beams to bend, and thus buckle, than to compress any further. A possible explanation for this would be related to the Poisson's effect. Whenever in the bi-axial case a part of the material compresses, another part has to expand (remember that the material itself is incompressible). However, less and less space remains available for this expansion, because in all directions this expansion is taking place. Therefore this proposed geometrical effect might result in a higher stiffness, an added geometrical stiffness, compared to the bending stiffness and therefore we see a clear result of the attempts to break the symmetry in our forcing of the system. It seems that this difference kicks in when bending of filaments becomes important.

5.4 Post-buckling phase: large deformations

In comparing the Holey Sheet to a beam we can also compare the behaviour after the buckling point and see whether the modelling keeps valid. Since we now focus on the phase after the

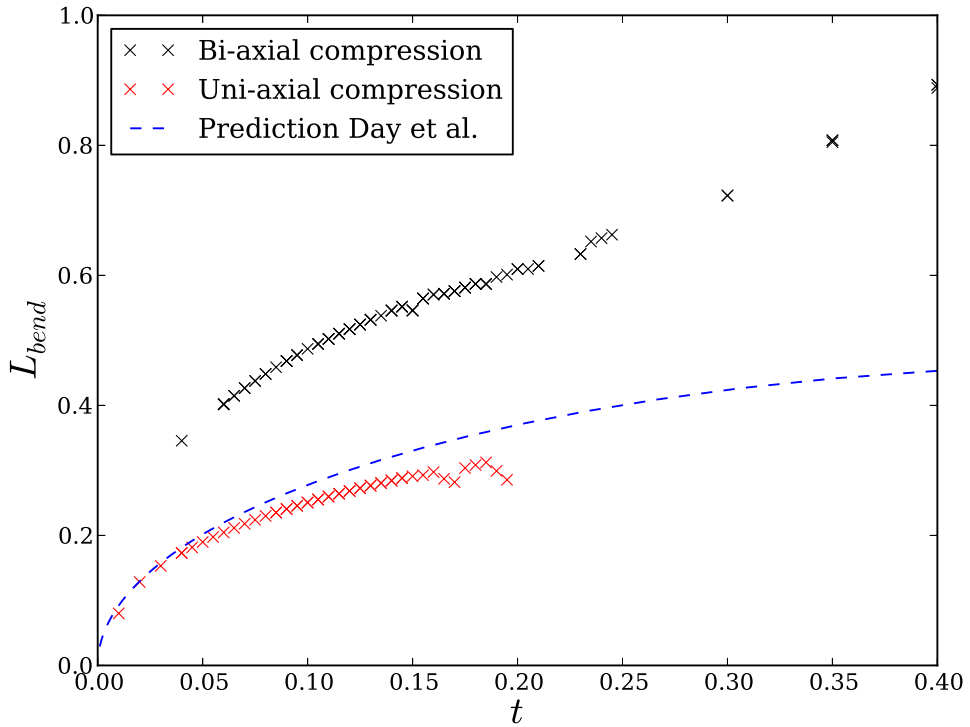


Figure 5.16: Effective bending length as a function of filament thickness estimated by use of (5.44) for both the uni-axial and bi-axial compression. In addition to the data the predicted value of L_{bend} as given by (5.33) is plotted.

beams or Holey Sheet has buckled we need to take large deformations into consideration. The theory needed is therefore likely to be derived from finite strain theory and non-linear elastica which is mainly out of scope for this thesis. Parts of these theories are even still in development. However, we have the possibility to make a comparison to simulations and experiments on the buckling of rectangular (thick) beams in order to see whether the beam-mapping still makes sense.

5.4.1 Method I: Post-buckling stiffness

A relation between F and u in the post-buckling phase often involves a critical force F_c and $\Delta u = u - u_c$ the displacement after the critical displacement. The form of this relations can in general be written like

$$F = F_c (1 + S\Delta u), \quad (5.45)$$

where S is therefore the slope of the post-buckling phase of the $F - u$ curve and can thus be interpreted as the post-buckling stiffness. Different values for F_c can be used depending on the model taken, but most common choices are the actual F_c or the predicted Euler critical force (5.36). For the in-extensible beams, Euler elastica predicts a slope of $\frac{1}{2}$. The question is whether this can be observed as a limit value for $t \rightarrow 0$, just as we retrieved slender limit results in the preceding sections.

In order to compare our results to beam experiments we have to rescale all measurements to dimensionless quantities. For the slope, we rescale our measured slope by the critical force, as mentioned before. For the width of our beam we introduce the dimensionless quantity aspect

ratio, which is equal to the width divided by the length for a ordinary straight beam. There is however one problem with this aspect ratio, as we have now defined different effective lengths depending on whether we compress or bend. It is not immediately clear which effective length (and thus beam) we should use. However, in the post-buckling phase of beams it is mostly bending which determines the behaviour and therefore we expect the same to hold for the Holey Sheet. We thus calculate the aspect ratio by using L_{bend} . The results are shown in figure 5.20, where S has been calculated from the measured slope in two ways. The first uses the measured critical force and the second the calculated critical Euler load.

From the figures we can see that it seems that the limiting value is indeed 0.5 just as in-extensible beam theory predicts. Therefore it seems that in the thin filament limit the Holey Sheet might behave as an in-extensible beam. In this thin limit there is again no difference between uni-axial or bi-axial compression just as we observed in the preceding sections. The likely reason for this still being that in thin filament limit all displacements and stresses are that much localized at the centers of the filaments that there is no coupling between the different directions of the beams. It is also clear from the figures that if we want to compare the simulations to beams, the rescaling by the Euler load gives better results. This should not come as a surprise, as we want to compare our results to beams and therefore we need to use the effective critical force, the Euler load, as well. If we thus use figure 5.20b, we can see that in fact the bi-axial compression seems to fit the plain beam simulations, for values up to at least $t = 0.20$. In contrast, the uni-axial compression is totally off, compared to plain beams. It thus seems that there is a breakdown in the beam modelling after the buckling point, where we still can model the bi-axial compression of a Holey Sheet as compressing beams, but not for the uni-axial compression.

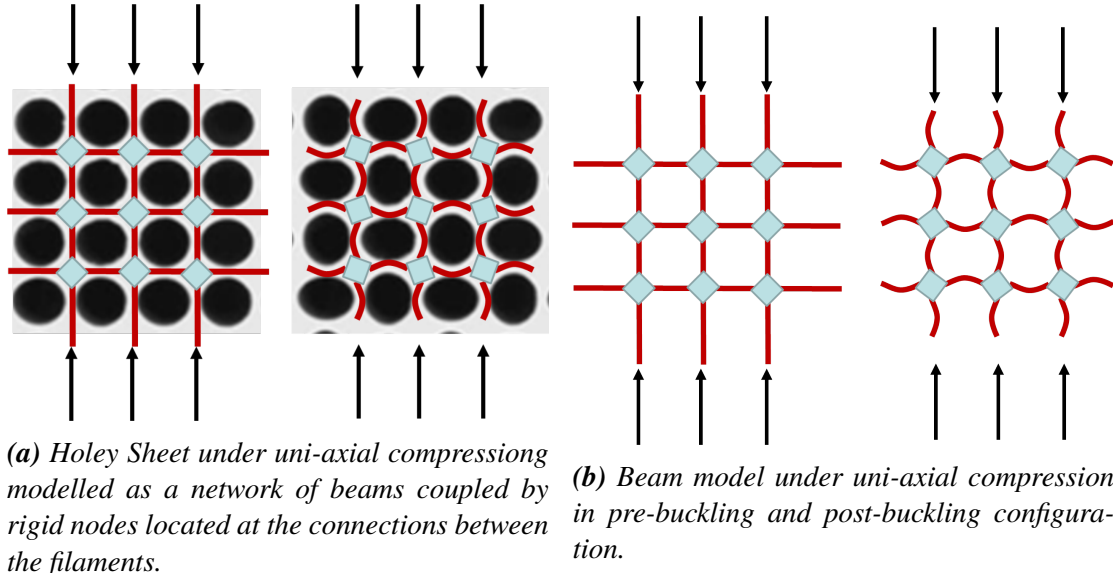


Figure 5.17: Possible explanation for the breakdown of beam modelling in the case of uni-axial compression of the Holey Sheet, the Holey Sheet being equal to a network of coupled beams, which in the post-buckling phase are interacting. Due to this interaction the single beam model is likely to lose its validity.

This breakdown might be explained by the symmetry breaking induced by the buckling. As we can see in figure 5.17, the modelling of the Holey Sheet as a beam, can in fact be viewed as a network of beams connected by nodes in the center islands. When in the uni-axial case a force is applied, work is done on the vertical beams by this force, both in the pre-buckling and post-buckling phase. In the pre-buckling phase the horizontal beams do not contribute

to the behaviour of the vertical beams, which are thus solely responsible for the pre-buckling response and equal to the aforementioned effective beams. In the post-buckling phase, however, we observe a connection between the horizontal and vertical beams, as the horizontal beams are bent, although no work is done on this beams by the external force. These horizontal beams exert a torque via the center nodes on the vertical beams due to this bending. Therefore the response cannot be modelled any more as being the result of the compression of the vertically aligned beams. The network beam modelling suggests that a coupled beam network should be able to describe the post-buckling behaviour better, but the investigation of this idea was outside the scope of this thesis.

The preceding results suggest that it might not be possible to compare the results of the post-buckling phase to single beam models. Therefore we plot the results of the simulations without rescaling to beam models as well, see figure 5.18.

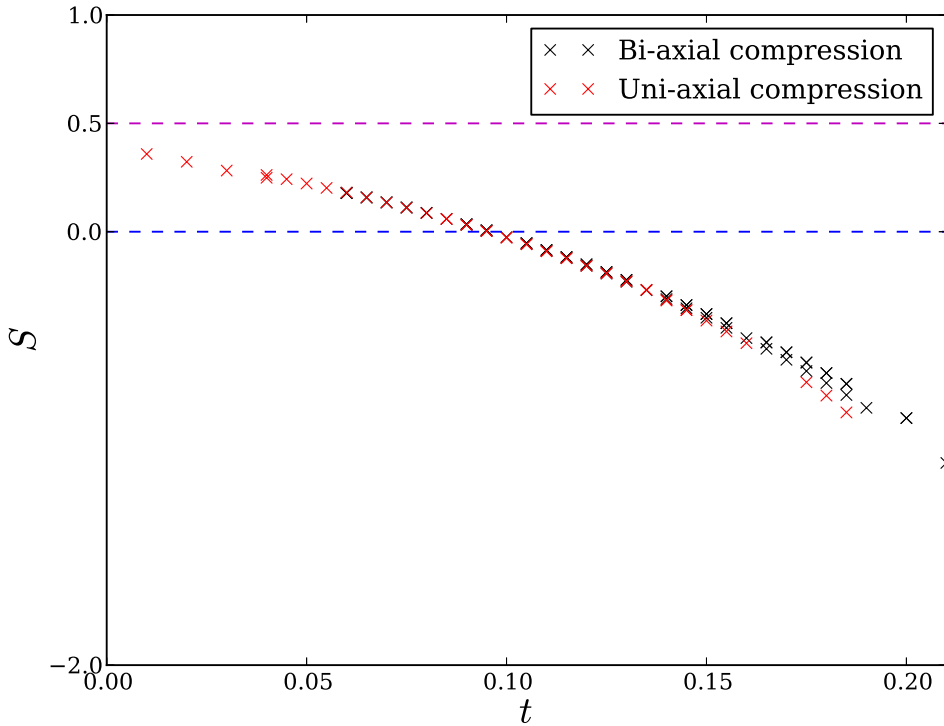
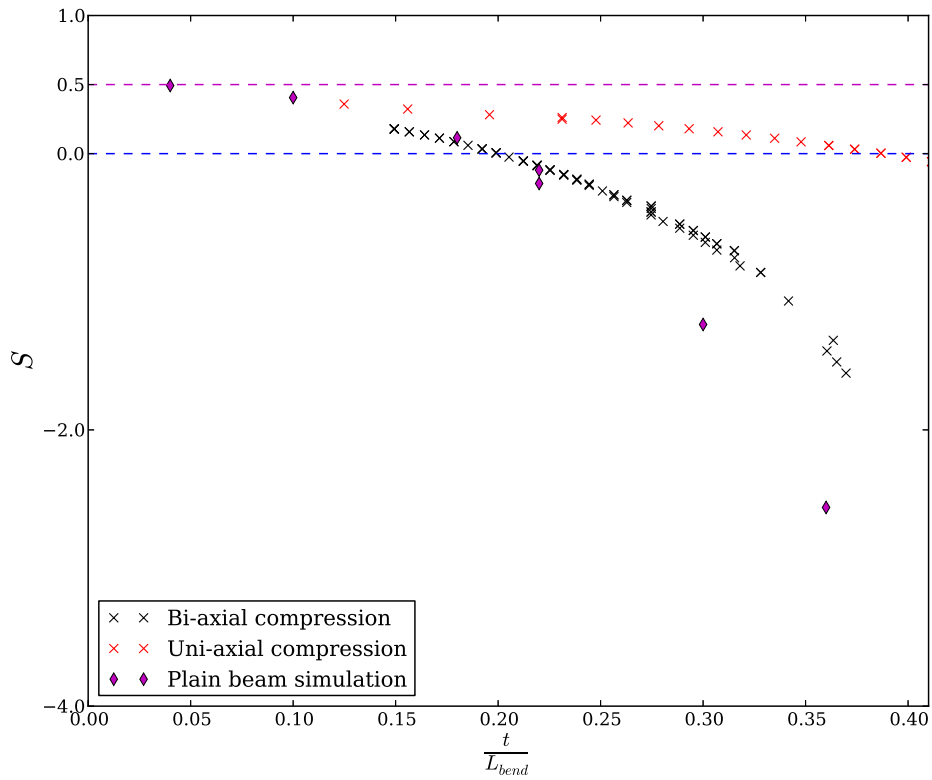
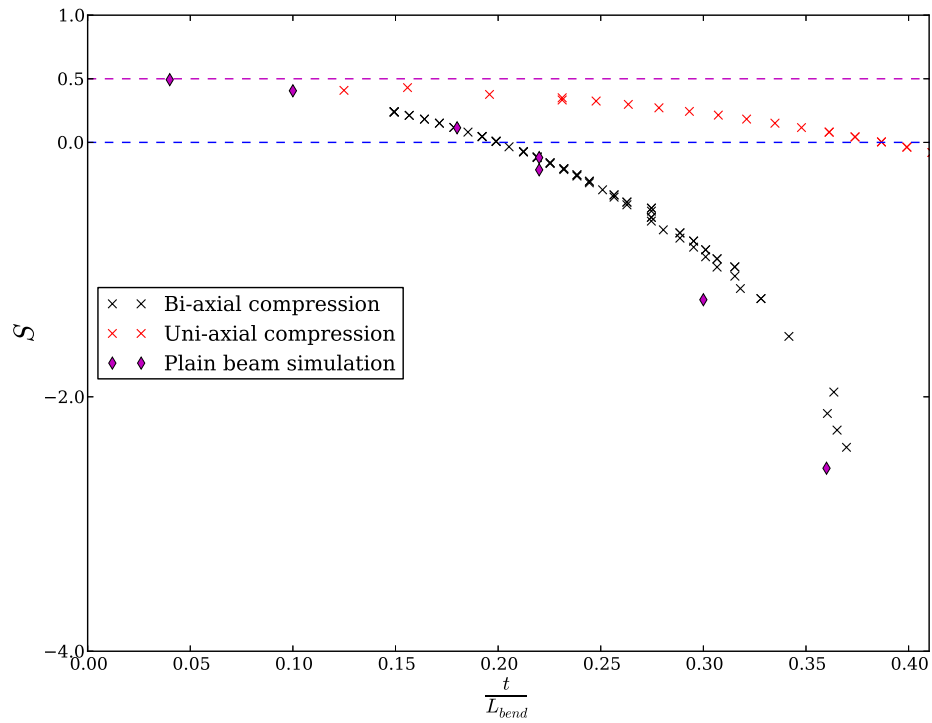


Figure 5.18: The measured slope rescaled by the measured critical force F_c as a function of filament thickness t . The slope seems to cross 0 at $t = 0.095$, indicating the onset of snap-through buckling.

First of all, it can be observed that now there is little difference between the uni-axial and the bi-axial case. They both start near the predicted 0.5, although it is questionable whether this is really the limit value that we observe. The slope then changes sign around $t \approx 0.095$, resulting in a negative stiffness. This is evidence for so called snap-through buckling. Snap-through buckling is a special form of buckling where the solution 'snaps' from one equilibrium solution to another branch. For the Holey Sheet this occurs when the force displacement curve has a peak and the force is increased beyond this peak. As the solution branch cannot make the force increase more, a branch-switch has to occur, see figure 5.19. As a result a large (almost) instantaneous displacement will be produced. This fast movement can prove to be applicable in fast mechanical switches. The negative stiffness, if we use $F = ku$, results in a force which



(a) Measured slope rescaled by the measured critical force.



(b) Measured slope rescaled by the calculated critical Euler force (5.36).

Figure 5.20: Plot of the rescaled measured slope as a function of the aspect ratio. The aspect ratio for the Holey Sheet simulations is calculated by $\frac{t}{L_{bend}}$, where L_{bend} is the effective compression length as found by (5.44).

assists the created displacement instead of opposing it, as one would normally expect.

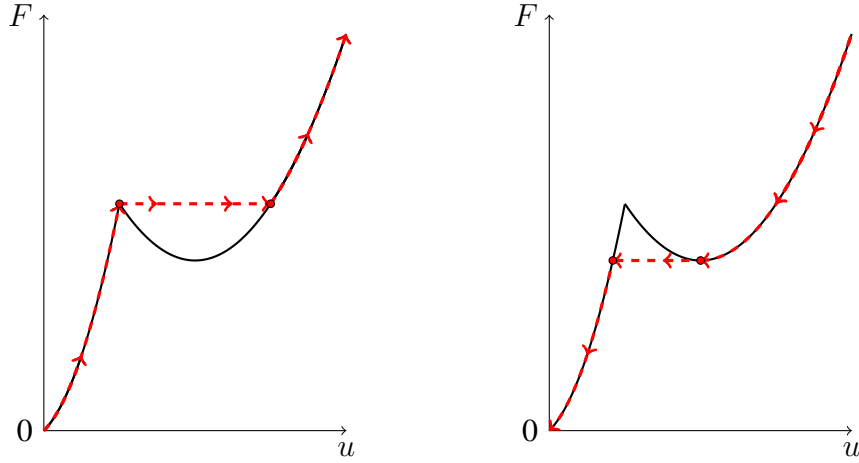


Figure 5.19: Snap-through behaviour; while increasing the force the curve meets a peak and therefore cannot both increase F and follow the curve. The result is that it skips a part of the curve and thus u rises quickly. On the way back a similar behaviour can be observed, only now when the curve meets a local minimum.

5.4.2 Method II: Force-angle relation

Another feature of the post-buckling phase which allows us to compare the Holey Sheet to beams is the relation between the force F and an angle α . In the case of beams this angle α is defined as the angle that the beam makes at the endpoints with the reference configuration, see f.e. 4.7. In the case of the Holey sheet we measure the angle of rotation of the most central node, depicted in figure 5.21. This provides a measure for the angle of the effective beam we try to model.

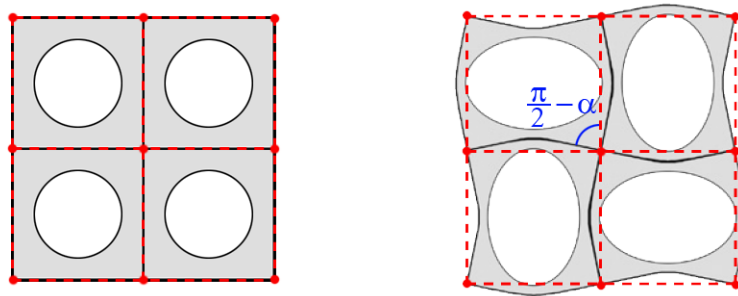


Figure 5.21: Measurement of the effective beam angle α is carried out by measuring the rotation of the center nodes of the islands, depicted by red dots. These dots are the end point of the center-lines (red dashed) through the filaments and are therefore a good candidate to represent the effective beam bending angle.

Just as for the post-buckling slope, a relation between the force F and the angle α can be derived, and in fact it bears much resemblance to the post-buckling slope equation,

$$F = F_c (1 + \kappa \alpha^2). \quad (5.46)$$

We are interested whether this kind of relation also holds for the Holey Sheet. Furthermore, the post-buckling slope showed a transition from ordinary buckling to snap-through buckling. This should be observed in the force-angle curves as well, in the form of κ , as a function of t , crossing zero.

The plot of F versus α , figure 5.24, shows that indeed there is a quadratic relation between the two variables, as the quadratic fits match the observations very precise. In figure 5.24 it can be clearly seen that indeed there is a transition between the ordinary buckling and the snap-through buckling for both uni-axial and bi-axial compression, because the curves switch from curving up to curving down for increasing t . This fact is due to the change of sign in κ . In order to determine κ we use

$$F = F_c + K\alpha^2. \quad (5.47)$$

When fitting this equation we can find K and use a rescaled version of it to compare to beam simulations. The classical Euler elastica then predicts for in-extensible beams that $\kappa = \frac{1}{8}$ should hold. Just as for the post-buckling slope we check whether this result shows up in the slender limit. To do this we rescale K by the predicted Euler load just as we did for the post-buckling stiffness. To match the bi-axial data to the plain beam results, we had to rescale κ by a factor of $\frac{1}{4}$ for some yet unknown reason. The result, 5.22, shows that for κ as well, the bi-axial case seems to match the data much better.

We observe that just as for the post-buckling stiffness, the effective single beam theory cannot

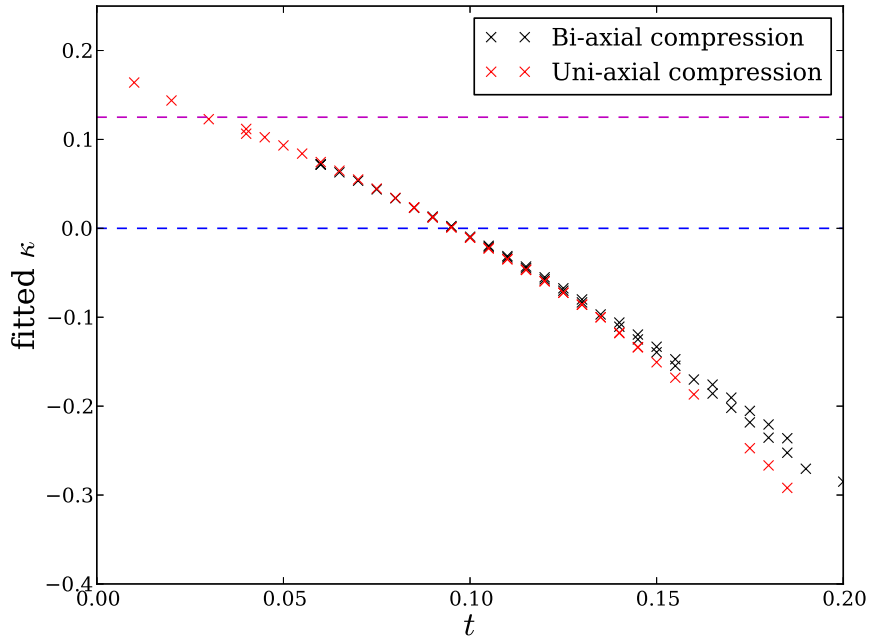


Figure 5.22: Plot of κ as a function of the filament thickness t , estimated by rescaling K found in fitting (5.47) with the measured critical force F_c . The point where κ gets zero is the transition between ordinary buckling and snap through buckling and seems to coincide with the transition value for t found in the preceding section.

fully explain the results. The data of the Holey Sheet simulations do not follow the plain beam line, and therefore, we plot, just as we did for the post-buckling slope, the data without rescaling to aspect ratio, see figure 5.22. The same trend as in the preceding section can be observed,

there is little difference between uni-axial and bi-axial compression. It is however, questionable, whether the predicted slender limit value is really observed as the datapoints for small t seem to be a little more noisy. This could be due to the fact that the extraction of the angle α for small t is more troublesome than for large t , as the simulations are more sensitive to numerical errors since small perturbations can already induce buckling and thus large deformations. The transition from ordinary buckling to snap-through buckling seems to be consistent with the post-buckling data, giving a value of $t \approx 0.95$.

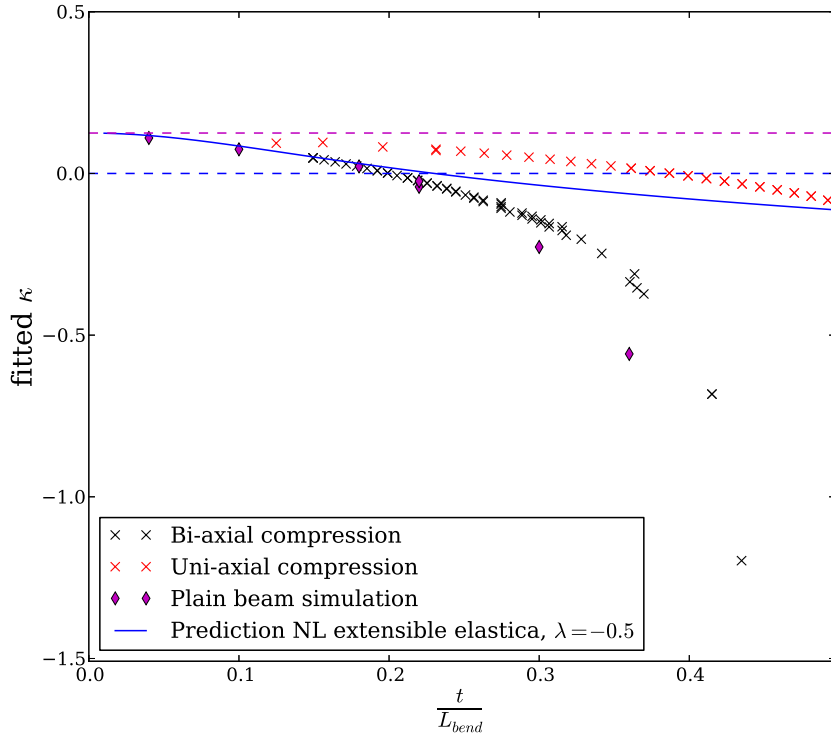
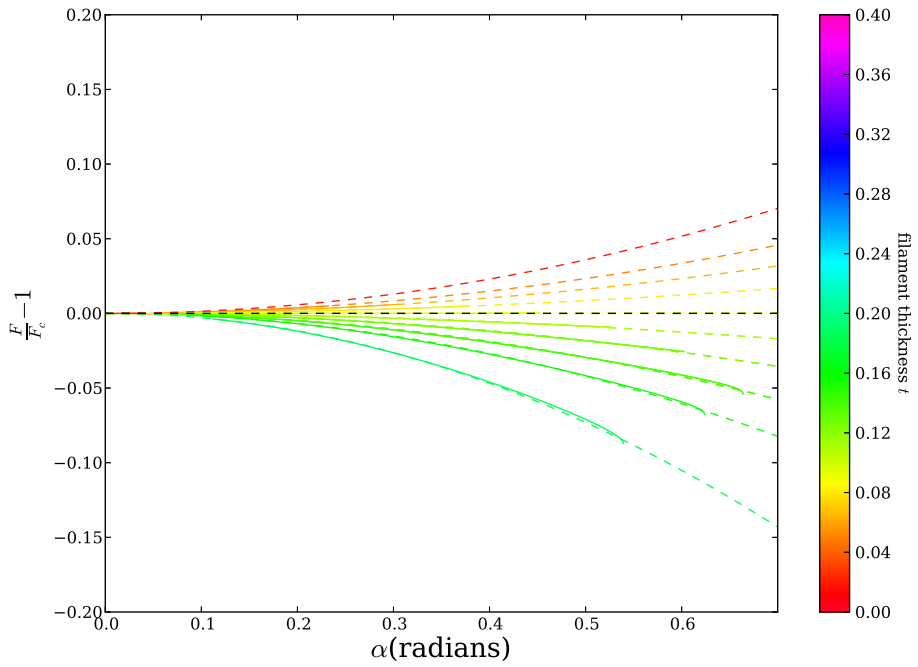
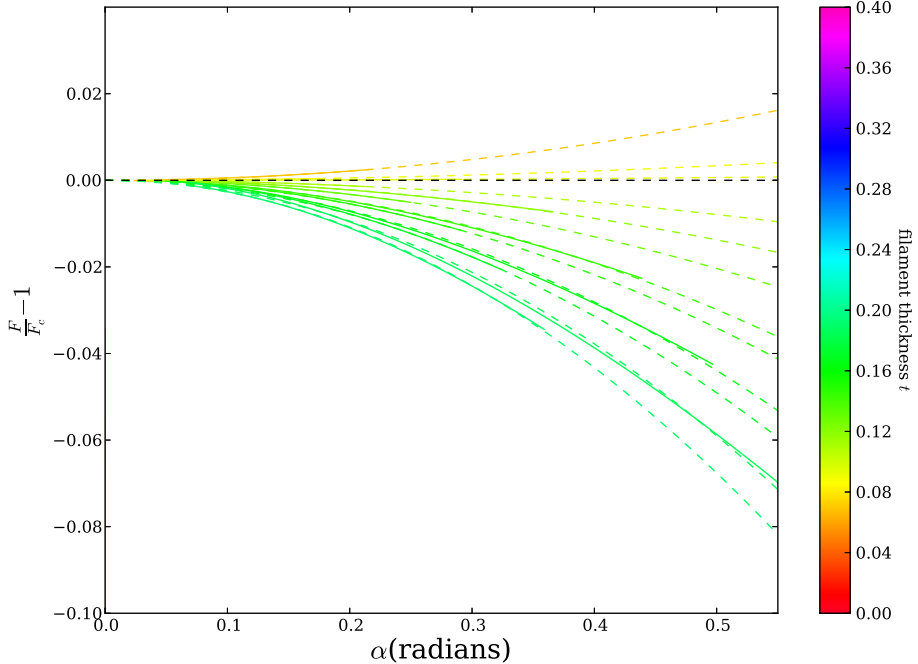


Figure 5.23: Plot of κ as a function of the aspect ratio, estimated by rescaling K found in fitting (5.47) with the critical force. The point where κ gets zero is the transition between ordinary buckling and snap through buckling. In addition, plain beam simulations are given and a prediction based on non-linear elasticity [22].



(a) Uni-axial compression.



(b) Bi-axial compression.

Figure 5.24: Plot of $\frac{F}{F_c} - 1$ versus α for different values of filament thickness t for both uni-axial compression and bi-axial compression. The quadratic fits are plotted (dashed) as well and agree very well with the simulations, indicating that indeed there is a quadratic relation between F and α . A transition between ordinary and snap-through buckling can be observed as the zero-line is crossed for t around 0.1 in both cases.

This page would be intentionally left blank if we would not wish to inform about that.

Conclusion and outlook

6.1 Conclusion

In this thesis we studied the buckling-behaviour of the Holey Sheet using numerical simulations. The response of the Holey Sheet basically splits in two parts, pre-buckling and post-buckling divided by the buckling point. We analysed these two phases separately. In order to neglect large wavelength deformations or inhomogeneities we focused on an unit cell, with which the Holey Sheet can be tiled, see figure 6.1. Of special interest for this thesis was the effect of the geometry on the response, i.e. the hole size or the thickness t of the filaments separating the holes.

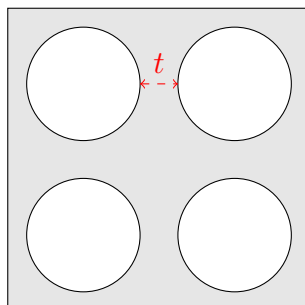


Figure 6.1: The undeformed computational unit cell as used for this thesis.

Although numerical buckling analysis often poses challenging problems[24], we were able to successfully devise a scheme to create batch simulations, exploring the parameter space of t . This was done without the need to introduce imperfection as is often customary, but gives results not accurate enough for our purpose. The force-displacement curves acquired using numerics showed much resemblance to those of (thick) beams. The natural research question, therefore, was whether an effective single beam theory could be devised, such that the effective beams have an identical response to compression as the Holey Sheet.

We performed two different mechanical tests in this thesis, namely uni-axial and bi-axial compression, since these are the only ones which initiate buckling in the Holey Sheets. The key results from this thesis are partial answers to the question whether effective beam theory works to describe the Holey Sheet. Overall we could conclude that no unambiguous answer could be given.

First of all, we found that effective beams can be defined such that they correctly describe the pre-buckling phase. However, one must note that in this phase two different effects, namely

compression and bending of the filaments, compete with each other in determining the final response. In order to incorporate both effects in the modelling of the overall response, we had to define two different effective beams, for each of these different deformations. An old theoretical model [21], which predicts the effective beams dimensions based on the geometry of the Holey Sheet, seemed to be effective only in the limit of slender filaments separating the holes. We proposed corrections to these predictions and these were able to yield better predictions, especially in the bi-axial case.

Secondly, it was more troublesome to match the post-buckling behaviour of the unit cell to effective beams. A possible explanation for this breakdown in modelling relied on the fact that due to the symmetry-breaking induced by the buckling, a coupling between the horizontally and vertically aligned filaments arises which is not present in the pre-buckling phase. Due to this coupling, single beam theory is not expected to yield correct results. This discrepancy was predominantly observed in the uni-axial case. In the bi-axial case the results were closer to that of plain beams, if we modelled the Holey Sheet behaviour as if it was dominated by deformations due to bending of the filaments. Finally, despite the fact that effective single beam modelling could not account for the correct response in this phase, we observed a very interesting phenomena in the simulations. It was found that a transition between ordinary buckling and snap-through buckling occurred at $t \approx 0.095$. This onset of the non-standard snap-through buckling for already small filament thicknesses t could prove to be interesting for future applications.

6.2 Outlook

To begin with, a solution to the mismatch of beams and the Holey Sheet could be to include multiple beams instead of single beams. As we expect that the breakdown of effective single beam modelling was caused by a buckling-induced coupling between beams in different directions, a starting point of further research could be the behaviour of a coupled beam system, such as the Roorda-frame[25]. The coupling is expected to be mainly governed by a torque mutually applied by the beams via the rigid center islands. Therefore, the effect of torque on the endpoints of beams should be included as well in the study of coupled beams. The effect of torque on single beams has been studied recently in [19] and this work should then be extended to coupled beams.

Furthermore, as there seems to be good agreement between the pre-buckling response of beams and the Holey Sheet, one could try to further optimize the predictions, initiated by Day et al.[21]. The simulations show that the predictions by [21] are only valid for a very small range of t and it is interesting to see whether they can be extended. Especially for the effective bending length, there is room for improvement, as we have only calculated new predictions, concerning non-localized strains, for the effective compression length.

Additionally, we observed that, although the general behaviour of the computational unit cells coincided to great extent with that of the Holey Sheet, there is a difference in the exact post-buckling response. Since we have only focused on small-wavelength deformations, it might be interesting to see what the response in simulations would be of larger size computational domains. Laboratory experiments have shown that the onset of buckling is a localized phenomena, see 6.2, and spreads out over the whole Holey Sheet gradually. These observations hint at influence from inhomogeneities or edge effects in the overall behaviour. This could be included in the simulations on more extended computational domains.

To conclude, an interesting new approach to explain the overall behaviour of the Holey Sheet

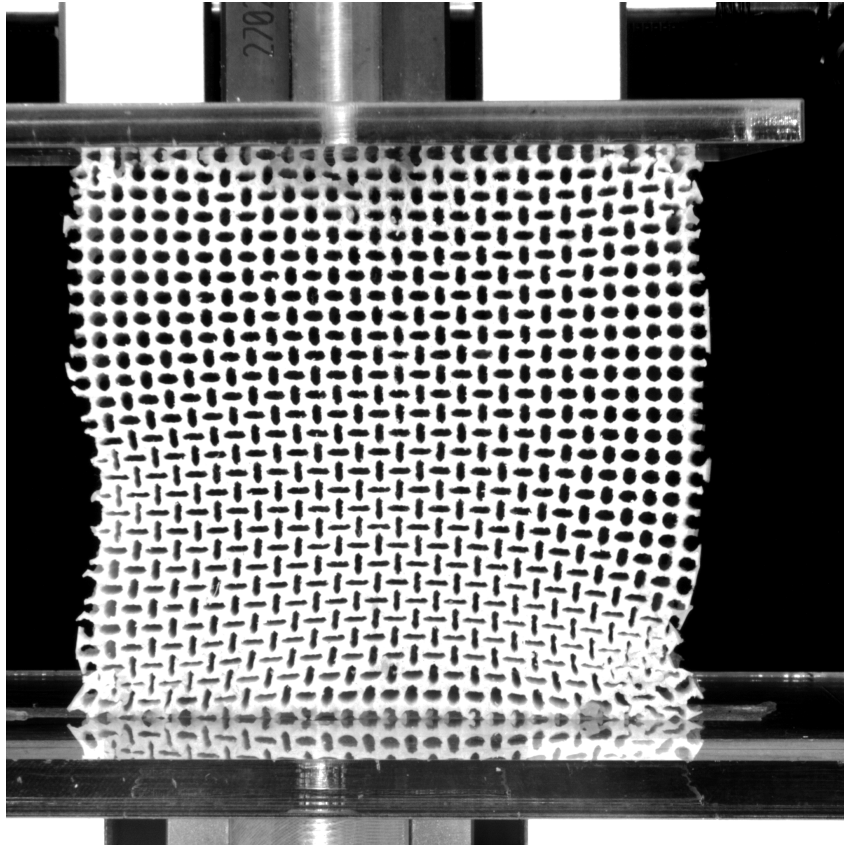


Figure 6.2: Still from an uni-axial compression experiment of a 30 by 30 Holey Sheet. The depth of the sheet is 3.1 cm, the hole size is 2.55 mm and the filament thickness is 0.45 mm. The pattern transformation spreads out gradually over the whole domain, instead of occurring at once at every spot in the material. It seems that inhomogeneities at the edges of the Holey Sheet play an important role in the onset of the buckling behaviour as well.

could be the method of homogenization[26]. This method approximates the behaviour of a heterogeneous material by that of an homogenized fictive material. The properties of this homogenized material should be approximately equal to that of the original material. The homogenized material is often chosen to represent the average of the microscopic effects taking place. Therefore, we could chose to use the unit cell of the Holey Sheet, as used in this thesis, as a possible input for the homogenized material. Already much of the behaviour of the original response of the Holey Sheet seems to be present in the unit cell and the method of homogenization might prove to be successful in extending this results to include large-wavelength effects.

This page would be intentionally left blank if we would not wish to inform about that.

References

- [1] R. Levien, *The elastica: a mathematical history*, Technical Report UCB/EECS-2008-103, EECS Department, University of California, Berkeley, 2008.
- [2] T. Mullin, S. Deschanel, K. Bertoldi, and M. C. Boyce, *Pattern Transformation Triggered by Deformation*, Phys. Rev. Lett. **99**, 084301 (2007).
- [3] K. Bertoldi, M. Boyce, S. Deschanel, S. Prange, and T. Mullin, *Mechanics of deformation-triggered pattern transformations and superelastic behavior in periodic elastomeric structures*, Journal of the Mechanics and Physics of Solids **56**, 2642 (2008).
- [4] K. Bertoldi, P. M. Reis, S. Willshaw, and T. Mullin, *Negative Poisson's Ratio Behavior Induced by an Elastic Instability*, Advanced Materials **22**, 361 (2009).
- [5] R. Lakes, *Foam Structures with a Negative Poisson's Ratio*, Science **235**, 1038 (1987).
- [6] D. Schattschneider, *The Plane Symmetry Groups: Their Recognition and Notation*, The American Mathematical Monthly **85**, 439 (1978).
- [7] W. F. Trench, *Introduction to Real Analysis*, Free online available at <http://ramanujan.math.trinity.edu/wtrench/misc/index.shtml>, 7th edition, 2013.
- [8] R. M. Temam and A. M. Miranville, *Mathematical Modeling in Continuum Mechanics*, Cambridge University Press, 2nd edition, 2005.
- [9] S. Lang, *Analysis II.*, Number v. 2 in Addison-Wesley series in mathematics, Addison-Wesley Pub. Co., 1969.
- [10] A. Boresi and R. Schmidt, *Advanced mechanics of materials*, John Wiley & Sons, 2003.
- [11] R. W. Ogden, *Non-Linear Elastic Deformations*, Dover Publications, 1984.
- [12] K. B. Petersen and M. S. Pedersen, *The Matrix Cookbook*, 2012, Version 20121115.
- [13] M. Sadd, *Elasticity: Theory, Applications, and Numerics*, Elsevier Science, 2010.
- [14] I. Jasluk, J. Chen, and M. Thorpe, *Elastic moduli of two dimensional materials with polygonal and elliptical holes*, Applied Mechanics Reviews **47**, S18 (1994).
- [15] R. L. Burden and J. D. Faires, *Numerical Analysis*, Thompson, 9th edition, 2005.
- [16] O. C. Zienkiewicz and R. L. Taylor, *The Finite Element Method: Its Basis and Fundamentals*, Butterworth-Heinemann, 6 edition, 2005.
- [17] G. H. Golub and C. F. V. Loan, *Matrix Computations*, The Johns Hopkins University Press, 4th edition, 2012.
- [18] R. Bastiaansen, *Bending and Buckling in Elastic Patterned Sheets*, 2013.

- [19] W. Schouten, *Elastic Instabilities in Monoholar and Bihholar patterned Networks*, 2014.
- [20] K. Hibbit and Sorensen, *ABAQUS Theory Manual (version 6.13)*, Hibbit, Karlsson and Sorenson Inc., Pawtucket (USA), 2013.
- [21] A. Day, K. Snyder, E. Garboczi, and M. Thorpe, *The elastic moduli of a sheet containing circular holes*, Journal of the Mechanics and Physics of Solids **40**, 1031 (1992).
- [22] C. Coulais, J. Overvelde, K. Bertoldi, and M. van Hecke, *Snap Through Buckling of Meta Beams*, In preparation, 2014.
- [23] S. Timoshenko and J. Gere, *Theory of Elastic Stability*, Dover Civil and Mechanical Engineering, Dover Publications, 1989.
- [24] H. Meijer, F. Dercole, and B. Oldeman, *Numerical Bifurcation Analysis*, in *Encyclopedia of Complexity and Systems Science*, edited by R. A. Meyers, pages 6329–6352, Springer New York, 2009.
- [25] Z. Bazant and L. Cedolin, *Stability of Structures: Elastic, Inelastic, Fracture, and Damage Theories*, Dover books on engineering, Dover Publications, 1991.
- [26] B. Hassani and E. Hinton, *A review of homogenization and topology optimization I—homogenization theory for media with periodic structure*, Computers & Structures **69**, 707 (1998).